Full-Vector Finite Difference Mode Solver for Whispering-Gallery Resonators

by

Serge M. Vincent
B.Eng., University of Victoria, 2013

A Thesis Submitted in Partial Fulfillment of the
Requirements for the Degree of

MASTER OF APPLIED SCIENCE

in the Department of Electrical and Computer Engineering

Full-Vector Finite Difference Mode Solver for Whispering-Gallery Resonators

by

Serge M. Vincent
B.Eng., University of Victoria, 2013

Supervisory Committee

Dr. Tao Lu, Supervisor
(Department of Electrical and Computer Engineering)

Dr. Reuven Gordon, Departmental Member
(Department of Electrical and Computer Engineering)

Supervisory Committee

Dr. Tao Lu, Supervisor
(Department of Electrical and Computer Engineering)

Dr. Reuven Gordon, Departmental Member
(Department of Electrical and Computer Engineering)

ABSTRACT

Optical whispering-gallery mode (WGM) cavities, which exhibit extraordinary spatial and temporal confinement of light, are one of the leading transducers for examining molecular recognition at low particle counts. With the advent of hybrid photonic-plasmonic and increasingly sophisticated forms of these resonators, the importance of supporting numerical methods has correspondingly become evident. In response, we adopt a full-vector finite difference approximation in order to solve for WGM's in terms of their field distributions, resonant wavelengths, and quality factors in the context of naturally discontinuous permittivity structure. A segmented Taylor series and alignment/rotation operator are utilized at such singularities in conjunction with arbitrarily spaced grid points.

Simulations for microtoroids, with and without dielectric nanobeads, and plasmonic microdisks are demonstrated for short computation times and shown to be in agreement with data in the literature. Constricted surface plasmon polariton (SPP) WGM's are also featured within this document. The module of this thesis is devised as a keystone for composite WGM models that may guide experiments in the field.

Contents

List of Tables

List of Figures

ACKNOWLEDGEMENTS

I would like to express my gratitude to:

Prof. Tao Lu, for the encouragement, tenacity, creativity, and insight that he exuded, as my supervisor, over the course of my thesis project.

Prof. Reuven Gordon and Prof. Rustom Bhiladvala, for their early guidance and contagious passion that inspired me to apply myself in the realm of academic research.

Xuan Du, Wenyan Yu, Amin Cheraghi Shirazi, and Niloofar Sadeghi, for their valuable discussions and assistance in the past two years.

My Family and Friends, for their patience, steadfast support, and faith in my ability to shed light on the cryptic facets of our universe.

La vie n'est facile pour aucun de nous. Mais quoi, il faut avoir de la persévérance, et surtout de la confiance en soi. Il faut croire que l'on est doué pour quelque chose, et que, cette chose, il faut l'atteindre coûte que coûte.

↕

Life is not easy for any of us. But what of that? We must have perseverance and above all confidence in ourselves. We must believe that we are gifted for something, and that this thing, at whatever cost, must be attained.

Marie Curie

DEDICATION

To my parents,
Daniel and Marie-Antoinette

Chapter 1

Introduction

Optical microcavities are a prominent platform for observing extraordinarily confined light interact with matter [1]. The confinement in space and time, represented by a low mode volume V and high quality factor Q, may localize a resonant field to a surface and form a "whispering-gallery" mode (WGM) that propagates circumferentially about the cavity periphery. These properties, including extended photon storage times, lay the foundation for a sensitive transducer that is competitive with surface plasmon resonance (SPR) [2] and nanomechanical resonator [3] based techniques, among others. Label-free biosensing towards single molecule detection in a dissipative environment is a principal application of this type of technology, aside from studies of cavity opto-mechanics [4, 5, 6], cavity quantum electrodynamics (QED) [7], nonlinear optics [8], and low-power narrow-linewidth lasing [9].

Recent attempts to lower the detection limit of WGM sensors have incorporated a combination of design philosophies, such as plasmon-enhanced near-field cavities [10, 11, 12]. Although a WGM in a plain silica microtoroid could alone resolve single 12.5-nm radius polystyrene nanobeads [13], researchers have further affixed tuned gold nanorods to comparable dielectric structures to discern the binding of single DNA-intercalating molecules whose masses are smaller than 1 kDa [14]. Since a WGM can be viewed as totally internally reflected light with an exponentially decaying evanescent field near the external cavity interface, one can explain this enhancement through a WGM-SPR mode coupling that increases the optical resonance shift. Such a change, however, comes at the expense of quality factor degradation from added energy conversion events or, in particular, plasmonic loss mechanisms.

Regardless of the experimental context, the underlying theory dictating an optical cavity's operation and relevance must be validated in an analytical sense. If

the complexity of the physical problem doesn't grant this luxury, the challenge of quantifying solutions or behaviour may instead be met with close approximations that fall under the domain of numerical modelling. An important step in any model should be some level of discretization applied to a region of interest, within which a light-matter system's evolution can be predicted. For instance, WGM resonance can be computed using the finite-difference time-domain (FDTD) [15, 16], eigenmode expansion [17, 18], boundary element (BE) [19, 20, 21], or finite-difference beam propagation (FD-BP) methods [22]. There are distinct trade-offs between their accuracy, requisite resources, and processing efficiency, yet the majority of the economical techniques implement a two-dimensional mode solver as to later aggregate the solver's output. M. Oxborrow previously characterized non-trivial electromagnetic resonators in terms of their cross-sectional field patterns, quality factors, and resonant frequencies using a finite element (FE) approach [23], the imposition being that the geometry be axisymmetric.

A mode solver may impose different degrees of constraint on the solutions of the mode equation it seeks to find. The basic finite difference formalism for a differential equation (i.e. an electromagnetic wave equation) expresses a function's derivatives by way of Taylor's theorem, assuming that the function is differentiable and continuous by some well-defined set of preconditions. This will often produce the largest possible truncation error, abated by interpolation or simply accounting for a greater number of grid points in each calculation [24]. Alternatively, prior knowledge of the generalized analytical functional form can allow for exceptional convergence rates, as was alluded to by G. Hadley in three separate cases: 1) uniform regions, 2) dielectric interfaces [25], and 3) dielectric corners [26].

This thesis seeks a finite difference paradigm that fully accounts for permittivity discontinuities in whispering-gallery microcavities, achieving it through an adaptation of the procedure from [27] that exploits a generalized Taylor series and a local coordinate transform at interfaces. If the grid spacing along the radial direction $\Delta\rho$ and height direction Δz in cylindrical coordinates are equated, a 7-point stencil can attain a second-order truncation error. Higher rates of convergence are attainable by, facilely, retaining extra terms in the series expansion and expressing the central field and its derivatives in terms of a greater number of neighbouring fields. The end product is a flexible full-vectorial framework that can disclose circulating eigenmodes, resonance quantities, and other attributes of traditional and exotic WGM apparatuses alike.

1.1 Thesis Outline

Chapter 2 is an independent summary of the physics behind whispering-gallery mode microcavities. It is intended to familiarize the reader with various types of cavities and their figures of merit, while establishing the experimental intuition that motivates later chapters.

Chapter 3 details the mathematical approach by which the mode solver is formulated. Governing equations, constitutive relations, special functions, and the identification of eigenwavelength-eigenmode pairs are presented. The finite difference solver derivation begins with its scalar form and ends with full-vectorial corrections.

Chapter 4 highlights three essential test cases for the mode solver methodology: whispering-gallery mode resonances in a bare microtoroidal cavity, in a plasmonic microdisk, and a microtoroidal cavity subjected to dielectric particle adsorption. Convergence is also quantitatively verified.

Chapter 5 contains the conclusion of the thesis and descriptions of future research prospects.

Chapter 2

Overview of Optical Microcavities

Acoustic whispering-gallery modes were first tentatively described by Lord Rayleigh in the late 19$^{\text{th}}$ century. His attempt was to explicate a phenomenon in the dome of St Paul's Cathedral, London, by which whispers became audible to distant listeners on the opposite side of the dome. He later, in a 1910 paper [28], arrived at a physical theory revealing that these were in fact resonances due to constructively interfering sound waves guided by the cavity formed by the wall curvature. This scientific interpretation created a surge in research productivity in the subject ever since, as scientists began to speculate over the existence of an optical counterpart to this mode. Theoretical investigations of optical WGM microresonator physics were published as long ago as 1939 [29], whereas the experimental demonstrations were pioneered in the late 1970's to early 1980's by researchers worldwide [30, 31, 32]. WGM microcavities have many practical purposes, playing an crucial role in transduction for biosensing, low-pump-power narrow-linewidth lasing, optomechanical excitations, and nonlinear optics.

The simplified operational principles of a WGM device are given by a geometrical optics perspective. If one considers a general whispering-gallery mode cavity, as seen in Figure 2.2, the cavity/core of refractive index n_1 and surrounding dielectric/cladding of refractive index n_2 satisfying $n_1 > n_2$ will evoke total internal reflection. Light rays coupled into the cavity at a plane of origin will internally propagate until they again reach the divisive interface, at which point they reflect. If such a ray impinges at the edge at an angle of incidence greater than the critical angle

Figure 2.1: Photograph from [33] of the Echo Wall in the Temple of Heaven, Beijing; another edifice that supports whispering-gallery modes.

$$\phi_c = \sin^{-1}\left(\frac{n_2}{n_1}\right) \tag{2.1}$$

from Snell's law, an exponentially decaying or evanescent field will be generated. Strong resonant build-up of energy will occur due to these lingering and contained light orbits. A temporal measure of confinement of such WGM's is the quality factor or Q factor, broadly quoted as 2π multiplied by the energy that is stored divided by the energy that is lost per cycle. Spectrally, the Q factor is the ratio of the resonant angular frequency ω_{Res} to the resonator linewidth $\Delta\omega$ such that

$$\begin{aligned} Q &= \omega_{\text{Res}} \frac{\text{Energy stored in the cavity}}{\text{Power lost per cycle}} \\ &= \frac{\omega_{\text{Res}}}{\Delta\omega} \end{aligned} \tag{2.2}$$

Only specific light waves will return to the coupling region in phase, i.e. those that follow

$$m\lambda_{\text{Res}} = 2\pi n_1 R \tag{2.3}$$

where the azimuthal mode order m is an integer and $2\pi n_1 R$ is the optical path length with radius R that, on average, the modal photons will traverse. All the while the spatial extent of the WGM will be minuscule, in the sense that photons lie in an effective potential at the interface similar to that trapping electrons in the Bohr atom.

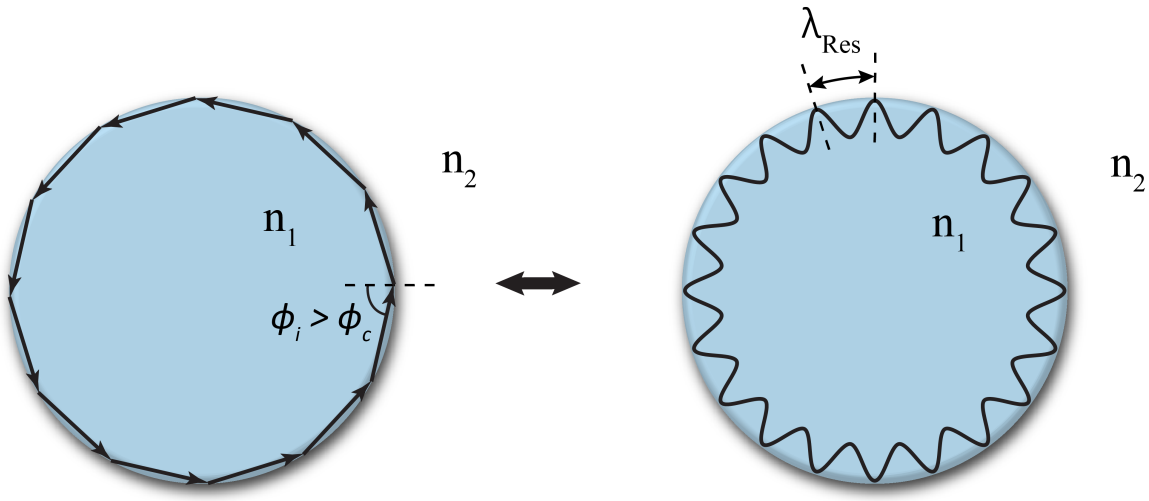

Figure 2.2: Geometrical optics depiction of whispering-gallery mode formation due to total internal reflection and the resultant resonance condition (i.e. m wavelengths along a circular optical path below the cavity surface) due to the in-phase superposition of electromagnetic waves.

2.1 Composition of the Quality Factor

In reality the Q-factor must be decomposed into components attributed to various losses. Its maximum is ultimately restricted by material absorption, being derived from the Beer-Lambert law and a Taylor series approximation to be

$$Q_o^{\text{abs}} = \frac{2\pi n_{\text{eff}}}{\lambda_{\text{Res}}\alpha} \tag{2.4}$$

for a linear absorption coefficient α and effective index n_{eff} [34]. We can amass other mechanisms, such as radiative loss (Q_o^{rad}), Rayleigh scattering from surface roughness (Q_o^{scat}), and surface contamination/imperfections (Q_o^{surf} from, e.g., water wetting the cavity face) to define an intrinsic quality factor Q_o such that

$$\frac{1}{Q_o} = \frac{1}{Q_o^{\text{abs}}} + \frac{1}{Q_o^{\text{rad}}} + \frac{1}{Q_o^{\text{scat}}} + \frac{1}{Q_o^{\text{surf}}} \tag{2.5}$$

that is recognized as the energy losses arising solely from the microcavity. Light is, on the other hand, delivered to and collected from the cavity through coupling peripherals such as a tapered waveguide [35] or a prism [36]. A portion of energy is removed from the resonator in this fashion, hence there is a coupling or extrinsinc quality factor Q_c. As a consequence the overall quality factor Q follows

$$\frac{1}{Q} = \frac{1}{Q_o} + \frac{1}{Q_c} \tag{2.6}$$

At resonance, the intracavity power can be maximized once critical coupling (i.e. $Q_c = Q_o$) takes place.

2.2 Reactive and Split Frequency Sensing

A compelling feature of the whispering-gallery mode is the evanescent field, protruding from the interface, that is sensitive to an inhomogeneity brought into proximity to it. The well-known reactive sensing modality [37, 38] relies on a cavity's predisposition to these light perturbations, in such a way that an excess polarizability α_{Ex} introduced by, say, particle adsorption will increase the optical path length. This will translate to a shift of $\Delta\lambda_{\text{Res}}$ in the resonant wavelength, gauged by first-order perturbation theory [39] as a perturbation of a field $\vec{E}_o$ such that

$$\frac{\Delta\lambda_{\text{Res}}}{\lambda_{\text{Res}}} \approx \frac{\alpha_{\text{Ex}}|\vec{E}_o(\vec{r}_i)|^2}{2\int \epsilon(\vec{r})|\vec{E}_o(\vec{r})|^2 \mathrm{d}V} \tag{2.7}$$

Here, the location of a bound material is $\vec{r}_i$ and the resonator's permittivity is ϵ. Operation of such WGM sensors is shown in Figure 2.3. Experimental configurations typically aim for a near-critical coupling of light from a tapered fiber to the microcavity within its equatorial plane, with a narrow-linewidth laser source swept in a wavelength range about a targeted resonance in the structure. Light transmission and the resolved frequency shifts of the spectrum's Lorentzian dip at resonance (whose center and full width at half-depth determine the loaded $Q = Q_oQ_c/(Q_o+Q_c)$, outside of cavity ring-down measurements) can be monitored by a photodetector-oscilloscope pair.

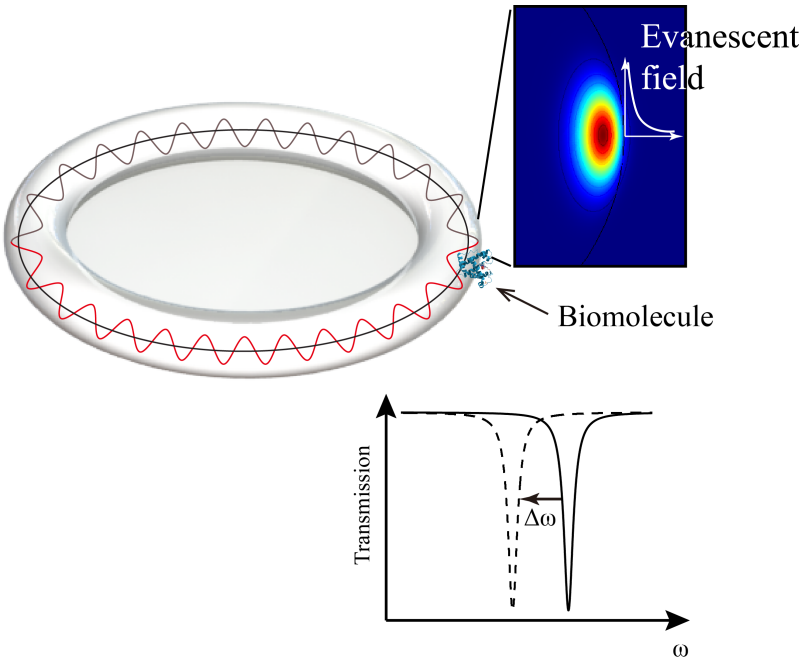

(a)

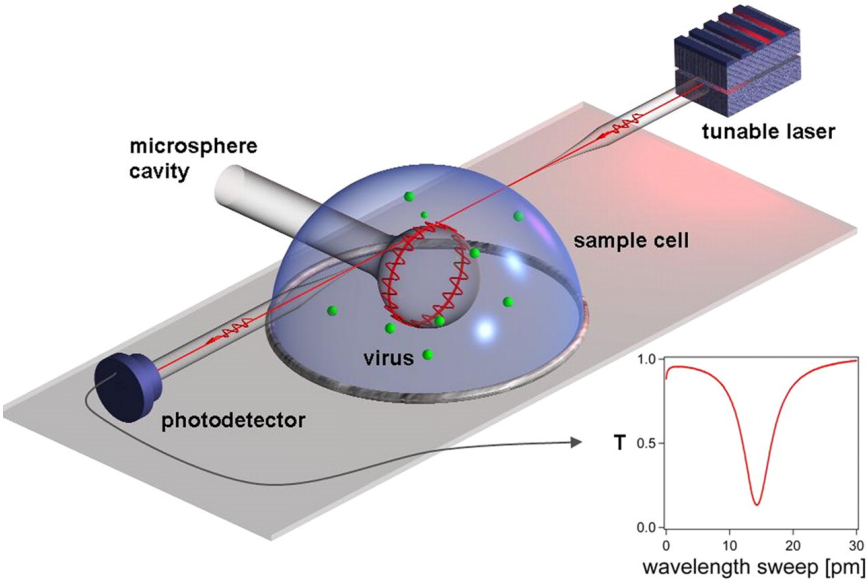

(b)

Figure 2.3: (a) Energy exchange within the evanescent field of a glass microtoroid. The light-matter interaction is one by which the adsorbed biosample is polarized and photons will roughly follow a modified trajectory (i.e. outlined in black). (b) Excerpt from [40]: Setup for label-free detection of single influenza A virions, using an optical fiber taper that crosses a cell with a silica WGM microsphere and encapsulating phosphate buffered saline droplet.

Ideally, there are two resonances in a WGM cavity due to azimuthal mode orders of opposite sign. This two-fold degeneracy is in the form of counterpropragating modes (the clockwise E_+ and counter-clockwise E_-) of identical resonant wavelengths and transverse field distributions that, veritably, is lifted by the presence of scatterers. If Rayleigh backscattered light from the forward propagating field overcomes the round-trip loss, a backwards propagating field of equal power can appear. Minute nanoparticles bound to the cavity surface will act as scattering centers and result in a pair of cavity standing wave patterns, splitting the mode into two angular frequencies whose spectral separation is [41]

$$\beta_{\pm} = \frac{\omega_{\mathrm{Res}}}{2} \frac{\int \vec{E}_+(\vec{r}) \Delta\epsilon(\vec{r}) \vec{E}^*_-(\vec{r}) \mathrm{d}V}{\int \epsilon(\vec{r}) |\vec{E}_+(\vec{r})|^2 \mathrm{d}V} \tag{2.8}$$

where ω_{Res} is the central resonant angular frequency. Measurements of the change in frequency splitting can be employed to discriminate common mode noise, such as mutual shifting caused by temperature fluctuations, towards eventual suppression. The probe laser jitter or frequency instability, originating in part from deviations of the length of the internal lasing cavity and the Schawlow-Townes linewidth limitation [42], can be cancelled by way of mode splitting [43, 44].

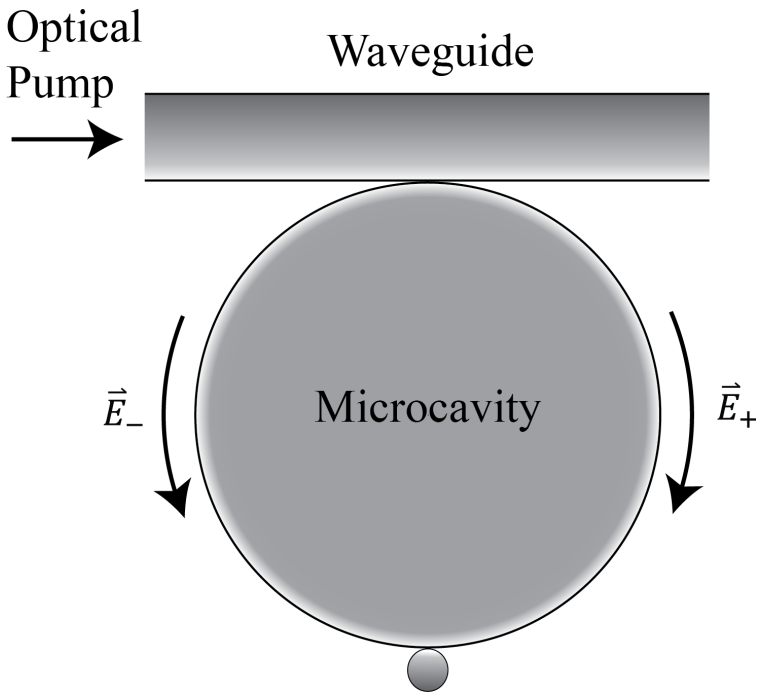

Figure 2.4: WGM doublet generation by light scattering off a surface contaminant.

2.3 Thermo-Optic and Quadratic Electro-Optic Influences

The relative ease of triggering nonlinearities in WGM resonators was first acknowledged by R. K. Chang and A. J. Campillo in the last two decades of the 20^{th} century [45, 46, 47, 48, 49]. Their research involving the free-space excitation based optical pumping of high-Q liquid microdroplets led them to observe unusual effects, including Brillouin and cascaded Raman scattering, at considerable pump thresholds due to low efficiency.

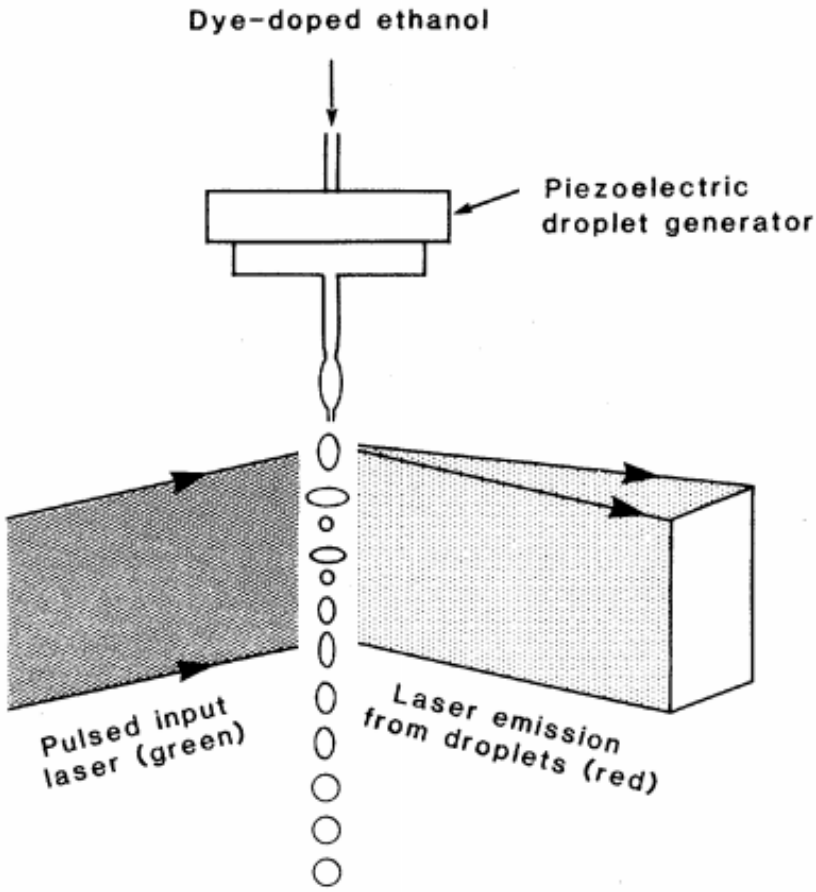

Figure 2.5: Experimental configuration for monitoring emitted electromagnetic radiation (i.e. isotropic orange fluorescence and partially polarized red laser light output for green laser light input) from droplets within a stream. Originally published in [45].

The stability of solid-state platforms (e.g. those primarily consisting of a silicon dioxide dielectric) has, in comparison, proven favourable over the transient nature of the prior droplets. The considerable resonant accumulation of energy within a WGM microcavity lowers optical nonlinearity thresholds and can be attributed to two paramount parameters:

1. Long photon storage times
2. Confinement to small mode volumes

Heating from absorption results in temperature fluctuations ΔT, therefore perturbing refractive indices via

$$\Delta n = \frac{\mathrm{d}n}{\mathrm{d}T}\Delta T \tag{2.9}$$

for a material-dependent thermo-optic coefficient $\frac{\mathrm{d}n}{\mathrm{d}T}$. Besides thermorefractivity, an emerging temperature distribution will also induce thermal expansion as to increase the optical path length L and, in turn, raise $\Delta\lambda_{\mathrm{Res}}$. These combined effects can be described using

$$\frac{\Delta\lambda_{\mathrm{Res}}}{\lambda_{\mathrm{Res}}} = \Delta T\left(\frac{1}{n}\frac{\mathrm{d}n}{\mathrm{d}T} + \frac{1}{L}\frac{\mathrm{d}L}{\mathrm{d}T}\right) \tag{2.10}$$

in which $\frac{1}{n}\frac{\mathrm{d}n}{\mathrm{d}T} + \frac{1}{L}\frac{\mathrm{d}L}{\mathrm{d}T} = 8.83 \times 10^{-6}\ \mathrm{K}^{-1}$ for fused silica near $\lambda = 1540$ nm [50]. It is generally acceptable, however, to neglect the latter term due to the fact that the former is dominant. For high modal intensities I, we may apply the Kerr effect adjustment associated with the second-order nonlinear refractive index $n_{2,\mathrm{K}}$:

$$\Delta n = n_{2,\mathrm{K}} I \tag{2.11}$$

Dielectric material deformation due to the presence of an electric field, i.e. electrostriction, additionally contributes to $n_{2,\mathrm{K}}$.

2.4 Microcavity Materials

Ultrahigh-Q, optically resonant cavities can be fashioned out of numerous compounds as to influence their limit of detection, instigate Raman lasing, or tweak propagative dynamics. The ultralow loss of fused or thermally grown silica (SiO_2) [34] has enabled

it to secure a foothold in WGM device fabrication. The need for on-chip integration in silicon photonics has, conversely, diverted some research towards silicon [51] with the mandatory trade-off entailed by large permittivity contrasts. Silicon nitride (Si_3N_4) [52], whose nonlinear properties are relevant to nonlinear optics, is also suited for constructing WGM nanostructures. Electro-optical crystals, e.g. lithium niobate ($LiNbO_3$) [53], have been chosen for the utility of their electrical tunability. Gallium arsenide (GaAs) [54], in addition to other III-V semiconductors, have successfully made up active lasing microcavities. Nonetheless, in the earlier stages of the field the record quality factors near 6.3×10^{10} were achieved with calcium fluoride (CaF_2) crystals [55].

2.5 Microcavity Architectures

2.5.1 Silica Microspheres

A spherically symmetric SiO_2 cavity lends itself to analytical solutions for its eigenmodes. In vacuo and in spherical coordinates (ρ, θ, ϕ), a scalar approximation $\psi(\vec{r}) = \vec{r} \cdot \vec{E}(\vec{r})$ or $\vec{r} \cdot \vec{H}(\vec{r})$ of the electric field $\vec{E}$ or magnetic displacement vector $\vec{H}$ leaves [56]

$$\psi_{N,\ell,m}(\rho,\theta,\phi) = \begin{cases} A j_\ell(k_c\rho) P_\ell^m(\cos\theta) \mathrm{e}^{\pm im\phi}, & \rho \le a \\ B h_\ell(k_o\rho) P_\ell^m(\cos\theta) \mathrm{e}^{\pm im\phi}, & \rho > a \end{cases} \tag{2.12}$$

and characteristic equations

$$\frac{\frac{\partial}{\partial(k_c a)}\left[(k_c a) j_\ell(k_c a)\right]}{(k_c a) j_\ell(k_c a)} - \sqrt{\epsilon_c} \frac{\frac{\partial}{\partial(k_o a)}\left[(k_o a) h_\ell(k_o a)\right]}{(k_o a) h_\ell(k_o a)} = 0 \qquad \text{for } \vec{r} \cdot \vec{E}(\vec{r}) = 0 \tag{2.13}$$

$$\frac{\frac{\partial}{\partial(k_c a)}\left[(k_c a) j_\ell(k_c a)\right]}{(k_c a) j_\ell(k_c a)} - \frac{1}{\sqrt{\epsilon_c}} \frac{\frac{\partial}{\partial(k_o a)}\left[(k_o a) h_\ell(k_o a)\right]}{(k_o a) h_\ell(k_o a)} = 0 \qquad \text{for } \vec{r} \cdot \vec{H}(\vec{r}) = 0 \tag{2.14}$$

where a is the sphere radius, P_ℓ^m is an associated Legendre polynomial, j_ℓ is a spherical Bessel function, h_ℓ is a spherical Hankel function, the cavity wavenumber is k_c, the cavity's relative permittivity is ϵ_c, the vacuum wavenumber is k_o, and N as well as ℓ are the radial and polar mode numbers, respectively. A and B materialize from mode selection (either those from (2.13) or (2.14)) and the continuity at the sphere interface.

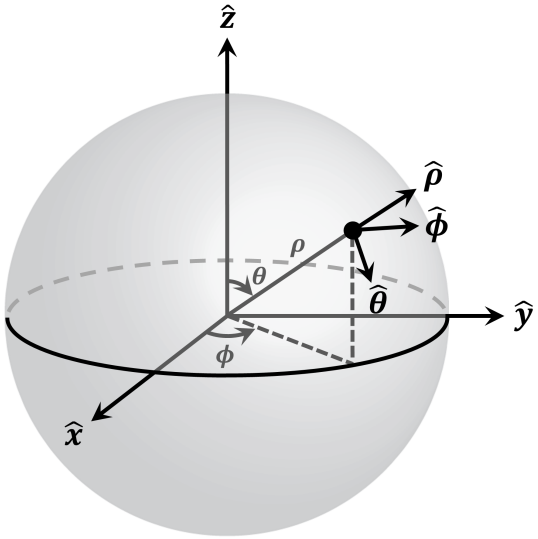

Figure 2.6: Spherical coordinate system.

Fabrication of a microsphere ordinarily consists of stripping a commercial optical fiber, etching it with buffered hydrofluoric acid (HF) solution to control its size, and melting the tip through strong absorption of pulsed laser light (e.g. CO_2 system with a $\sim$10.6 μm emission wavelength) or hydrogen-oxygen flame exposure. This final step, referred to as "reflow", leads to surface tension aided smoothing of the resonator surface. Quality factors up to $0.8 \pm 0.1 \times 10^{10}$ have been reported for a wavelength close to 633 nm [34], having fallen to 10^8 in the near infrared regime upon moisture contamination.

2.5.2 Silicon Microrings

With a dielectric constant ranging from 11.0 to 12.0, silicon ring resonators support single-mode propagation with very low signal power loss and ready manufacturability. They are cost-effective to arrange as a large-scale array using deep ultraviolet (UV) lithography, and as a class of device silicon ring resonators can perform as label-free biosensors (with minimal crosstalk and an adequate dynamic range, for quantitative assays, while in an array [57]), high-speed modulators [58], and optical filters [59].

2.5.3 Microdisks

Elaborate lithographic and etching processes are required to functionalize WGM microdisks, yet this comes with the benefit of rendering them compatible with integrated circuits. Silica microdisks are actualized by:

1. Thermally growing an oxide thin film on a silicon wafer, alternatively fabricated by chemical vapor deposition (CVD), plasma-enhanced CVD (PECVD), flame hydrolysis deposition (FHD), or the sol-gel method.
2. Spin coating a layer of photoresist onto the wafer.
3. Soft baking the sample.
4. Patterning it in order to transfer the microdisk image from a chromium mask to the wafer with UV light exposure.
5. Hard baking the sample to smooth the edges of the disks.
6. Removing the unexposed photoresist for film development, followed by immersion in buffered HF to wet etch the unprotected silicon dioxide and leave behind microdisks.
7. Applying xenon difluoride (XeF_2) isotropic etching to form the silicon pillars beneath the disks.

The smooth wedge along the cavity curvature allows for quality factors in the vicinity of 10^7 [60] and, with electron-beam lithography or finer resolutions afforded by a stepper, rises to 8.75×10^8 [61]. Silicon microdisks with Q's on the order of 10^6 have also been demonstrated [62].

2.5.4 Silica Microtoroids

As an extension of the procedure in Subsection 2.5.3, reflowing a silica microdisk with a CO_2 laser can further improve the optical Q to 5×10^8 [63]. The toroidal end-product (c.f. Figure 2.7a), shown as being one of the only on-chip microcavities with such extreme light confinement, has been purposed for frequency microcomb generation [64], cavity optomechanics analyses [65], as well as a plethora of applications discussed in the Introduction [4, 5, 6, 7, 8, 9, 13].

2.5.5 Double-Disk Microresonators

By positioning two virtually parallel silica disks at a gap distance of a few nanometres, strong dynamical backaction effects (exceeding those in several competing optomechanical constructs) will occur. By selective plasma etching of the silicon substrate and sacrificial amorphous silicon (a-Si) layer sandwiched in a multilayer stack, i.e. SiO_2-a-Si-SiO_2, one can fabricate a double-disk with sensitive WGM feedback exhibiting a notable per-photon gradient force of 22 fN for a 138 nm air gap [66].

2.5.6 Silica Microbubbles

Stable transport and localization of proteins, deoxyribonucleic acid (DNA), virions, and other species to a WGM cavity is crucial for spectral identification and/or close observations of mode-particle interactions. Apart from optical trapping, it is possible to accomplish this by converting a vessel segment directly into a microcavity. The silica microbubble is just this - a WGM resonator shaped by arc discharge heating of pressurized silica capillaries [67, 68]. The design enables transport of liquid and measured entities within the internal confines of the silica tubule and microbubble, with a streamlined coupling geometry and small insertion loss. The potential for the cavity to be configured as a gas sensor, due to its fluid containment, is present as well.

2.5.7 Bottleneck Microresonators

A chief objective in quantum optics is to realize strongly entangled photon states. Two photons will rarely interact (after all, they are bosons and are capable of occupying the same quantum state), failing completely to influence one another in a perfect vacuum. Nevertheless, there are nonlinear responses in exotic platforms, such as a bottleneck WGM cavity interfaced with a nanofiber and coupled to a single rubidium atom, that push for a π phase shift and thus a tangible level of entanglement [70].

The curvature profile of the bottleneck is fabricated by a heat-and-pull process divided into two parts:

1. Elongating a fiber along with heating from a scanned CO_2 laser or travelling flame.

2. Adding a parabolic bulge by delicately stretching the fiber waist while CO_2 laser microtapering two near-contiguous sections.

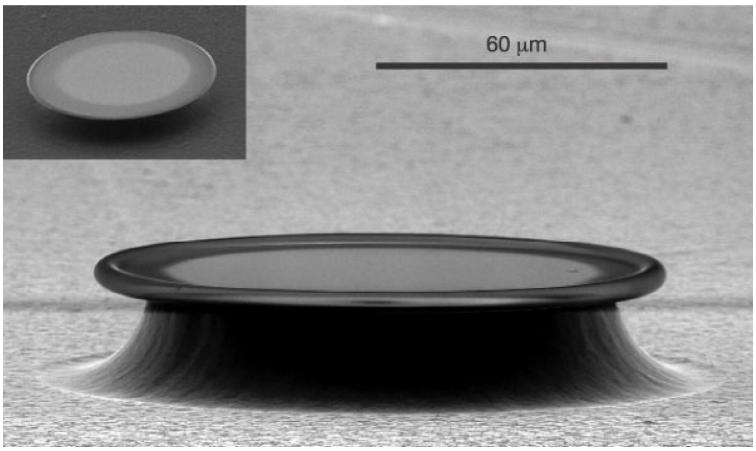

(a)

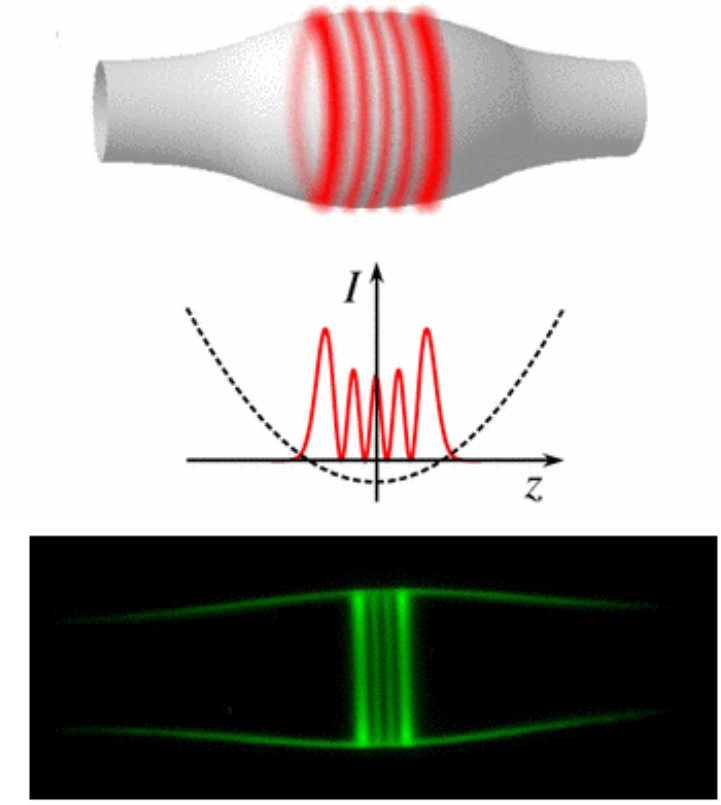

(b)

Figure 2.7: (a) Reference [63]: A scanning electron micrograph of a typical silica microtoroid. (b) Reference [69]: Conceptual diagram of the radial and axial confinement of the optical mode of a bottleneck resonator, as well as the detected green fluorescence from an erbium-doped variant with 36-μm diameter.

The constricting bottleneck is useful in tuning optical modes, for its axially-confining effective harmonic potential (depicted in Figure 2.7b) is modified by the curvature profile alone [69]. Note that the optomechanical characteristics of a similar bottle geometry have been put forward for mass sensing [71].

2.5.8 Liquid-Core Optical Ring-Resonators

With functional principles that are very much the same as that of a silica microbubble, the liquid-core optical ring-resonator (LCORR) hosts internal fluid flow. LCORR's with modest Q-factors, marginally above those of standard ring resonators despite the unconstrained longitudinal extent of the whispering-gallery mode, consist of fused silica capillaries with a wall of a few microns whose inner surface is coated with a polymer. The outer radius is determined by H_2O flame heated stretching of a central capillary region, while etching stipulates the wall thickness. Mie theory conveniently reproduces the experimentally observed radial distribution of a LCORR WGM [72].

2.6 Surface Plasmon Polaritons and Localized Surface Plasmons

Free electrons in the conduction band of metals heavily influence their response to electromagnetic activity. At visible frequencies, the free electron gas can undergo sustained as well as volume charge density oscillations that are seldom observed in other parts of the spectrum. These "surface plasmons" [73] at the interface between a dielectric and a metal (whose dielectric constant has a larger magnitude and negative real part) will couple to light by enhancing and spatially confining it. With the constriction of an electron gas in three spatial dimensions, e.g. in a subwavelength metallic particle, the displacement of electrons from the positively charged lattice gives rise to a restoring force and establishes geometry-dependent resonances.

Surface plasmon polaritons (SPP's) are surface waves [74, 75] - an outcome when surface plasmons couple to electromagetic waves [76]. Given a half-space with ohmic losses such that $\epsilon_1 = \epsilon_1' + i\epsilon_1''$ and $|\epsilon_1''| \ll |\epsilon_1'|$ bordering a polarizable nonconducting half-space with real ϵ_2, the wavevector's parallel component is

$$
\begin{aligned}
k_{\parallel} &= k'_{\parallel} + ik''_{\parallel} \\
&\approx \frac{\omega}{c}\sqrt{\frac{\epsilon'_1\epsilon_2}{\epsilon'_1+\epsilon_2}}\left[1 + i\frac{\epsilon''_1\epsilon_2}{2\epsilon'_1(\epsilon'_1+\epsilon_2)}\right]
\end{aligned} \tag{2.15}
$$

with $k = \omega/c = 2\pi/\lambda$ denoting the wavenumber in free space. From this, the SPP wavelength can be found:

$$
\begin{aligned}
\lambda_{\mathrm{SPP}} &= \frac{2\pi}{k'_{\parallel}} \\
&\approx \lambda\sqrt{\frac{\epsilon'_1+\epsilon_2}{\epsilon'_1\epsilon_2}}
\end{aligned} \tag{2.16}
$$

The $1/e$ decay length of the E-field is conveyed by $1/k''_{\parallel}$, attaining ~ 60 μm for silver and ~ 10 μm for gold at $\lambda = 633$ nm [77]. Away from the interface, to first order in $|\epsilon''_1|/|\epsilon'_1|$, the perpendicular

$$
k_{1,\perp} \approx \frac{\omega}{c}\sqrt{\frac{\epsilon'^2_1}{\epsilon'_1+\epsilon_2}}\left(1 + i\frac{\epsilon''_1}{2\epsilon'_1}\right) \tag{2.17}
$$

$$
k_{2,\perp} \approx \frac{\omega}{c}\sqrt{\frac{\epsilon^2_2}{\epsilon'_1+\epsilon_2}}\left[1 - i\frac{\epsilon''_1}{2(\epsilon'_1+\epsilon_2)}\right] \tag{2.18}
$$

with E-field $1/e$ decay lengths $1/k_{1,\perp}$, $1/k_{2,\perp}$ of roughly 23 nm, 421 nm for Ag and 28 nm, 328 nm for Au [77]. Once there are characteristic sizes of the metallic structure below the electron mean free path, we must further account for the increased probability of scattering from the interface that will augment ϵ''_1. By tilting the light line (vide Figure 2.8) via creating evanescent waves in medium 2 of refractive index > 1, SPP's may be excited.

In nanoscale metallic particles or configurations, such as nanospheres, there are bound charge oscillations or localized surface plasmons (LSP's). For such spheres at the quasi-static limit (i.e. presumption that all object points respond simultaneously to an incoming field) valid for dimensions $\ll \lambda$, the local field $\vec{E} = -\nabla\Phi$ with a potential Φ satisfying the Laplace equation $\nabla^2\Phi = 0$. Averting a long-winded explanation,

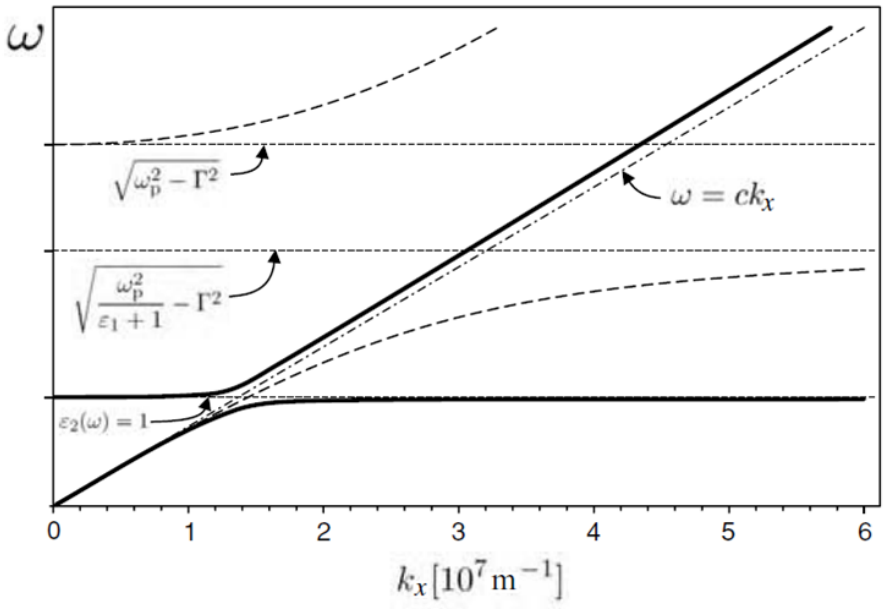

Figure 2.8: Extracted from [77]: SPP dispersion relation for a gold/air interface, where the dashed line relates to a Drude-Sommerfeld dielectric function while the solid line relates to that which incorporates a single interband transition. The volume plasma frequency is ω_p and frictional damping is proportional to Γ.

it can be shown that the scattered field is indistinguishable to an electrostatic field of a dipole centered at the sphere. A metallic nanosphere of radius r_p with complex $\epsilon_1(\omega)$ in a medium with ϵ_2 would then have a polarizability

$$\alpha(\omega) = 4\pi\epsilon_o r_p^3 \frac{\epsilon_1(\omega) - \epsilon_2}{\epsilon_1(\omega) + 2\epsilon_2} \tag{2.19}$$

for the permittivity of free space ϵ_o, resonating at the Fröhlich condition $\mathrm{Re}[\epsilon_1(\omega)] = -2\epsilon_2$ when $\mathrm{Im}[\epsilon_1(\omega)]$ is slowly-varying or diminutive. Furthermore, the scattering cross-section

$$\sigma_\mathrm{scatt} = \frac{k^4}{6\pi\epsilon_o^2}|\alpha(\omega)|^2 \tag{2.20}$$

and absorption cross-section

$$\sigma_\mathrm{abs} = \frac{k}{\epsilon_o}\mathrm{Im}[\alpha(\omega)] \tag{2.21}$$

Consolidating optical WGM microcavities with plasmonics [11, 78, 79] ameliorates sensitivity, as resonance shifts are directly heightened by the dually increased

numerator and decreased denominator in expression (2.7). In stark constrast to surface enhanced Raman spectroscopy (SERS), the goal of these hybrid systems is to enhance near-field signals by slight detuning of the WGM resonance with respect to the plasmon resonance in order to lessen scattering losses. As an aside, theoretical limits of detection amid noise (e.g. thermorefractive and Gaussian) have been touched upon by the scientific community [80, 81].

Chapter 3

Full-Vector Finite Difference Mode Solver's Theoretical Basis

3.1 Electrodynamic Wave Equation

Maxwell's equations concern two fundamental fields: the electric field $\vec{E}$ and magnetic field $\vec{B}$. Collectively, these equations in their differential form reveal how the fields behave over space and time. They are individually known as Gauss's law of electrostatics, Gauss's law of magnetostatics, Faraday's law, and Ampère's law

$$\nabla \cdot \vec{D}(\vec{r},t) = \rho(\vec{r},t) \tag{3.1}$$

$$\nabla \cdot \vec{B}(\vec{r},t) = 0 \tag{3.2}$$

$$\nabla \times \vec{E}(\vec{r},t) = -\frac{\partial \vec{B}(\vec{r},t)}{\partial t} \tag{3.3}$$

$$\nabla \times \vec{H}(\vec{r},t) = \vec{j}(\vec{r},t) + \frac{\partial \vec{D}(\vec{r},t)}{\partial t} \tag{3.4}$$

where the electric displacement vector $\vec{D} = \epsilon_o \epsilon_r \vec{E}$, the magnetic displacement vector $\vec{H} = \vec{B}/\mu_o$ for nonmagnetic materials, ρ is the free charge density, and $\vec{j}$ is the free current density with respect to position $\vec{r}$ and time t. The quantities $\epsilon_o = 8.85 \times 10^{-12}$ F/m, $\mu_o = 4\pi \times 10^{-7}$ H/m, and ϵ_r are respectively the vacuum permittivity, vacuum permeability, and material dependent relative permittivity. The constitutive relations above are more properly described as the response of matter under the influence of fields, in that there is a macroscopic polarization $\vec{P}$ and magnetization $\vec{M}$ that are

contained within

$$\vec{D}(\vec{r},t) = \epsilon_o \vec{E}(\vec{r},t) + \vec{P}(\vec{r},t) \tag{3.5}$$

$$\vec{H}(\vec{r},t) = \frac{1}{\mu_o}\vec{B}(\vec{r},t) - \vec{M}(\vec{r},t) \tag{3.6}$$

The magnetic susceptibility $\chi_m = 0$ suggests $\vec{M} = \chi_m \vec{H} = \vec{0}$ and the electric susceptibility χ_e in $\vec{P} = \epsilon_o \chi_e \vec{E}$ defines the relative permittivity as $\epsilon/\epsilon_o = \epsilon_r = \chi_e + 1$. Note that we assume here that ϵ_r has the simplest possible tensor rank of 0, corresponding to an isotropic, homogeneous, linear medium. In the absence of free charges ($\rho = 0$) and currents ($\vec{j} = \vec{0}$), manipulation of equations (3.1)-(3.6) and the use of the vector identity

$$\nabla \times (\nabla \times \vec{A}) = \nabla(\nabla \cdot \vec{A}) - \nabla^2 \vec{A} \tag{3.7}$$

will lead us to express the electromagnetic (EM) wave or vector Helmholtz equations as

$$\nabla^2 \vec{E} = \mu_o \epsilon_o \epsilon_r \frac{\partial^2 \vec{E}}{\partial t^2} \tag{3.8}$$

and

$$\nabla^2 \vec{B} = \mu_o \epsilon_o \epsilon_r \frac{\partial^2 \vec{B}}{\partial t^2} \tag{3.9}$$

where the phase speed $v_{\mathrm{p}} = \frac{1}{\sqrt{\mu_o \epsilon_o \epsilon_r}} = \frac{c}{\sqrt{\epsilon_r}} = \frac{c}{n}$, n is the refractive index, and $c = 3.00 \times 10^8$ m/s is the speed of light in free space. Attenuation can be reinserted into the wave equation by replacing

$$\epsilon \to \epsilon + i\frac{\sigma}{\omega \epsilon_o} \tag{3.10}$$

where $i = \sqrt{-1}$, the conductivity is σ, and the optical angular frequency is ω. A complex dielectric constant, which we can denote as $\widetilde{\epsilon}$, further implies a complex refractive $\widetilde{n}$ that together relate to an asborption index κ:

$$\widetilde{\epsilon} = \widetilde{n}^2 = (n + i\kappa)^2 \tag{3.11}$$

Separating the variables of the Helmholtz equation for $\vec{E}$, the spherical coordinates representation

$$\begin{aligned} \frac{1}{\rho^2}\frac{\partial}{\partial\rho}\left(\rho^2\frac{\partial\vec{E}}{\partial\rho}\right)+\frac{1}{\rho^2\sin\theta}\frac{\partial}{\partial\theta}\left(\sin\theta\frac{\partial\vec{E}}{\partial\theta}\right)+\frac{1}{\rho^2\sin^2\theta}\frac{\partial^2\vec{E}}{\partial\phi^2}+k_0^2\epsilon_r\vec{E}=0 \\ \frac{\partial}{\partial\rho}\left(\rho^2\frac{\partial\vec{E}}{\partial\rho}\right)+k_0^2\epsilon_r\rho^2\vec{E}=-\frac{1}{\sin\theta}\frac{\partial}{\partial\theta}\left(\sin\theta\frac{\partial\vec{E}}{\partial\theta}\right)-\frac{1}{\sin^2\theta}\frac{\partial^2\vec{E}}{\partial\phi^2}=\text{Constant} \end{aligned} \tag{3.12}$$

permits us to write $|\vec{E}(\rho,\theta,\phi)|=R(\rho)F(\theta,\phi)$. Afterwards, the rearranged

$$F\sin^2\theta\left[\frac{1}{R}\frac{\partial}{\partial\rho}\left(\rho^2\frac{\partial R}{\partial\rho}\right)+k_0^2\epsilon_r\rho^2\right]+\sin\theta\frac{\partial}{\partial\theta}\left(\sin\theta\frac{\partial F}{\partial\theta}\right)=-\frac{\partial^2F}{\partial\phi^2}=\text{Constant} \tag{3.13}$$

deduces $F(\theta,\phi)=\Theta(\theta)\Phi(\phi)$. It is reasonable to presume that the longitudinal variation along ϕ can be isolated via $\Phi(\phi)=e^{\pm im\phi}$ with azimuthal mode order m in the analysis of an optical WGM microcavity. A single direction of propagation reduces the field to $\vec{E}(\rho,\theta,\phi)=\vec{E}(\rho,\theta)e^{-im\phi}$, such that $\frac{\partial^2\vec{E}}{\partial\phi^2}=-m^2\vec{E}$. We would, however, formally account for loss by accepting an imaginary part m_i of a complex mode number $\widetilde{m}$:

$$\widetilde{m}=m+im_i \tag{3.14}$$

There are then two separable solutions for the formulae

$$\frac{1}{R}\left(\rho^2\frac{\partial^2R}{\partial\rho^2}+2\rho\frac{\partial R}{\partial\rho}\right)+k_0^2\epsilon_r\rho^2=\ell(\ell+1) \tag{3.15}$$

and

$$\begin{aligned} \frac{m^2}{\sin^2\theta}-\frac{1}{\Theta}\left(\frac{\partial^2\Theta}{\partial\theta^2}+\frac{\cos\theta}{\sin\theta}\frac{\partial\Theta}{\partial\theta}\right)&=\ell(\ell+1) \\ \downarrow\ \mathrm{x}&=\cos\theta \\ \frac{m^2}{1-\mathrm{x}^2}-\frac{1}{\Theta}\left[(1-\mathrm{x}^2)\frac{\partial^2\Theta}{\partial\mathrm{x}^2}-2\mathrm{x}\frac{\partial\Theta}{\partial\mathrm{x}}\right]&=\ell(\ell+1) \end{aligned} \tag{3.16}$$

Emerging analytical solutions for these formulae are $R(\rho)=A_\ell j_\ell(k_o\sqrt{\epsilon_r}\rho)+B_\ell y_\ell(k_o\sqrt{\epsilon_r}\rho)$ and $\Theta(\mathrm{x})=P_\ell^m(\mathrm{x})\rightarrow\Theta(\theta)=P_\ell^m(\cos\theta)$ where j_ℓ is a spherical Bessel function of the first kind, y_ℓ is a spherical Bessel function of the second kind (or spherical Neumann function), P_ℓ^m is an associated Legendre polynomial, A_ℓ as well as B_ℓ are

yet-undetermined coefficients, and the integer degree ℓ must be equal to or greater than the order m. Products of R and Θ may form a general solution

$$|\vec{E}(\rho,\theta)| = \sum_{\ell} \left[A_\ell j_\ell(k\rho) + B_\ell y_\ell(k\rho)\right] P_\ell^m(\cos\theta) \tag{3.17}$$

while keeping in mind that $k\rho = k_o\sqrt{\epsilon_r}\rho$.

3.1.1 Interface Continuity Relations

Integral forms of Maxwell's equations are the bridge towards the treatment of permittivity and permeability discontinuities when solving for electromagnetic fields. According to Gauss's and Stoke's theorems, although differentiability of $\vec{E}$, $\vec{D}$, $\vec{H}$, and $\vec{B}$ field components may be inhibited at singular points [82],

$$\oint \vec{E}(\vec{r},t)\cdot d\vec{l} = -\int_S \frac{\partial}{\partial t}\vec{B}(\vec{r},t)\cdot d\vec{S} \tag{3.18}$$

$$\oint \vec{D}(\vec{r},t)\cdot d\vec{S} = \int_V \rho(\vec{r},t)dV \tag{3.19}$$

$$\oint \vec{H}(\vec{r},t)\cdot d\vec{l} = \int_S \left[\vec{j}(\vec{r},t) + \frac{\partial}{\partial t}\vec{D}(\vec{r},t)\right]\cdot d\vec{S} \tag{3.20}$$

$$\oint \vec{B}(\vec{r},t)\cdot d\vec{S} = 0 \tag{3.21}$$

denoting the volume element dV, surface element $d\vec{S}$, and line element $d\vec{l}$. Lacking sources at the interface, an infinitesimal volume V and enclosed area S will unveil that the tangential component of the electric field E_t and magnetic displacement vector H_t in neighbouring regions I and II obey

$$E_{t,\mathrm{I}} - E_{t,\mathrm{II}} = 0 \tag{3.22}$$

$$H_{t,\mathrm{I}} - H_{t,\mathrm{II}} = 0 \tag{3.23}$$

and the normal component of the electric displacement vector D_n and magnetic field B_n obey

$$D_{n,\mathrm{I}} - D_{n,\mathrm{II}} = 0 \tag{3.24}$$

$$B_{n,\mathrm{I}} - B_{n,\mathrm{II}} = 0 \tag{3.25}$$

Equivalently, these continuity relations can be expressed as cross and dot products

$$\hat{n} \times (\vec{E}_{\mathrm{I}} - \vec{E}_{\mathrm{II}}) = \vec{0} \tag{3.26}$$

$$\hat{n} \times (\vec{H}_{\mathrm{I}} - \vec{H}_{\mathrm{II}}) = \vec{0} \tag{3.27}$$

$$\begin{gathered} \hat{n} \cdot (\vec{D}_{\mathrm{I}} - \vec{D}_{\mathrm{II}}) = 0 \\ \hat{n} \cdot (\epsilon_{\mathrm{I}} \vec{E}_{\mathrm{I}} - \epsilon_{\mathrm{II}} \vec{E}_{\mathrm{II}}) = 0 \end{gathered} \tag{3.28}$$

$$\begin{gathered} \hat{n} \cdot (\vec{B}_{\mathrm{I}} - \vec{B}_{\mathrm{II}}) = 0 \\ \hat{n} \cdot (\vec{H}_{\mathrm{I}} - \vec{H}_{\mathrm{II}}) = 0 \end{gathered} \tag{3.29}$$

where $\hat{n}$ is the unit normal vector to the interface and the optical media have $\mu_{\mathrm{I}} = \mu_{\mathrm{II}} = \mu_o$.

3.1.2 Special Functions

Bessel's differential equation yields standard solutions J and Y, correlated to j and y to the extent that they become normalized Bessel functions of half-integral order:

$$j_\ell(k_o\sqrt{\epsilon_r}\rho) = \sqrt{\frac{\pi}{2k_o\sqrt{\epsilon_r}\rho}} J_{\ell+\frac{1}{2}}(k_o\sqrt{\epsilon_r}\rho) \tag{3.30}$$

$$y_\ell(k_o\sqrt{\epsilon_r}\rho) = \sqrt{\frac{\pi}{2k_o\sqrt{\epsilon_r}\rho}} Y_{\ell+\frac{1}{2}}(k_o\sqrt{\epsilon_r}\rho) \tag{3.31}$$

We are also able to write the functions $j_\ell(k_o\sqrt{\epsilon_r}\rho) = j_\ell(z)$ and $y_\ell(k_o\sqrt{\epsilon_r}\rho) = y_\ell(z)$ (displayed in Figures 3.1a and 3.1b for sample arguments) as Rayleigh formulae, such that

$$j_\ell(z) = (-z)^\ell \left(\frac{1}{z}\frac{\mathrm{d}}{\mathrm{d}z}\right)^\ell \frac{\sin z}{z} \tag{3.32}$$

$$y_\ell(z) = -(-z)^\ell \left(\frac{1}{z}\frac{\mathrm{d}}{\mathrm{d}z}\right)^\ell \frac{\cos z}{z} \tag{3.33}$$

The associated Legendre polynomial $P_\ell^m(\cos\theta)$ is part of the solution of Laplace's equation in spherical coordinates, the angular portion $P_\ell^m(\cos\theta)e^{-im\phi}$ of which com-

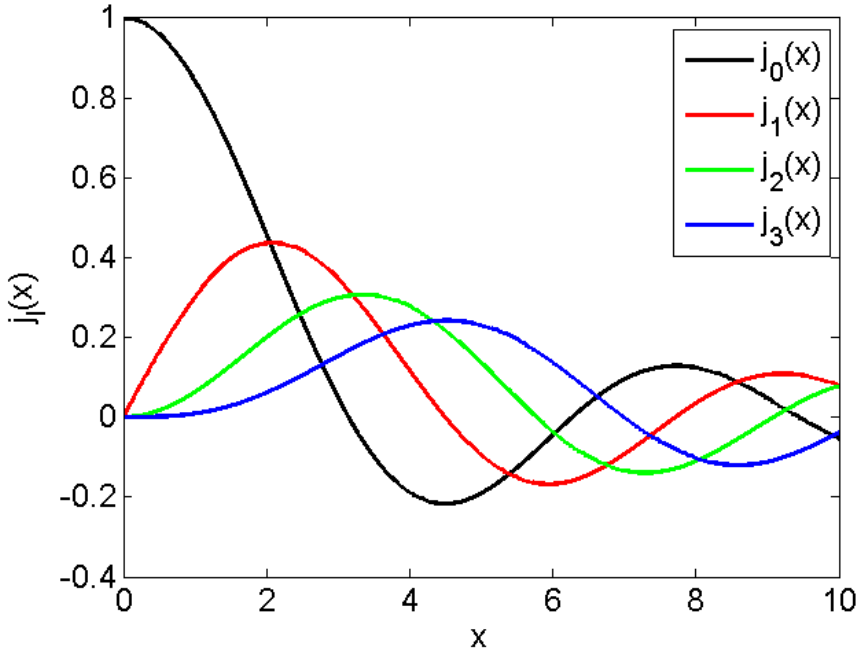

(a)

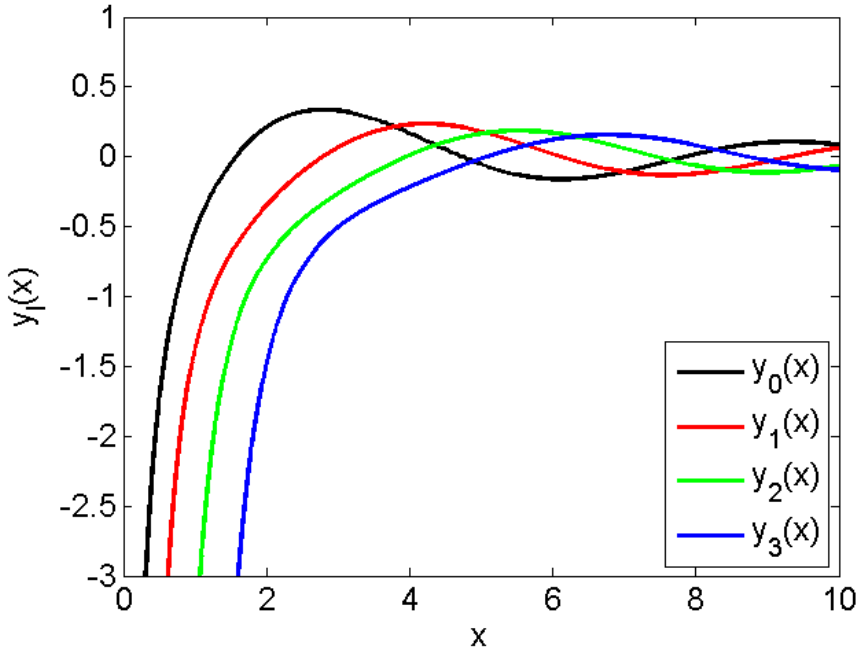

(b)

Figure 3.1: Examples of (a) spherical Bessel functions of the first kind and (b) spherical Neumann functions with orders $\ell = 0,\ 1,\ 2$, and 3.

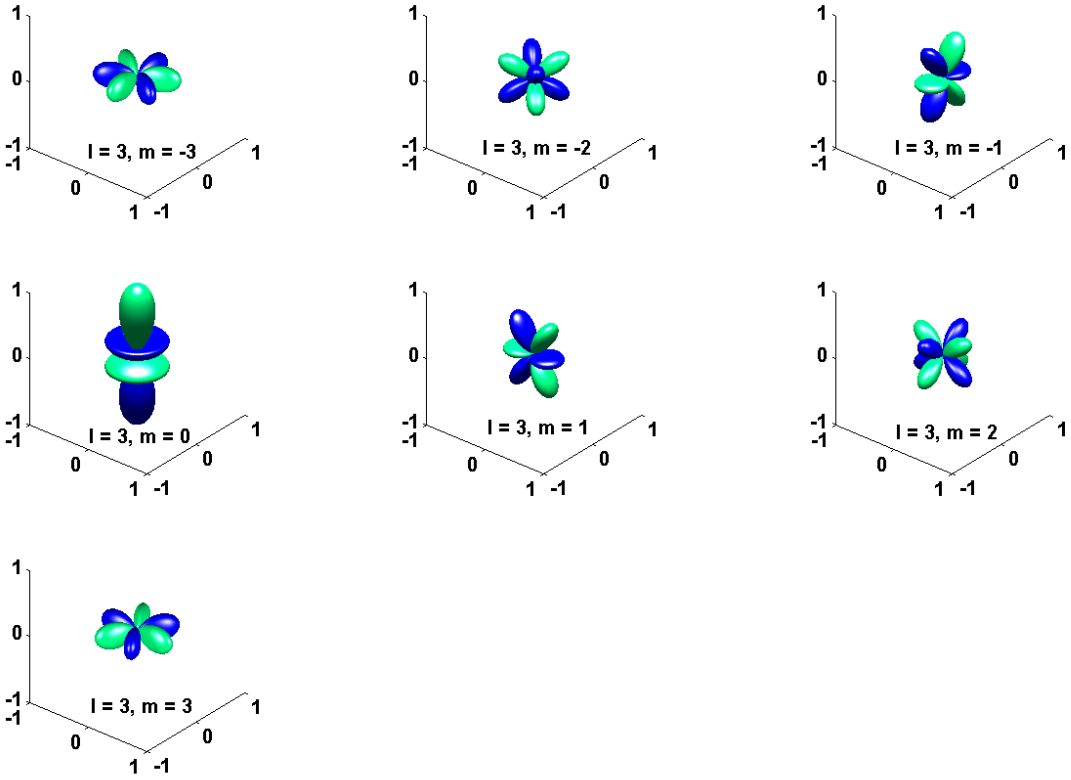

Figure 3.2: Spherical harmonics for a degree $\ell = 3$. The colour mapping was chosen such that positive values are in teal, while negative ones are in blue.

prises what is otherwise known as spherical harmonics (e.g. Figure 3.2). When computing $P_\ell^m(\cos\theta)$ for analytical solutions with large m and ℓ, as in the case of spherically symmetric WGM microcavities, the number of bits for the assigned floating-point number often becomes insufficient. A typical whispering-gallery mode circumnavigating a 30-μm radius silica microsphere in water at 780.911 nm with $m = 340$ [14] would have $P_{340}^{340}(0.5) = 2.01 \times 10^{794}$. This is well above the IEEE 754 double-precision binary floating-point format (binary64) maximum of $\sim 1.80 \times 10^{308}$, therefore requiring a normalization procedure in order to feasibly generate field data and resonance parameters. One prevalent avenue in geodesy is the forward column recursion algorithm [83], which initially defines the polynomial in Abramowitz and Stegun notation [84] as

$$\begin{aligned}\bar{P}_{\ell m}(\theta) &= (-1)^m \bar{P}_\ell^m(\theta) \\ &= (-1)^m \sqrt{\frac{k(2\ell+1)(\ell-m)!}{(\ell+m)!}} P_\ell^m(\theta)\end{aligned} \tag{3.34}$$

where $k = 1$ if $m = 0$ and $k = 2$ if $m > 0$. The recursion itself involves a relation between $\bar{P}_{\ell m}(\theta)$ and two preceding $\bar{P}$'s of degrees $\ell - 1$ as well as $\ell - 2$ for $\ell > m$ [85]:

$$\bar{P}_{\ell m}(\theta) = \alpha_{\ell m} \cos\theta \bar{P}_{\ell-1,m}(\theta) - \beta_{\ell m} \bar{P}_{\ell-2,m}(\theta) \tag{3.35}$$

where

$$\alpha_{\ell m} = \sqrt{\frac{(2\ell-1)(2\ell+1)}{(\ell-m)(\ell+m)}} \tag{3.36}$$

$$\beta_{\ell m} = \sqrt{\frac{(2\ell+1)(\ell+m-1)(\ell-m-1)}{(\ell-m)(\ell+m)(2\ell-3)}} \tag{3.37}$$

Polynomials $\bar{P}_{\ell m}(\theta)$ obeying $\ell = m$ belong to sectoral harmonics. Given a $\bar{P}_{0,0}(\theta) = 1$ and $\bar{P}_{1,1}(\theta) = \sqrt{3}\sin\theta$, these can be specified by

$$\bar{P}_{mm}(\theta) = (\sin\theta)^m \sqrt{3} \prod_{n=2}^{m} \sqrt{\frac{2n+1}{2n}} \tag{3.38}$$

and can be utilized alongside (3.35) to specify any associated Legendre polynomial of a desired degree $\ell \geq m$ and order $m \geq 2$. A diagram illustrating the calculation sequence can be viewed in Figure 3.3, while select $P_\ell^m(\cos\theta)$ and $\bar{P}_\ell^m(\cos\theta)$ are plotted in Figure 3.4.

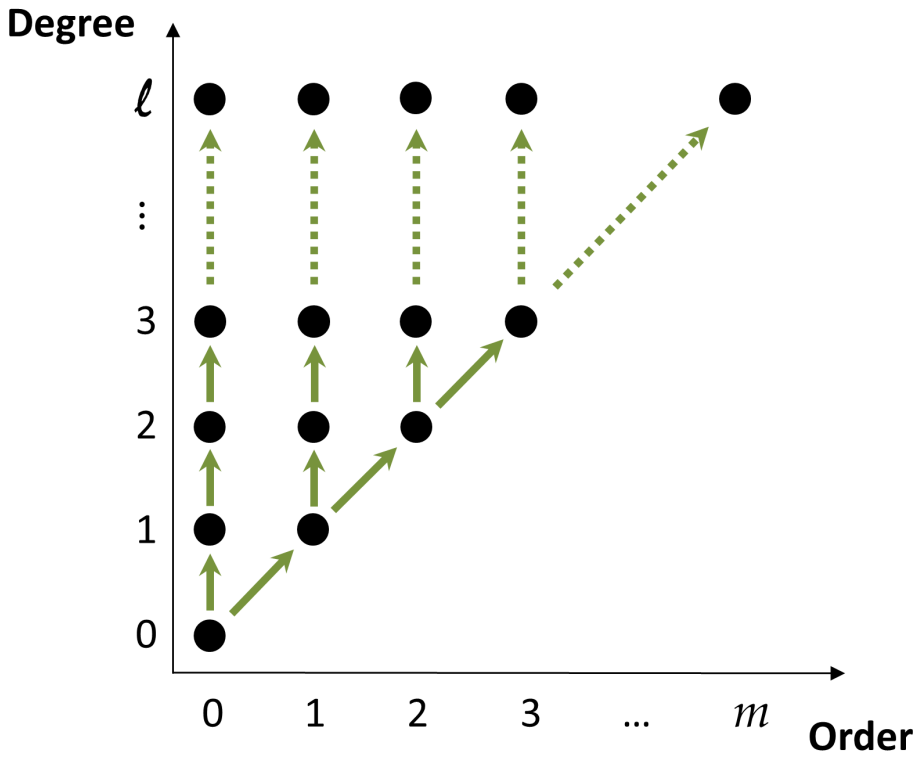

Figure 3.3: Forward column recursion algorithm for calculating the fully normalized associated Legendre polynomial, $\bar{P}_{\ell m}(\theta)$.

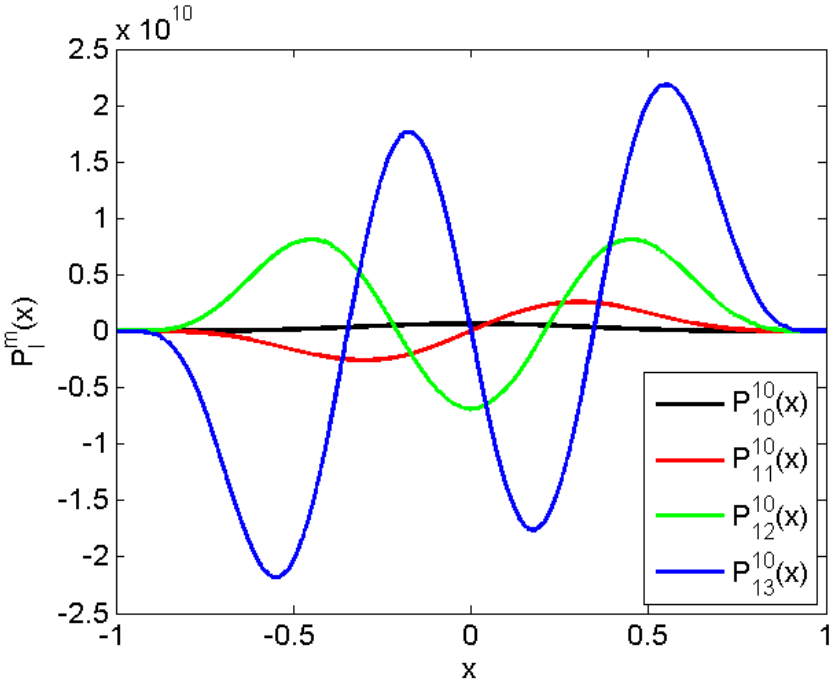

(a)

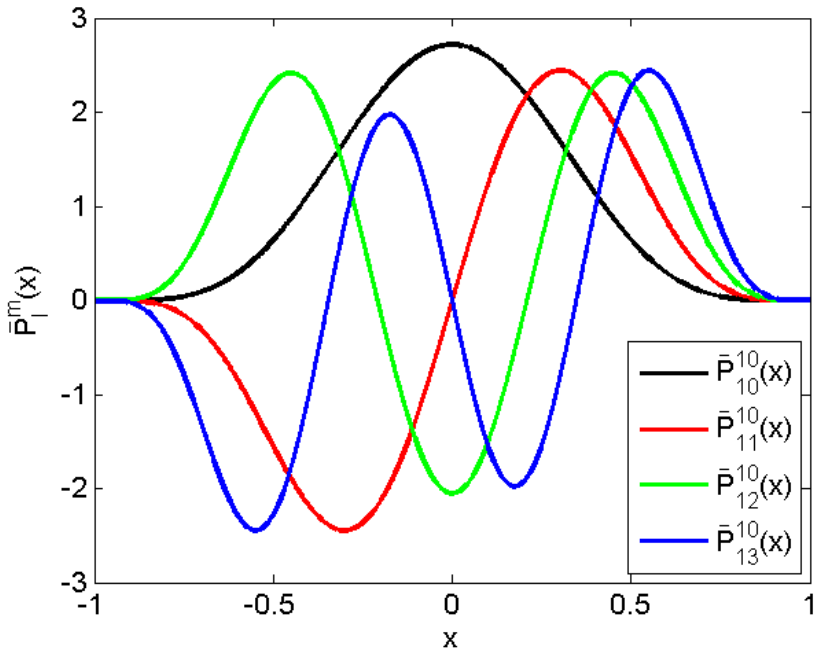

(b)

Figure 3.4: Scale contrast between (a) associated Legendre polynomials and (b) fully normalized Legendre polynomials with order $m = 10$ and degrees $\ell = 10,\ 11,\ 12$, as well as 13.

3.2 Scalar Finite Difference Approximation

For any analytic multivariate function which has a certain continuous differentiability there exists a Taylor series that converges to it [86]. The polynomial basis of the Taylor series expansion is a familiar choice amidst a multitude of alternatives for approximation, one example being the Fourier series expansion better suited to periodic functions.

Let us consider a ρ-z cross-section in cylindrical coordinates. In order to construct a finite difference matrix $\mathbf{V}$ by which one can extract eigenmodes and eigenwavelengths, we must form a stencil in the local neighbourhood of a point (ρ_i, z_j) as well as derive a relationship between a component $E_x(\rho_i, z_j)$ (that is, $x = \rho$, z, or ϕ) and its proximate $E_x(\rho_{i+1}, z_j)$, $E_x(\rho_{i-1}, z_j)$, $E_x(\rho_i, z_{j+1})$, $E_x(\rho_i, z_{j-1})$, $E_x(\rho_{i+1}, z_{j+1})$, and $E_x(\rho_{i-1}, z_{j-1})$ in the nodal group. Choosing a 7-point stencil in a $M \times N$ computation window (with dimensions tied to ρ and z, respectively), the six two-dimensional Taylor series in a homogeneous region are

$$E_x(\rho_{i+1}, z_j) = E_x(\rho_i, z_j) + \Delta\rho_{i+1}\frac{\partial}{\partial\rho}E_x(\rho_i, z_j) + \frac{1}{2!}\Delta\rho_{i+1}^2\frac{\partial^2}{\partial\rho^2}E_x(\rho_i, z_j) + ... \quad (3.39)$$

$$E_x(\rho_{i-1}, z_j) = E_x(\rho_i, z_j) - \Delta\rho_{i-1}\frac{\partial}{\partial\rho}E_x(\rho_i, z_j) + \frac{1}{2!}\Delta\rho_{i-1}^2\frac{\partial^2}{\partial\rho^2}E_x(\rho_i, z_j) + ... \quad (3.40)$$

$$E_x(\rho_i, z_{j+1}) = E_x(\rho_i, z_j) + \Delta z_{j+1}\frac{\partial}{\partial z}E_x(\rho_i, z_j) + \frac{1}{2!}\Delta z_{j+1}^2\frac{\partial^2}{\partial z^2}E_x(\rho_i, z_j) + ... \quad (3.41)$$

$$E_x(\rho_i, z_{j-1}) = E_x(\rho_i, z_j) - \Delta z_{j-1}\frac{\partial}{\partial z}E_x(\rho_i, z_j) + \frac{1}{2!}\Delta z_{j-1}^2\frac{\partial^2}{\partial z^2}E_x(\rho_i, z_j) + ... \quad (3.42)$$

$$\begin{aligned} E_x(\rho_{i+1}, z_{j+1}) = {} & E_x(\rho_i, z_j) + \Delta\rho_{i+1}\frac{\partial}{\partial\rho}E_x(\rho_i, z_j) + \Delta z_{j+1}\frac{\partial}{\partial z}E_x(\rho_i, z_j) \\ & + \frac{1}{2!}\Delta\rho_{i+1}^2\frac{\partial^2}{\partial\rho^2}E_x(\rho_i, z_j) + \frac{2}{2!}\Delta\rho_{i+1}\Delta z_{j+1}\frac{\partial^2}{\partial\rho\partial z}E_x(\rho_i, z_j) \\ & + \frac{1}{2!}\Delta z_{j+1}^2\frac{\partial^2}{\partial z^2}E_x(\rho_i, z_j) + ... \end{aligned} \quad (3.43)$$

$$\begin{aligned} E_x(\rho_{i-1}, z_{j-1}) = {} & E_x(\rho_i, z_j) - \Delta\rho_{i-1}\frac{\partial}{\partial\rho}E_x(\rho_i, z_j) - \Delta z_{j-1}\frac{\partial}{\partial z}E_x(\rho_i, z_j) \\ & + \frac{1}{2!}\Delta\rho_{i-1}^2\frac{\partial^2}{\partial\rho^2}E_x(\rho_i, z_j) + \frac{2}{2!}\Delta\rho_{i-1}\Delta z_{j-1}\frac{\partial^2}{\partial\rho\partial z}E_x(\rho_i, z_j) \\ & + \frac{1}{2!}\Delta z_{j-1}^2\frac{\partial^2}{\partial z^2}E_x(\rho_i, z_j) + ... \end{aligned} \quad (3.44)$$

In principle, a finite difference scheme with stencil symmetry, $\Delta\rho_{i+1} = \Delta\rho_{i-1}$, $\Delta z_{j+1} = \Delta z_{j-1}$, and whose dominant source of error is its truncation error should have an effective convergence rate of 2 if the third and higher-order derivative terms of the central $E_x(\rho_i, z_j)$ in each series are truncated. The assembled Taylor expansions should then serve to express $E_{x,\mathrm{C}} = E_x(\rho_i, z_j)$ and its various derivatives in terms of the nearby fields $E_{x,\mathrm{E}} = E_x(\rho_{i+1}, z_j)$, $E_{x,\mathrm{W}} = E_x(\rho_{i-1}, z_j)$, $E_{x,\mathrm{N}} = E_x(\rho_i, z_{j+1})$, $E_{x,\mathrm{S}} = E_x(\rho_i, z_{j-1})$, $E_{x,\mathrm{NE}} = E_x(\rho_{i+1}, z_{j+1})$, and $E_{x,\mathrm{SW}} = E_x(\rho_{i-1}, z_{j-1})$:

$$\begin{bmatrix} E_{x,\mathrm{E}} \\ E_{x,\mathrm{W}} \\ E_{x,\mathrm{N}} \\ E_{x,\mathrm{S}} \\ E_{x,\mathrm{NE}} \\ E_{x,\mathrm{SW}} \end{bmatrix} = \begin{bmatrix} 1 & \Delta\rho_{i+1} & 0 & \frac{\Delta\rho_{i+1}^2}{2} & 0 & 0 \\ 1 & -\Delta\rho_{i-1} & 0 & \frac{\Delta\rho_{i-1}^2}{2} & 0 & 0 \\ 1 & 0 & \Delta z_{j+1} & 0 & 0 & \frac{\Delta z_{j+1}^2}{2} \\ 1 & 0 & -\Delta z_{j-1} & 0 & 0 & \frac{\Delta z_{j-1}^2}{2} \\ 1 & \Delta\rho_{i+1} & \Delta z_{j+1} & \frac{\Delta\rho_{i+1}^2}{2} & \Delta\rho_{i+1}\Delta z_{j+1} & \frac{\Delta z_{j+1}^2}{2} \\ 1 & -\Delta\rho_{i-1} & -\Delta z_{j-1} & \frac{\Delta\rho_{i-1}^2}{2} & \Delta\rho_{i-1}\Delta z_{j-1} & \frac{\Delta z_{j-1}^2}{2} \end{bmatrix} \begin{bmatrix} E_{x,\mathrm{C}} \\ \frac{\partial E_{x,\mathrm{C}}}{\partial\rho} \\ \frac{\partial E_{x,\mathrm{C}}}{\partial z} \\ \frac{\partial^2 E_{x,\mathrm{C}}}{\partial\rho^2} \\ \frac{\partial^2 E_{x,\mathrm{C}}}{\partial\rho\partial z} \\ \frac{\partial^2 E_{x,\mathrm{C}}}{\partial z^2} \end{bmatrix}$$

$$= \mathbf{S}_{i,j} \begin{bmatrix} E_{x,\mathrm{C}} \\ \frac{\partial E_{x,\mathrm{C}}}{\partial\rho} \\ \frac{\partial E_{x,\mathrm{C}}}{\partial z} \\ \frac{\partial^2 E_{x,\mathrm{C}}}{\partial\rho^2} \\ \frac{\partial^2 E_{x,\mathrm{C}}}{\partial\rho\partial z} \\ \frac{\partial^2 E_{x,\mathrm{C}}}{\partial z^2} \end{bmatrix} \quad (3.45)$$

If $a_{i,j} = \Delta\rho_{i+1}\Delta z_{j+1}$, $b_{i,j} = \Delta\rho_{i-1}\Delta z_{j-1}$, $c_{i,j} = \Delta\rho_{i-1}\Delta z_{j+1}$, $d_{i,j} = \Delta\rho_{i+1}\Delta z_{j-1}$, $e_{i,j} = \Delta\rho_{i+1} + \Delta\rho_{i-1}$, $f_{i,j} = \Delta\rho_{i+1} - \Delta\rho_{i-1}$, $g_{i,j} = \Delta z_{j+1} + \Delta z_{j-1}$, and $h_{i,j} = \Delta z_{j+1} - \Delta z_{j-1}$, inverting $\mathbf{S}_{i,j}$ brings about

$$
\begin{bmatrix} E_{x,\mathrm{C}} \\ \frac{\partial E_{x,\mathrm{C}}}{\partial \rho} \\ \frac{\partial E_{x,\mathrm{C}}}{\partial z} \\ \frac{\partial^2 E_{x,\mathrm{C}}}{\partial \rho^2} \\ \frac{\partial^2 E_{x,\mathrm{C}}}{\partial \rho \partial z} \\ \frac{\partial^2 E_{x,\mathrm{C}}}{\partial z^2} \end{bmatrix} = \begin{bmatrix} -\frac{b_{i,j}}{a_{i,j}-b_{i,j}} & \frac{a_{i,j}}{a_{i,j}-b_{i,j}} & -\frac{b_{i,j}}{a_{i,j}-b_{i,j}} \\ \frac{c_{i,j}-d_{i,j}}{e_{i,j}(a_{i,j}-b_{i,j})} & \frac{-c_{i,j}+d_{i,j}}{e_{i,j}(a_{i,j}-b_{i,j})} & -\frac{f_{i,j}\Delta z_{j-1}}{\Delta\rho_{i+1}(a_{i,j}-b_{i,j})} \\ -\frac{\Delta\rho_{i-1}h_{i,j}}{\Delta z_{j+1}(a_{i,j}-b_{i,j})} & \frac{\Delta\rho_{i+1}h_{i,j}}{\Delta z_{j-1}(a_{i,j}-b_{i,j})} & \frac{-c_{i,j}+d_{i,j}}{g_{i,j}(a_{i,j}-b_{i,j})} \\ \frac{2g_{i,j}}{e_{i,j}(a_{i,j}-b_{i,j})} & -\frac{2g_{i,j}}{e_{i,j}(a_{i,j}-b_{i,j})} & \frac{2\Delta z_{j-1}}{\Delta\rho_{i+1}(a_{i,j}-b_{i,j})} \\ -\frac{1}{a_{i,j}-b_{i,j}} & \frac{1}{a_{i,j}-b_{i,j}} & -\frac{1}{a_{i,j}-b_{i,j}} \\ \frac{2\Delta\rho_{i-1}}{\Delta z_{j+1}(a_{i,j}-b_{i,j})} & -\frac{2\Delta\rho_{i+1}}{\Delta z_{j-1}(a_{i,j}-b_{i,j})} & \frac{2e_{i,j}}{g_{i,j}(a_{i,j}-b_{i,j})} \end{bmatrix}
$$

$$
\begin{bmatrix} \frac{a_{i,j}}{a_{i,j}-b_{i,j}} & \frac{b_{i,j}}{a_{i,j}-b_{i,j}} & -\frac{a_{i,j}}{a_{i,j}-b_{i,j}} \\ \frac{f_{i,j}\Delta z_{j+1}}{\Delta\rho_{i-1}(a_{i,j}-b_{i,j})} & \frac{f_{i,j}\Delta z_{j-1}}{\Delta\rho_{i+1}(a_{i,j}-b_{i,j})} & -\frac{f_{i,j}\Delta z_{j+1}}{\Delta\rho_{i-1}(a_{i,j}-b_{i,j})} \\ \frac{c_{i,j}-d_{i,j}}{g_{i,j}(a_{i,j}-b_{i,j})} & \frac{\Delta\rho_{i-1}h_{i,j}}{\Delta z_{j+1}(a_{i,j}-b_{i,j})} & -\frac{\Delta\rho_{i+1}h_{i,j}}{\Delta z_{j-1}(a_{i,j}-b_{i,j})} \\ -\frac{2\Delta z_{j+1}}{\Delta\rho_{i-1}(a_{i,j}-b_{i,j})} & -\frac{2\Delta z_{j-1}}{\Delta\rho_{i+1}(a_{i,j}-b_{i,j})} & \frac{2\Delta z_{j+1}}{\Delta\rho_{i-1}(a_{i,j}-b_{i,j})} \\ \frac{1}{a_{i,j}-b_{i,j}} & \frac{1}{a_{i,j}-b_{i,j}} & -\frac{1}{a_{i,j}-b_{i,j}} \\ -\frac{2e_{i,j}}{g_{i,j}(a_{i,j}-b_{i,j})} & -\frac{2\Delta\rho_{i-1}}{\Delta z_{j+1}(a_{i,j}-b_{i,j})} & \frac{2\Delta\rho_{i+1}}{\Delta z_{j-1}(a_{i,j}-b_{i,j})} \end{bmatrix} \begin{bmatrix} E_{x,\mathrm{E}} \\ E_{x,\mathrm{W}} \\ E_{x,\mathrm{N}} \\ E_{x,\mathrm{S}} \\ E_{x,\mathrm{NE}} \\ E_{x,\mathrm{SW}} \end{bmatrix}
$$

$$
= \mathbf{S}_{i,j}^{-1} \begin{bmatrix} E_{x,\mathrm{E}} \\ E_{x,\mathrm{W}} \\ E_{x,\mathrm{N}} \\ E_{x,\mathrm{S}} \\ E_{x,\mathrm{NE}} \\ E_{x,\mathrm{SW}} \end{bmatrix}
$$

$$
= \begin{bmatrix} \mathrm{m}_{11}^{i,j} & \mathrm{m}_{12}^{i,j} & \mathrm{m}_{13}^{i,j} & \mathrm{m}_{14}^{i,j} & \mathrm{m}_{15}^{i,j} & \mathrm{m}_{16}^{i,j} \\ \mathrm{m}_{21}^{i,j} & \mathrm{m}_{22}^{i,j} & \mathrm{m}_{23}^{i,j} & \mathrm{m}_{24}^{i,j} & \mathrm{m}_{25}^{i,j} & \mathrm{m}_{26}^{i,j} \\ \mathrm{m}_{31}^{i,j} & \mathrm{m}_{32}^{i,j} & \mathrm{m}_{33}^{i,j} & \mathrm{m}_{34}^{i,j} & \mathrm{m}_{35}^{i,j} & \mathrm{m}_{36}^{i,j} \\ \mathrm{m}_{41}^{i,j} & \mathrm{m}_{42}^{i,j} & \mathrm{m}_{43}^{i,j} & \mathrm{m}_{44}^{i,j} & \mathrm{m}_{45}^{i,j} & \mathrm{m}_{46}^{i,j} \\ \mathrm{m}_{51}^{i,j} & \mathrm{m}_{52}^{i,j} & \mathrm{m}_{53}^{i,j} & \mathrm{m}_{54}^{i,j} & \mathrm{m}_{55}^{i,j} & \mathrm{m}_{56}^{i,j} \\ \mathrm{m}_{61}^{i,j} & \mathrm{m}_{62}^{i,j} & \mathrm{m}_{63}^{i,j} & \mathrm{m}_{64}^{i,j} & \mathrm{m}_{65}^{i,j} & \mathrm{m}_{66}^{i,j} \end{bmatrix} \begin{bmatrix} E_{x,\mathrm{E}} \\ E_{x,\mathrm{W}} \\ E_{x,\mathrm{N}} \\ E_{x,\mathrm{S}} \\ E_{x,\mathrm{NE}} \\ E_{x,\mathrm{SW}} \end{bmatrix}
$$

$$
= \mathbf{M}_{i,j} \begin{bmatrix} E_{x,\mathrm{E}} \\ E_{x,\mathrm{W}} \\ E_{x,\mathrm{N}} \\ E_{x,\mathrm{S}} \\ E_{x,\mathrm{NE}} \\ E_{x,\mathrm{SW}} \end{bmatrix} \tag{3.46}
$$

appearing irreducible in complexity in view of the operators demanded by the wave equation and the constrained dimension of the vector space. Subsequently, elements of $\mathbf{M}_{i,j}$ for $i = 1, 2, ..., M$ and $j = 1, 2, ..., N$ are brought together in $\mathbf{V}$-matrix construction. Starting from the scalar Helmholtz formula,

$$\begin{aligned}
\nabla^2 E_x + k_o^2 \epsilon_r E_x &= 0 \\
\frac{\partial^2 E_x}{\partial \rho^2} + \frac{1}{\rho}\frac{\partial E_x}{\partial \rho} + \frac{\partial^2 E_x}{\partial z^2} + \left(k_o^2 \epsilon_r - \frac{m^2}{\rho^2}\right) E_x &= 0 \\
\frac{1}{\epsilon_r}\frac{\partial^2 E_x}{\partial \rho^2} + \frac{1}{\epsilon_r \rho}\frac{\partial E_x}{\partial \rho} + \frac{1}{\epsilon_r}\frac{\partial^2 E_x}{\partial z^2} - \frac{m^2}{\epsilon_r \rho^2} E_x &= -k_o^2 E_x
\end{aligned}$$

$$\downarrow$$

$$\frac{1}{\epsilon_r^{i,j}} \begin{bmatrix} \mathrm{m}_{41}^{i,j} + \frac{\mathrm{m}_{21}^{i,j}}{\rho_i} + \mathrm{m}_{61}^{i,j} \\ \mathrm{m}_{42}^{i,j} + \frac{\mathrm{m}_{22}^{i,j}}{\rho_i} + \mathrm{m}_{62}^{i,j} \\ \mathrm{m}_{43}^{i,j} + \frac{\mathrm{m}_{23}^{i,j}}{\rho_i} + \mathrm{m}_{63}^{i,j} \\ \mathrm{m}_{44}^{i,j} + \frac{\mathrm{m}_{24}^{i,j}}{\rho_i} + \mathrm{m}_{64}^{i,j} \\ \mathrm{m}_{45}^{i,j} + \frac{\mathrm{m}_{25}^{i,j}}{\rho_i} + \mathrm{m}_{65}^{i,j} \\ \mathrm{m}_{46}^{i,j} + \frac{\mathrm{m}_{26}^{i,j}}{\rho_i} + \mathrm{m}_{66}^{i,j} \end{bmatrix}^{\mathrm{T}} \begin{bmatrix} E_{x,\mathrm{E}} \\ E_{x,\mathrm{W}} \\ E_{x,\mathrm{N}} \\ E_{x,\mathrm{S}} \\ E_{x,\mathrm{NE}} \\ E_{x,\mathrm{SW}} \end{bmatrix} - \frac{m^2}{\epsilon_r^{i,j} \rho_i^2} E_{x,\mathrm{C}} = -k_o^2 E_{x,\mathrm{C}}$$

which will compose $\mathbf{V}$ in

$$\mathbf{V}\ \mathbf{E} = \mathbf{V} \begin{bmatrix} E_x|_{(1,1)} \\ \vdots \\ E_x|_{(M,N)} \end{bmatrix} = -k_o^2 \begin{bmatrix} E_x|_{(1,1)} \\ \vdots \\ E_x|_{(M,N)} \end{bmatrix} \tag{3.47}$$

The layout of entries v_{11}, ..., v_{MN} within $\mathbf{V}$ is vast, yet the six off-diagonals can be elegantly summarized as

$$E_{x,\mathrm{E}} - 1^{\mathrm{st}} \text{ Upper Off-Diagonal}: \ \mathrm{v}_{12},\ \mathrm{v}_{23},\ ...,\ \mathrm{v}_{(M\times N-1)(M\times N)} \tag{3.48}$$

$$E_{x,\mathrm{N}} - 2^{\mathrm{nd}} \text{ Upper Off-Diagonal}: \ \mathrm{v}_{1(M+1)},\ \mathrm{v}_{2(M+2)},\ ...,\ \mathrm{v}_{(M\times N-M)(M\times N)} \tag{3.49}$$

$$E_{x,\mathrm{NE}} - 3^{\mathrm{rd}} \text{ Upper Off-Diagonal}: \ \mathrm{v}_{1(M+2)},\ \mathrm{v}_{2(M+3)},\ ...,\ \mathrm{v}_{(M\times N-M-1)(M\times N)} \tag{3.50}$$

$$E_{x,\mathrm{W}} - 1^{\mathrm{st}} \text{ Lower Off-Diagonal}: \ \mathrm{v}_{21},\ \mathrm{v}_{32},\ ...,\ \mathrm{v}_{(M\times N)(M\times N-1)} \tag{3.51}$$

$$E_{x,\mathrm{S}} - 2^{\mathrm{nd}} \text{ Lower Off-Diagonal}: \ \mathrm{v}_{(M+1)1},\ \mathrm{v}_{(M+2)2},\ \ldots,\ \mathrm{v}_{(M\times N)(M\times N-M)} \tag{3.52}$$

$$E_{x,\mathrm{SW}} - 3^{\mathrm{rd}} \text{ Lower Off-Diagonal}: \ \mathrm{v}_{(M+2)1},\ \mathrm{v}_{(M+3)2},\ \ldots,\ \mathrm{v}_{(M\times N)(M\times N-M-1)} \tag{3.53}$$

with the caveat that, when there is no wrap-around boundary condition and the E-field beyond the analysis region decays to 0, we must enforce

$$\mathrm{v}_{(M\times n)(M\times n+1)} = \mathrm{v}_{(M\times n+1)(M\times n)} = 0 \tag{3.54}$$

and

$$\mathrm{v}_{(M\times n)(M\times n+M+1)} = \mathrm{v}_{(M\times n+M+1)(M\times n)} = 0 \tag{3.55}$$

where n is an integer ranging from 1 to $N-1$. These boundary conditions are the simplest to implement, however, they limit the assessment of radiative loss as they mimic a perfect electrical conducting wall. Future revisions of this truncation would comprise the creation of an artificial absorbing or perfectly matched layer (PML) that attenuates EM waves when they near the computation window edge.

3.3 Full-Vector Finite Difference Formalism

In [27], Y.-C. Chiang *et al.* developed a numerical technique for acquiring full-vectorial optical modes of a step-index waveguide. By combining a local coordinate transformation with matched interface conditions, the Taylor series expansion for the finite difference expressions was suitably modified to admit the permittivity transitions along linear oblique or curved dielectric boundaries. Two wave equations for field components, say E_ρ and E_z, can then be coupled to one another according to the four conditions outlined in Section 3.1.1

The above referenced treatment can be extended to WGM geometries, granted that rotational energy (i.e. the cavity's effective potential $V_{\mathrm{eff}} = k_o^2(1-\epsilon_r) + \frac{\ell(\ell+1)}{\rho^2}$) be included and what was once applied to straight trajectories of trapped photons is retrofitted for curvilinear paths. For a nodal group with stencil points that lie in multiple dielectric media as in Figure 3.5, we are still required to adopt a piecemeal Taylor series expansion broken into five steps:

1. Relating the fields $E_{\rho,\mathrm{C}}$ and $E_{z,\mathrm{C}}$ to those at the interface, $E_\rho|_L$ and $E_z|_L$, located along 1 of 6 possible directions $\left(\hat{\rho},\ \hat{z},\ \frac{1}{\sqrt{\Delta\rho_{i+1}^2+\Delta z_{j+1}^2}}(\Delta\rho_{i+1}\hat{\rho}+\Delta z_{j+1}\hat{z}),\right.$ $-\hat{\rho},\ -\hat{z}$, or $\left.-\frac{1}{\sqrt{\Delta\rho_{i-1}^2+\Delta z_{j-1}^2}}(\Delta\rho_{i-1}\hat{\rho}+\Delta z_{j-1}\hat{z})\right)$.

2. Applying a local coordinate transformation. For a linear oblique interface, this is done through a rotation matrix operator $\mathbf{R}_{i,j}(-\theta)$ with a fixed angle θ between the ρ-axis and the normal vector $\hat{n}$ of the surface.

3. Transferring the field quantities from one medium to another via the interface continuity relations. This will necessarily implicate the first and second-order derivatives of the fields.

4. Applying an inverse local coordinate transformation. Given Step 2, the operator must be $\mathbf{R}_{i,j}(\theta)$.

5. Expressing the fields $E_\rho|_R$ and $E_z|_R$ on the other side of the interface in terms of those at the outer node ($E_{\rho,\mathrm{E}}$, $E_{z,\mathrm{E}}$, $E_{\rho,\mathrm{N}}$, $E_{z,\mathrm{N}}$, $E_{\rho,\mathrm{NE}}$, $E_{z,\mathrm{NE}}$, $E_{\rho,\mathrm{W}}$, $E_{z,\mathrm{W}}$, $E_{\rho,\mathrm{S}}$, $E_{z,\mathrm{S}}$, $E_{\rho,\mathrm{SW}}$, and/or $E_{z,\mathrm{SW}}$).

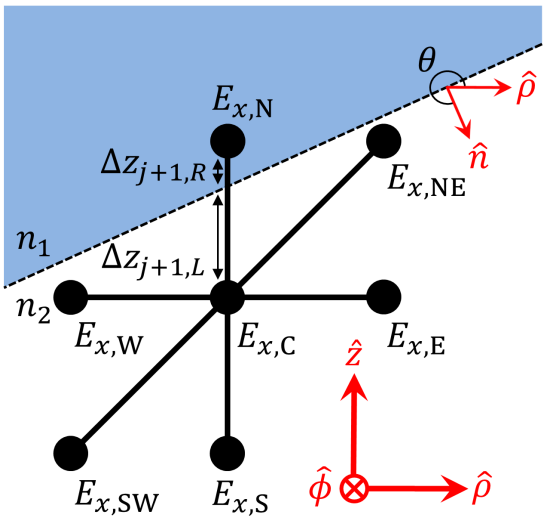

Figure 3.5: Microcavity cross section and the 7-point stencil (applicable to a pair of field components, e.g. E_x where $x = \rho$ or z) for a linear oblique interface. Note $n_1^2 = \epsilon_R$ and $n_2^2 = \epsilon_L$

Unlike the previous section the Taylor series (3.39)-(3.44) are not sufficient to solve for full-vectorial eigenmodes. Through neglection of third as well as higher-order terms, the differentiated Taylor series for a field component E_x (with $x = \rho$ or z) are

$$\begin{aligned}\frac{\partial E_{x,\mathrm{E}}}{\partial \rho} = \frac{\partial E_x(\rho_{i+1}, z_j)}{\partial \rho} &= \frac{\partial E_x(\rho_i, z_j)}{\partial \rho} + \Delta\rho_{i+1}\frac{\partial^2 E_x(\rho_i, z_j)}{\partial \rho^2} \\ &= \frac{\partial E_{x,\mathrm{C}}}{\partial \rho} + \Delta\rho_{i+1}\frac{\partial^2 E_{x,\mathrm{C}}}{\partial \rho^2} \qquad (3.56)\end{aligned}$$

$$\frac{\partial E_{x,\mathrm{E}}}{\partial z} = \frac{\partial E_{x,\mathrm{C}}}{\partial z} + \Delta\rho_{i+1}\frac{\partial^2 E_{x,\mathrm{C}}}{\partial \rho \partial z} \qquad (3.57)$$

$$\frac{\partial^2 E_{x,\mathrm{E}}}{\partial \rho^2} = \frac{\partial^2 E_{x,\mathrm{C}}}{\partial \rho^2} \qquad (3.58)$$

$$\frac{\partial^2 E_{x,\mathrm{E}}}{\partial \rho \partial z} = \frac{\partial^2 E_{x,\mathrm{C}}}{\partial \rho \partial z} \qquad (3.59)$$

$$\frac{\partial^2 E_{x,\mathrm{E}}}{\partial z^2} = \frac{\partial^2 E_{x,\mathrm{C}}}{\partial z^2} \qquad (3.60)$$

$$\begin{aligned}\frac{\partial E_{x,\mathrm{W}}}{\partial \rho} = \frac{\partial E_x(\rho_{i-1}, z_j)}{\partial \rho} &= \frac{\partial E_x(\rho_i, z_j)}{\partial \rho} - \Delta\rho_{i-1}\frac{\partial^2 E_x(\rho_i, z_j)}{\partial \rho^2} \\ &= \frac{\partial E_{x,\mathrm{C}}}{\partial \rho} - \Delta\rho_{i-1}\frac{\partial^2 E_{x,\mathrm{C}}}{\partial \rho^2} \qquad (3.61)\end{aligned}$$

$$\frac{\partial E_{x,\mathrm{W}}}{\partial z} = \frac{\partial E_{x,\mathrm{C}}}{\partial z} - \Delta\rho_{i-1}\frac{\partial^2 E_{x,\mathrm{C}}}{\partial \rho \partial z} \qquad (3.62)$$

$$\frac{\partial^2 E_{x,\mathrm{W}}}{\partial \rho^2} = \frac{\partial^2 E_{x,\mathrm{C}}}{\partial \rho^2} \qquad (3.63)$$

$$\frac{\partial^2 E_{x,\mathrm{W}}}{\partial \rho \partial z} = \frac{\partial^2 E_{x,\mathrm{C}}}{\partial \rho \partial z} \qquad (3.64)$$

$$\frac{\partial^2 E_{x,\mathrm{W}}}{\partial z^2} = \frac{\partial^2 E_{x,\mathrm{C}}}{\partial z^2} \qquad (3.65)$$

$$\frac{\partial E_{x,\mathrm{N}}}{\partial \rho} = \frac{\partial E_x(\rho_i, z_{j+1})}{\partial \rho} = \frac{\partial E_x(\rho_i, z_j)}{\partial \rho} + \Delta z_{j+1} \frac{\partial^2 E_x(\rho_i, z_j)}{\partial \rho \partial z}$$

$$= \frac{\partial E_{x,\mathrm{C}}}{\partial \rho} + \Delta z_{j+1} \frac{\partial^2 E_{x,\mathrm{C}}}{\partial \rho \partial z} \tag{3.66}$$

$$\frac{\partial E_{x,\mathrm{N}}}{\partial z} = \frac{\partial E_{x,\mathrm{C}}}{\partial z} + \Delta z_{j+1} \frac{\partial^2 E_{x,\mathrm{C}}}{\partial z^2} \tag{3.67}$$

$$\frac{\partial^2 E_{x,\mathrm{N}}}{\partial \rho^2} = \frac{\partial^2 E_{x,\mathrm{C}}}{\partial \rho^2} \tag{3.68}$$

$$\frac{\partial^2 E_{x,\mathrm{N}}}{\partial \rho \partial z} = \frac{\partial^2 E_{x,\mathrm{C}}}{\partial \rho \partial z} \tag{3.69}$$

$$\frac{\partial^2 E_{x,\mathrm{N}}}{\partial z^2} = \frac{\partial^2 E_{x,\mathrm{C}}}{\partial z^2} \tag{3.70}$$

$$\frac{\partial E_{x,\mathrm{S}}}{\partial \rho} = \frac{\partial E_x(\rho_i, z_{j-1})}{\partial \rho} = \frac{\partial E_x(\rho_i, z_j)}{\partial \rho} - \Delta z_{j-1} \frac{\partial^2 E_x(\rho_i, z_j)}{\partial \rho \partial z}$$

$$= \frac{\partial E_{x,\mathrm{C}}}{\partial \rho} - \Delta z_{j-1} \frac{\partial^2 E_{x,\mathrm{C}}}{\partial \rho \partial z} \tag{3.71}$$

$$\frac{\partial E_{x,\mathrm{S}}}{\partial z} = \frac{\partial E_{x,\mathrm{C}}}{\partial z} - \Delta z_{j-1} \frac{\partial^2 E_{x,\mathrm{C}}}{\partial z^2} \tag{3.72}$$

$$\frac{\partial^2 E_{x,\mathrm{S}}}{\partial \rho^2} = \frac{\partial^2 E_{x,\mathrm{C}}}{\partial \rho^2} \tag{3.73}$$

$$\frac{\partial^2 E_{x,\mathrm{S}}}{\partial \rho \partial z} = \frac{\partial^2 E_{x,\mathrm{C}}}{\partial \rho \partial z} \tag{3.74}$$

$$\frac{\partial^2 E_{x,\mathrm{S}}}{\partial z^2} = \frac{\partial^2 E_{x,\mathrm{C}}}{\partial z^2} \tag{3.75}$$

$$\frac{\partial E_{x,\mathrm{NE}}}{\partial \rho} = \frac{\partial E_x(\rho_{i+1}, z_{j+1})}{\partial \rho} = \frac{\partial E_x(\rho_i, z_j)}{\partial \rho} + \Delta\rho_{i+1}\frac{\partial^2 E_x(\rho_i, z_j)}{\partial \rho^2} + \Delta z_{j+1}\frac{\partial^2 E_x(\rho_i, z_j)}{\partial \rho \partial z}$$

$$= \frac{\partial E_{x,\mathrm{C}}}{\partial \rho} + \Delta\rho_{i+1}\frac{\partial^2 E_{x,\mathrm{C}}}{\partial \rho^2} + \Delta z_{j+1}\frac{\partial^2 E_{x,\mathrm{C}}}{\partial \rho \partial z} \tag{3.76}$$

$$\frac{\partial E_{x,\mathrm{NE}}}{\partial z} = \frac{\partial E_{x,\mathrm{C}}}{\partial z} + \Delta\rho_{i+1}\frac{\partial^2 E_{x,\mathrm{C}}}{\partial \rho \partial z} + \Delta z_{j+1}\frac{\partial^2 E_{x,\mathrm{C}}}{\partial z^2} \tag{3.77}$$

$$\frac{\partial^2 E_{x,\mathrm{NE}}}{\partial \rho^2} = \frac{\partial^2 E_{x,\mathrm{C}}}{\partial \rho^2} \tag{3.78}$$

$$\frac{\partial^2 E_{x,\mathrm{NE}}}{\partial \rho \partial z} = \frac{\partial^2 E_{x,\mathrm{C}}}{\partial \rho \partial z} \tag{3.79}$$

$$\frac{\partial^2 E_{x,\mathrm{NE}}}{\partial z^2} = \frac{\partial^2 E_{x,\mathrm{C}}}{\partial z^2} \tag{3.80}$$

$$\frac{\partial E_{x,\mathrm{SW}}}{\partial \rho} = \frac{\partial E_x(\rho_{i-1}, z_{j-1})}{\partial \rho} = \frac{\partial E_x(\rho_i, z_j)}{\partial \rho} - \Delta\rho_{i-1}\frac{\partial^2 E_x(\rho_i, z_j)}{\partial \rho^2} - \Delta z_{j-1}\frac{\partial^2 E_x(\rho_i, z_j)}{\partial \rho \partial z}$$

$$= \frac{\partial E_{x,\mathrm{C}}}{\partial \rho} - \Delta\rho_{i-1}\frac{\partial^2 E_{x,\mathrm{C}}}{\partial \rho^2} - \Delta z_{j-1}\frac{\partial^2 E_{x,\mathrm{C}}}{\partial \rho \partial z} \tag{3.81}$$

$$\frac{\partial E_{x,\mathrm{SW}}}{\partial z} = \frac{\partial E_{x,\mathrm{C}}}{\partial z} - \Delta\rho_{i-1}\frac{\partial^2 E_{x,\mathrm{C}}}{\partial \rho \partial z} - \Delta z_{j-1}\frac{\partial^2 E_{x,\mathrm{C}}}{\partial z^2} \tag{3.82}$$

$$\frac{\partial^2 E_{x,\mathrm{SW}}}{\partial \rho^2} = \frac{\partial^2 E_{x,\mathrm{C}}}{\partial \rho^2} \tag{3.83}$$

$$\frac{\partial^2 E_{x,\mathrm{SW}}}{\partial \rho \partial z} = \frac{\partial^2 E_{x,\mathrm{C}}}{\partial \rho \partial z} \tag{3.84}$$

$$\frac{\partial^2 E_{x,\mathrm{SW}}}{\partial z^2} = \frac{\partial^2 E_{x,\mathrm{C}}}{\partial z^2} \tag{3.85}$$

We may eventually condense (3.39)-(3.44) and (3.56)-(3.85) (for both E_ρ and E_z) into a matrix operator $\mathbf{T}_{i,j}$, as will be shown shortly. For the example provided in Figure 3.5 with fields $E_{\rho,\mathrm{N}}, E_{z,\mathrm{N}}$ and $E_{\rho,\mathrm{C}}, E_{z,\mathrm{C}}$ in distinct regions 1 and 2, Step 1 of the piecemeal Taylor series expansion would involve

$$\begin{bmatrix} E_x\big|_L \\ \frac{\partial E_x}{\partial \rho}\Big|_L \\ \frac{\partial E_x}{\partial z}\Big|_L \\ \frac{\partial^2 E_x}{\partial \rho^2}\Big|_L \\ \frac{\partial^2 E_x}{\partial \rho \partial z}\Big|_L \\ \frac{\partial^2 E_x}{\partial z^2}\Big|_L \end{bmatrix} = \begin{bmatrix} 1 & 0 & \Delta z_{j+1,L} & 0 & 0 & \frac{\Delta z_{j+1,L}^2}{2} \\ 0 & 1 & 0 & 0 & \Delta z_{j+1,L} & 0 \\ 0 & 0 & 1 & 0 & 0 & \Delta z_{j+1,L} \\ 0 & 0 & 0 & 1 & 0 & 0 \\ 0 & 0 & 0 & 0 & 1 & 0 \\ 0 & 0 & 0 & 0 & 0 & 1 \end{bmatrix} \begin{bmatrix} E_{x,\mathrm{C}} \\ \frac{\partial E_{x,\mathrm{C}}}{\partial \rho} \\ \frac{\partial E_{x,\mathrm{C}}}{\partial z} \\ \frac{\partial^2 E_{x,\mathrm{C}}}{\partial \rho^2} \\ \frac{\partial^2 E_{x,\mathrm{C}}}{\partial \rho \partial z} \\ \frac{\partial^2 E_{x,\mathrm{C}}}{\partial z^2} \end{bmatrix}$$

$$= \mathbf{T}_{i,j|L} \begin{bmatrix} E_{x,\mathrm{C}} \\ \frac{\partial E_{x,\mathrm{C}}}{\partial \rho} \\ \frac{\partial E_{x,\mathrm{C}}}{\partial z} \\ \frac{\partial^2 E_{x,\mathrm{C}}}{\partial \rho^2} \\ \frac{\partial^2 E_{x,\mathrm{C}}}{\partial \rho \partial z} \\ \frac{\partial^2 E_{x,\mathrm{C}}}{\partial z^2} \end{bmatrix} \tag{3.86}$$

while (3.39)-(3.40) and (3.42)-(3.44) continue to link $E_{\rho,\mathrm{C}}, E_{z,\mathrm{C}}$ to $E_{\rho,\mathrm{E}}, E_{z,\mathrm{E}}$, $E_{\rho,\mathrm{W}}, E_{z,\mathrm{W}}$, $E_{\rho,\mathrm{S}}, E_{z,\mathrm{S}}$, $E_{\rho,\mathrm{NE}}, E_{z,\mathrm{NE}}$, and $E_{\rho,\mathrm{SW}}, E_{z,\mathrm{SW}}$.

The rotation transformation from coordinates (ρ, z) to (n, t) for the interface's normal and tangential unit vectors, $\hat{n}$ and $\hat{t}$, is

$$n = \rho \cos\theta - z \sin\theta \tag{3.87}$$

$$t = \rho \sin\theta + z \cos\theta \tag{3.88}$$

belonging to SU(2) (in that it is a special unitary transformation applied to a vector in a cross-sectional coordinate system) and the operators

$$\frac{\partial}{\partial n} = \cos\theta \frac{\partial}{\partial \rho} - \sin\theta \frac{\partial}{\partial z} \tag{3.89}$$

$$\frac{\partial}{\partial t} = \sin\theta \frac{\partial}{\partial \rho} + \cos\theta \frac{\partial}{\partial z} \tag{3.90}$$

Field component and field component derivative expressions, as per the chain rule, are then

$$E_n = E_\rho \cos\theta - E_z \sin\theta \tag{3.91}$$

$$\frac{\partial E_n}{\partial n} = \cos^2\theta \frac{\partial E_\rho}{\partial \rho} - \frac{1}{2}\sin 2\theta \frac{\partial E_\rho}{\partial z} - \frac{1}{2}\sin 2\theta \frac{\partial E_z}{\partial \rho} + \sin^2\theta \frac{\partial E_z}{\partial z} \tag{3.92}$$

$$\frac{\partial E_n}{\partial t} = \frac{1}{2}\sin 2\theta \frac{\partial E_\rho}{\partial \rho} + \cos^2\theta \frac{\partial E_\rho}{\partial z} - \sin^2\theta \frac{\partial E_z}{\partial \rho} - \frac{1}{2}\sin 2\theta \frac{\partial E_z}{\partial z} \tag{3.93}$$

$$\begin{aligned}\frac{\partial^2 E_n}{\partial n^2} = \cos^3\theta \frac{\partial^2 E_\rho}{\partial \rho^2} - \sin 2\theta \cos\theta \frac{\partial^2 E_\rho}{\partial \rho \partial z} + \frac{1}{2}\sin\theta \sin 2\theta \frac{\partial^2 E_\rho}{\partial z^2} \\ -\frac{1}{2}\sin 2\theta \cos\theta \frac{\partial^2 E_z}{\partial \rho^2} + \sin\theta \sin 2\theta \frac{\partial^2 E_z}{\partial \rho \partial z} - \sin^3\theta \frac{\partial^2 E_z}{\partial z^2}\end{aligned} \tag{3.94}$$

$$\begin{aligned}\frac{\partial^2 E_n}{\partial n \partial t} = \frac{1}{2}\sin 2\theta \cos\theta \frac{\partial^2 E_\rho}{\partial \rho^2} + \cos\theta \cos 2\theta \frac{\partial^2 E_\rho}{\partial \rho \partial z} - \frac{1}{2}\sin 2\theta \cos\theta \frac{\partial^2 E_\rho}{\partial z^2} \\ -\frac{1}{2}\sin\theta \sin 2\theta \frac{\partial^2 E_z}{\partial \rho^2} - \sin\theta \cos 2\theta \frac{\partial^2 E_z}{\partial \rho \partial z} + \frac{1}{2}\sin\theta \sin 2\theta \frac{\partial^2 E_z}{\partial z^2}\end{aligned} \tag{3.95}$$

$$\begin{aligned}\frac{\partial^2 E_n}{\partial t^2} = \frac{1}{2}\sin\theta \sin 2\theta \frac{\partial^2 E_\rho}{\partial \rho^2} + \sin 2\theta \cos\theta \frac{\partial^2 E_\rho}{\partial \rho \partial z} + \cos^3\theta \frac{\partial^2 E_\rho}{\partial z^2} \\ -\sin^3\theta \frac{\partial^2 E_z}{\partial \rho^2} - \sin\theta \sin 2\theta \frac{\partial^2 E_z}{\partial \rho \partial z} - \frac{1}{2}\sin 2\theta \cos\theta \frac{\partial^2 E_z}{\partial z^2}\end{aligned} \tag{3.96}$$

$$E_t = E_\rho \sin\theta + E_z \cos\theta \tag{3.97}$$

$$\frac{\partial E_t}{\partial n} = \frac{1}{2}\sin 2\theta \frac{\partial E_\rho}{\partial \rho} - \sin^2\theta \frac{\partial E_\rho}{\partial z} + \cos^2\theta \frac{\partial E_z}{\partial \rho} - \frac{1}{2}\sin 2\theta \frac{\partial E_z}{\partial z} \tag{3.98}$$

$$\frac{\partial E_t}{\partial t} = \sin^2\theta \frac{\partial E_\rho}{\partial \rho} + \frac{1}{2}\sin 2\theta \frac{\partial E_\rho}{\partial z} + \frac{1}{2}\sin 2\theta \frac{\partial E_z}{\partial \rho} + \cos^2\theta \frac{\partial E_z}{\partial z} \tag{3.99}$$

$$\begin{aligned}\frac{\partial^2 E_t}{\partial n^2} = \frac{1}{2}\sin 2\theta \cos\theta \frac{\partial^2 E_\rho}{\partial \rho^2} - \sin\theta \sin 2\theta \frac{\partial^2 E_\rho}{\partial \rho \partial z} + \sin^3\theta \frac{\partial^2 E_\rho}{\partial z^2} \\ +\cos^3\theta \frac{\partial^2 E_z}{\partial \rho^2} - \sin 2\theta \cos\theta \frac{\partial^2 E_z}{\partial \rho \partial z} + \frac{1}{2}\sin\theta \sin 2\theta \frac{\partial^2 E_z}{\partial z^2}\end{aligned} \tag{3.100}$$

$$\begin{aligned}\frac{\partial^2 E_t}{\partial n \partial t} = \frac{1}{2}\sin\theta \sin 2\theta \frac{\partial^2 E_\rho}{\partial \rho^2} + \sin\theta \cos 2\theta \frac{\partial^2 E_\rho}{\partial \rho \partial z} - \frac{1}{2}\sin\theta \sin 2\theta \frac{\partial^2 E_\rho}{\partial z^2} \\ +\frac{1}{2}\sin 2\theta \cos\theta \frac{\partial^2 E_z}{\partial \rho^2} + \cos\theta \cos 2\theta \frac{\partial^2 E_z}{\partial \rho \partial z} - \frac{1}{2}\sin 2\theta \cos\theta \frac{\partial^2 E_z}{\partial z^2}\end{aligned} \tag{3.101}$$

$$\begin{aligned}\frac{\partial^2 E_t}{\partial t^2} = \sin^3\theta \frac{\partial^2 E_\rho}{\partial \rho^2} + \sin\theta \sin 2\theta \frac{\partial^2 E_\rho}{\partial \rho \partial z} + \frac{1}{2}\sin 2\theta \cos\theta \frac{\partial^2 E_\rho}{\partial z^2} \\ +\frac{1}{2}\sin\theta \sin 2\theta \frac{\partial^2 E_z}{\partial \rho^2} + \sin 2\theta \cos\theta \frac{\partial^2 E_z}{\partial \rho \partial z} + \cos^3\theta \frac{\partial^2 E_z}{\partial z^2}\end{aligned} \tag{3.102}$$

At this point, we have an opportunity to clarify the elements of $\mathbf{R}_{i,j}(\theta)$. Taking $f(\theta) = \sin\theta$, $g(\theta) = \cos\theta$, and θ to refer to the particular angle of the (i,j) stencil:

$$
\begin{bmatrix} E_n \\ \frac{\partial E_n}{\partial n} \\ \frac{\partial E_n}{\partial t} \\ \frac{\partial^2 E_n}{\partial n^2} \\ \frac{\partial^2 E_n}{\partial n \partial t} \\ \frac{\partial^2 E_n}{\partial t^2} \\ E_t \\ \frac{\partial E_t}{\partial n} \\ \frac{\partial E_t}{\partial t} \\ \frac{\partial^2 E_t}{\partial n^2} \\ \frac{\partial^2 E_t}{\partial n \partial t} \\ \frac{\partial^2 E_t}{\partial t^2} \end{bmatrix} = \begin{bmatrix} g(\theta) & 0 & 0 & 0 & 0 & 0 \\ 0 & g^2(\theta) & -\frac{f(2\theta)}{2} & 0 & 0 & 0 \\ 0 & \frac{f(2\theta)}{2} & g^2(\theta) & 0 & 0 & 0 \\ 0 & 0 & 0 & g^3(\theta) & -f(2\theta)g(\theta) & \frac{f(\theta)f(2\theta)}{2} \\ 0 & 0 & 0 & \frac{f(2\theta)g(\theta)}{2} & g(\theta)g(2\theta) & -\frac{f(2\theta)g(\theta)}{2} \\ 0 & 0 & 0 & \frac{f(\theta)f(2\theta)}{2} & f(2\theta)g(\theta) & g^3(\theta) \\ f(\theta) & 0 & 0 & 0 & 0 & 0 \\ 0 & \frac{f(2\theta)}{2} & -f^2(\theta) & 0 & 0 & 0 \\ 0 & f^2(\theta) & \frac{f(2\theta)}{2} & 0 & 0 & 0 \\ 0 & 0 & 0 & \frac{f(2\theta)g(\theta)}{2} & -f(\theta)f(2\theta) & f^3(\theta) \\ 0 & 0 & 0 & \frac{f(\theta)f(2\theta)}{2} & f(\theta)g(2\theta) & -\frac{f(\theta)f(2\theta)}{2} \\ 0 & 0 & 0 & f^3(\theta) & f(\theta)f(2\theta) & \frac{f(2\theta)g(\theta)}{2} \end{bmatrix}
$$

$$
\begin{bmatrix} -f(\theta) & 0 & 0 & 0 & 0 & 0 \\ 0 & -\frac{f(2\theta)}{2} & f^2(\theta) & 0 & 0 & 0 \\ 0 & -f^2(\theta) & -\frac{f(2\theta)}{2} & 0 & 0 & 0 \\ 0 & 0 & 0 & -\frac{f(2\theta)g(\theta)}{2} & f(\theta)f(2\theta) & -f^3(\theta) \\ 0 & 0 & 0 & -\frac{f(\theta)f(2\theta)}{2} & -f(\theta)g(2\theta) & \frac{f(\theta)f(2\theta)}{2} \\ 0 & 0 & 0 & -f^3(\theta) & -f(\theta)f(2\theta) & -\frac{f(2\theta)g(\theta)}{2} \\ g(\theta) & 0 & 0 & 0 & 0 & 0 \\ 0 & g^2(\theta) & -\frac{f(2\theta)}{2} & 0 & 0 & 0 \\ 0 & \frac{f(2\theta)}{2} & g^2(\theta) & 0 & 0 & 0 \\ 0 & 0 & 0 & g^3(\theta) & -f(2\theta)g(\theta) & \frac{f(\theta)f(2\theta)}{2} \\ 0 & 0 & 0 & \frac{f(2\theta)g(\theta)}{2} & g(\theta)g(2\theta) & -\frac{f(2\theta)g(\theta)}{2} \\ 0 & 0 & 0 & \frac{f(\theta)f(2\theta)}{2} & f(2\theta)g(\theta) & g^3(\theta) \end{bmatrix} \begin{bmatrix} E_\rho \\ \frac{\partial E_\rho}{\partial \rho} \\ \frac{\partial E_\rho}{\partial z} \\ \frac{\partial^2 E_\rho}{\partial \rho^2} \\ \frac{\partial^2 E_\rho}{\partial \rho \partial z} \\ \frac{\partial^2 E_\rho}{\partial z^2} \\ E_z \\ \frac{\partial E_z}{\partial \rho} \\ \frac{\partial E_z}{\partial z} \\ \frac{\partial^2 E_z}{\partial \rho^2} \\ \frac{\partial^2 E_z}{\partial \rho \partial z} \\ \frac{\partial^2 E_z}{\partial z^2} \end{bmatrix}
$$

$$
= \mathbf{R}_{i,j}(\theta) \begin{bmatrix} E_\rho \\ \frac{\partial E_\rho}{\partial \rho} \\ \frac{\partial E_\rho}{\partial z} \\ \frac{\partial^2 E_\rho}{\partial \rho^2} \\ \frac{\partial^2 E_\rho}{\partial \rho \partial z} \\ \frac{\partial^2 E_\rho}{\partial z^2} \\ E_z \\ \frac{\partial E_z}{\partial \rho} \\ \frac{\partial E_z}{\partial z} \\ \frac{\partial^2 E_z}{\partial \rho^2} \\ \frac{\partial^2 E_z}{\partial \rho \partial z} \\ \frac{\partial^2 E_z}{\partial z^2} \end{bmatrix} \quad (3.103)
$$

The essence of this thesis's full-vector finite difference mode solver lies in the judicious use of the interface continuity relations. Since the local rotation transformation guarantees the field components will be either parallel or perpendicular to the interface, the first and second-order derivative variants can be deduced based on Maxwell's equations, the Helmholtz equation, and the ϵ continuity in the t-direction. Trivially, we rephrase (3.22) and (3.24) as

$$E_n|_R = \frac{\epsilon_L}{\epsilon_R}\, E_n|_L \tag{3.104}$$

$$E_t|_R = E_t|_L \tag{3.105}$$

while azimuthal symmetry, i.e. $E_\phi|_R = E_\phi|_L$ and $H_\phi|_R = H_\phi|_L$, helps us elucidate that

$$\left.\frac{\partial E_n}{\partial n}\right|_R = \left.\frac{\partial E_n}{\partial n}\right|_L \tag{3.106}$$

$$\left.\frac{\partial E_n}{\partial t}\right|_R = \frac{\epsilon_L}{\epsilon_R}\left.\frac{\partial E_n}{\partial t}\right|_L \tag{3.107}$$

$$\left.\frac{\partial^2 E_n}{\partial n^2}\right|_R = \frac{\epsilon_L}{\epsilon_R}\left.\frac{\partial^2 E_n}{\partial n^2}\right|_L + k_o^2\frac{\epsilon_L(\epsilon_L-\epsilon_R)}{\epsilon_R}\, E_n|_L \tag{3.108}$$

$$\left.\frac{\partial^2 E_n}{\partial n \partial t}\right|_R = \left.\frac{\partial^2 E_n}{\partial n \partial t}\right|_L \tag{3.109}$$

$$\left.\frac{\partial^2 E_n}{\partial t^2}\right|_R = \frac{\epsilon_L}{\epsilon_R}\left.\frac{\partial^2 E_n}{\partial t^2}\right|_L \tag{3.110}$$

$$\left.\frac{\partial E_t}{\partial n}\right|_R = \left.\frac{\partial E_t}{\partial n}\right|_L + \left(\frac{\epsilon_L}{\epsilon_R}-1\right)\left.\frac{\partial E_n}{\partial t}\right|_L \tag{3.111}$$

$$\left.\frac{\partial E_t}{\partial t}\right|_R = \left.\frac{\partial E_t}{\partial t}\right|_L \tag{3.112}$$

$$\left.\frac{\partial^2 E_t}{\partial n^2}\right|_R = \left.\frac{\partial^2 E_t}{\partial n^2}\right|_L + k_o^2(\epsilon_L-\epsilon_R)\, E_t|_L \tag{3.113}$$

$$\left.\frac{\partial^2 E_t}{\partial n \partial t}\right|_R = \left.\frac{\partial^2 E_t}{\partial n \partial t}\right|_L + \left(\frac{\epsilon_L}{\epsilon_R} - 1\right) \left.\frac{\partial^2 E_n}{\partial t^2}\right|_L \tag{3.114}$$

$$\left.\frac{\partial^2 E_t}{\partial t^2}\right|_R = \left.\frac{\partial^2 E_t}{\partial t^2}\right|_L \tag{3.115}$$

where ϵ_R and ϵ_L are relative permittivities (vide Appendix A). Ergo, the interface continuity relation matrix $\mathbf{C}_{i,j}$ acting as central operator in a larger product arises:

$$\begin{bmatrix} E_n|_R \\ \frac{\partial E_n}{\partial n}\big|_R \\ \frac{\partial E_n}{\partial t}\big|_R \\ \frac{\partial^2 E_n}{\partial n^2}\big|_R \\ \frac{\partial^2 E_n}{\partial n \partial t}\big|_R \\ \frac{\partial^2 E_n}{\partial t^2}\big|_R \\ E_t|_R \\ \frac{\partial E_t}{\partial n}\big|_R \\ \frac{\partial E_t}{\partial t}\big|_R \\ \frac{\partial^2 E_t}{\partial n^2}\big|_R \\ \frac{\partial^2 E_t}{\partial n \partial t}\big|_R \\ \frac{\partial^2 E_t}{\partial t^2}\big|_R \end{bmatrix} = \begin{bmatrix} \frac{\epsilon_{i,j}}{\epsilon_{i,j+1}} & 0 & 0 & 0 & 0 & 0 \\ 0 & 1 & 0 & 0 & 0 & 0 \\ 0 & 0 & \frac{\epsilon_{i,j}}{\epsilon_{i,j+1}} & 0 & 0 & 0 \\ k_o^2 \frac{\epsilon_{i,j}(\epsilon_{i,j} - \epsilon_{i,j+1})}{\epsilon_{i,j+1}} & 0 & 0 & \frac{\epsilon_{i,j}}{\epsilon_{i,j+1}} & 0 & 0 \\ 0 & 0 & 0 & 0 & 1 & 0 \\ 0 & 0 & 0 & 0 & 0 & \frac{\epsilon_{i,j}}{\epsilon_{i,j+1}} \\ 0 & 0 & 0 & 0 & 0 & 0 \\ 0 & 0 & \left(\frac{\epsilon_{i,j}}{\epsilon_{i,j+1}} - 1\right) & 0 & 0 & 0 \\ 0 & 0 & 0 & 0 & 0 & 0 \\ 0 & 0 & 0 & 0 & 0 & 0 \\ 0 & 0 & 0 & 0 & 0 & \left(\frac{\epsilon_{i,j}}{\epsilon_{i,j+1}} - 1\right) \\ 0 & 0 & 0 & 0 & 0 & 0 \end{bmatrix}$$

$$\begin{bmatrix} 0 & 0 & 0 & 0 & 0 & 0 \\ 0 & 0 & 0 & 0 & 0 & 0 \\ 0 & 0 & 0 & 0 & 0 & 0 \\ 0 & 0 & 0 & 0 & 0 & 0 \\ 0 & 0 & 0 & 0 & 0 & 0 \\ 0 & 0 & 0 & 0 & 0 & 0 \\ 1 & 0 & 0 & 0 & 0 & 0 \\ 0 & 1 & 0 & 0 & 0 & 0 \\ 0 & 0 & 1 & 0 & 0 & 0 \\ k_o^2(\epsilon_{i,j} - \epsilon_{i,j+1}) & 0 & 0 & 1 & 0 & 0 \\ 0 & 0 & 0 & 0 & 1 & 0 \\ 0 & 0 & 0 & 0 & 0 & 1 \end{bmatrix} \begin{bmatrix} E_n|_L \\ \frac{\partial E_n}{\partial n}\big|_L \\ \frac{\partial E_n}{\partial t}\big|_L \\ \frac{\partial^2 E_n}{\partial n^2}\big|_L \\ \frac{\partial^2 E_n}{\partial n \partial t}\big|_L \\ \frac{\partial^2 E_n}{\partial t^2}\big|_L \\ E_t|_L \\ \frac{\partial E_t}{\partial n}\big|_L \\ \frac{\partial E_t}{\partial t}\big|_L \\ \frac{\partial^2 E_t}{\partial n^2}\big|_L \\ \frac{\partial^2 E_t}{\partial n \partial t}\big|_L \\ \frac{\partial^2 E_t}{\partial t^2}\big|_L \end{bmatrix}$$

$$= \mathbf{C}_{i,j} \begin{bmatrix} E_n|_L \\ \frac{\partial E_n}{\partial n}\Big|_L \\ \frac{\partial E_n}{\partial t}\Big|_L \\ \frac{\partial^2 E_n}{\partial n^2}\Big|_L \\ \frac{\partial^2 E_n}{\partial n \partial t}\Big|_L \\ \frac{\partial^2 E_n}{\partial t^2}\Big|_L \\ E_t|_L \\ \frac{\partial E_t}{\partial n}\Big|_L \\ \frac{\partial E_t}{\partial t}\Big|_L \\ \frac{\partial^2 E_t}{\partial n^2}\Big|_L \\ \frac{\partial^2 E_t}{\partial n \partial t}\Big|_L \\ \frac{\partial^2 E_t}{\partial t^2}\Big|_L \end{bmatrix} \quad (3.116)$$

in keeping with Figure 3.5. Such a matrix, in combination with those outlined before it, must be multiplied by one another in a strict order. This product that we name $\mathbf{S}^{\mathrm{N}}_{i,j}$ constitutes

$$\begin{bmatrix} E_{\rho,\mathrm{N}} \\ 0 \\ 0 \\ 0 \\ 0 \\ 0 \\ E_{z,\mathrm{N}} \\ 0 \\ 0 \\ 0 \\ 0 \\ 0 \end{bmatrix} = \begin{bmatrix} \mathbf{T}_{i,j|R} & \mathbf{0}_{6,6} \\ \mathbf{0}_{6,6} & \mathbf{T}_{i,j|R} \end{bmatrix} \mathbf{R}_{i,j}(\theta)\mathbf{C}_{i,j}\mathbf{R}_{i,j}(-\theta) \begin{bmatrix} \mathbf{T}_{i,j|L} & \mathbf{0}_{6,6} \\ \mathbf{0}_{6,6} & \mathbf{T}_{i,j|L} \end{bmatrix} \begin{bmatrix} E_{\rho,\mathrm{C}} \\ \frac{\partial E_{\rho,\mathrm{C}}}{\partial \rho} \\ \frac{\partial E_{\rho,\mathrm{C}}}{\partial z} \\ \frac{\partial^2 E_{\rho,\mathrm{C}}}{\partial \rho^2} \\ \frac{\partial^2 E_{\rho,\mathrm{C}}}{\partial \rho \partial z} \\ \frac{\partial^2 E_{\rho,\mathrm{C}}}{\partial z^2} \\ E_{z,\mathrm{C}} \\ \frac{\partial E_{z,\mathrm{C}}}{\partial \rho} \\ \frac{\partial E_{z,\mathrm{C}}}{\partial z} \\ \frac{\partial^2 E_{z,\mathrm{C}}}{\partial \rho^2} \\ \frac{\partial^2 E_{z,\mathrm{C}}}{\partial \rho \partial z} \\ \frac{\partial^2 E_{z,\mathrm{C}}}{\partial z^2} \end{bmatrix}$$

$$= \mathbf{S}^{\mathrm{N}}_{i,j} \begin{bmatrix} E_{\rho,\mathrm{C}} \\ \frac{\partial E_{\rho,\mathrm{C}}}{\partial \rho} \\ \frac{\partial E_{\rho,\mathrm{C}}}{\partial z} \\ \frac{\partial^2 E_{\rho,\mathrm{C}}}{\partial \rho^2} \\ \frac{\partial^2 E_{\rho,\mathrm{C}}}{\partial \rho \partial z} \\ \frac{\partial^2 E_{\rho,\mathrm{C}}}{\partial z^2} \\ E_{z,\mathrm{C}} \\ \frac{\partial E_{z,\mathrm{C}}}{\partial \rho} \\ \frac{\partial E_{z,\mathrm{C}}}{\partial z} \\ \frac{\partial^2 E_{z,\mathrm{C}}}{\partial \rho^2} \\ \frac{\partial^2 E_{z,\mathrm{C}}}{\partial \rho \partial z} \\ \frac{\partial^2 E_{z,\mathrm{C}}}{\partial z^2} \end{bmatrix} \tag{3.117}$$

After similarly amassing $\mathbf{S}^{\mathrm{NE}}_{i,j}$, $\mathbf{S}^{\mathrm{E}}_{i,j}$, $\mathbf{S}^{\mathrm{S}}_{i,j}$, $\mathbf{S}^{\mathrm{SW}}_{i,j}$, and $\mathbf{S}^{\mathrm{W}}_{i,j}$ it is then possible to construct an $\mathbf{S}_{i,j}$ of greater size and invert it into a $\mathbf{M}_{i,j}$. Once again, $\mathbf{M}_{i,j}$ will compose the finite difference matrix $\mathbf{V}$ used to solve for the eigenmodes and eigenfrequencies:

$$\mathbf{V}\ \mathbf{E} = \mathbf{V} \begin{bmatrix} E_\rho|_{(1,1)} \\ \vdots \\ E_\rho|_{(M,N)} \\ E_z|_{(1,1)} \\ \vdots \\ E_z|_{(M,N)} \end{bmatrix} = -k_o^2 \begin{bmatrix} E_\rho|_{(1,1)} \\ \vdots \\ E_\rho|_{(M,N)} \\ E_z|_{(1,1)} \\ \vdots \\ E_z|_{(M,N)} \end{bmatrix} \tag{3.118}$$

Chapter 4

Numerical Simulations

4.1 Bare Microcavity

A good starting point for model verification is the assessment of ordinary WGM microresonators. Microspheres, for instance, have analytical WGM's as was previously mentioned in Chapter 2. Figure 4.1 exemplifies the extent of convergence of the computed eigenwavelengths for a glass microsphere submerged in water (referred in Subsection 3.1.2, with a radius of 30 μm and $m = 340$) towards an analytical value [14], all the specifics of which will later be expounded. There is inherent value in also comparing the full-vector mode solver's numerical eigenmodes to theoretical field distributions, yet the exclusive advantages of the solver are somewhat shrouded. There is leakage into the cladding region analogous to the exponential decaying wavefunction beyond potential barriers in the quantum mechanical model of a particle in a finite spherical potential well, where the field is represented by a different product of a coefficient and special functions inside and outside the sphere. A superior candidate for simulation is instead the increasingly complex surface of revolution that is the microtoroid, as it evades analytical treatment and stands as a practical platform for experiment.

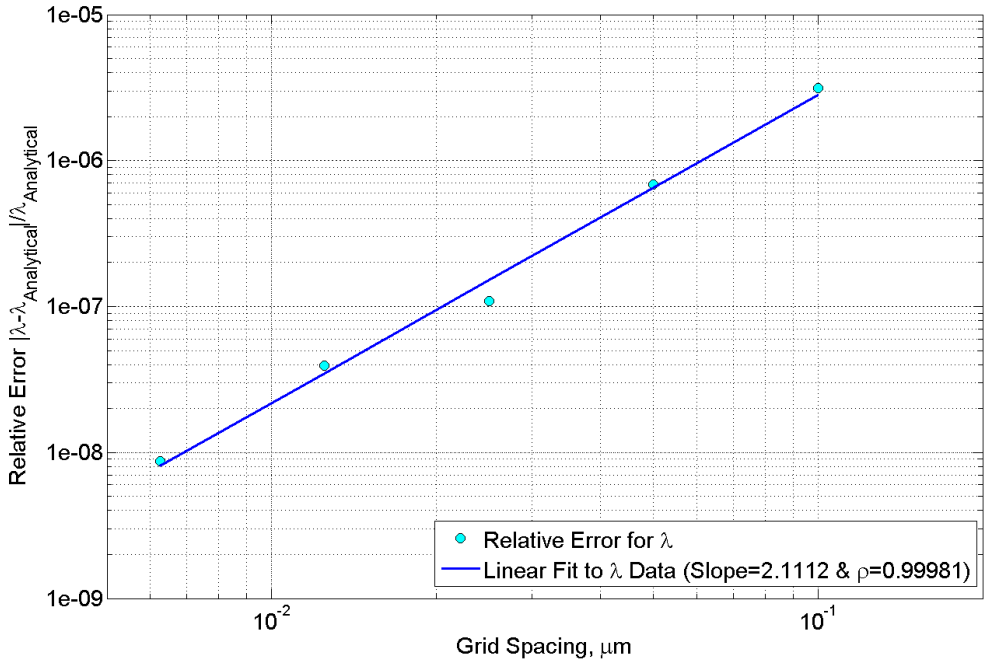

Figure 4.1: Trend of the resonant wavelength's relative error for the 340$^{\text{th}}$ fundamental transverse electric-like WGM in a microspherical cavity as uniform grid spacings are continuously halved. An analytically calculated $\lambda_{\text{Res}} = 780.911$ nm serves as a reference.

Figure 4.2 illustrates a plain SiO_2 toroidal cavity. The high degree of radial and azimuthal confinement [63, 87] is dictated by the resonator's aspect ratio, equivalent to the principal/major radius R divided by the minor radius r. By superimposing a uniform grid onto a ρ-z cross-section, a point-by-point refractive index map and computation domain can be circumscribed. From this data, the operational wavelength, and an awareness of the exact locations of the interfaces within the structure, eigenvector and eigenvalue pairs can be retrieved. For ease of reference and the sake of consistency, the following sections of this thesis will contain tabular entries of the simulation input parameters in an unchanging format.

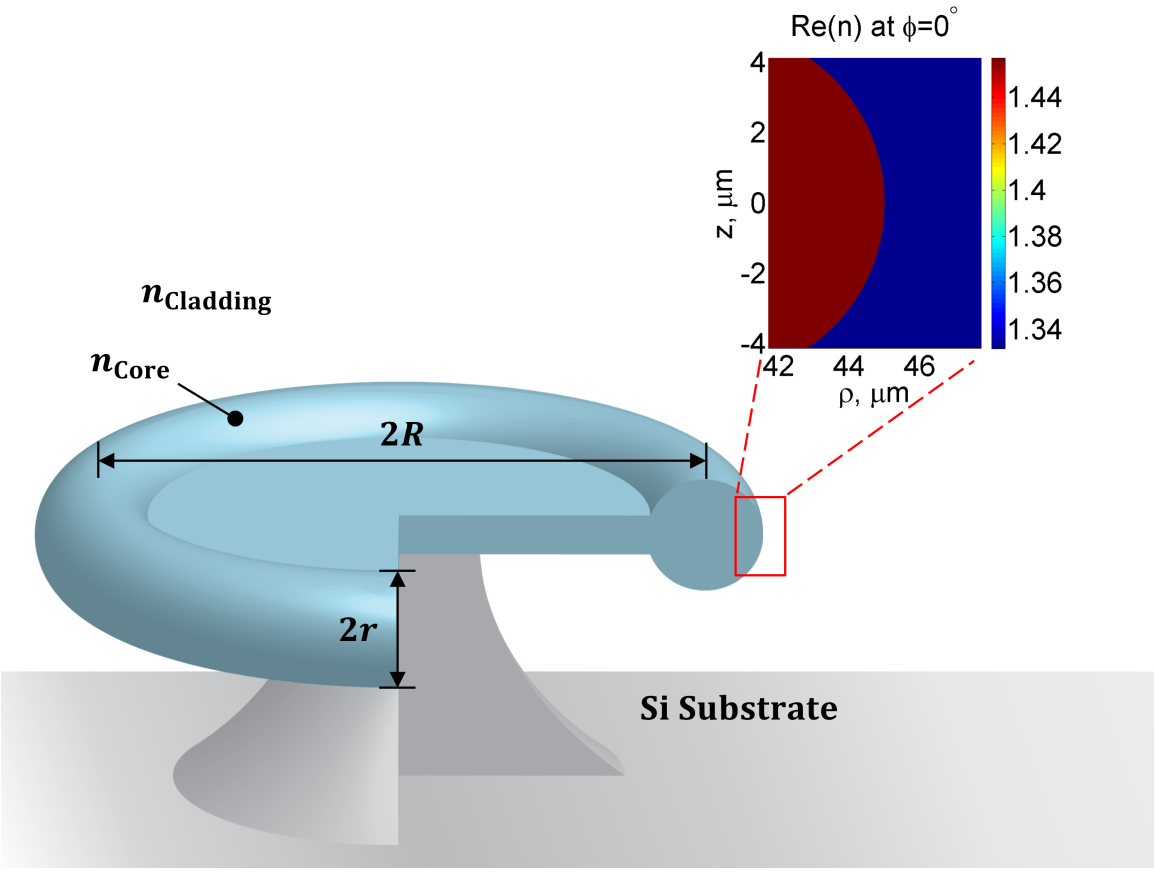

Figure 4.2: Cross-sectional diagram of a silica microtoroid enclosed by liquid water accompanied by the refractive index profile for $\lambda = 633$ nm.

Helium-neon gas lasers commonly operate in the red within the visible spectrum, due to their high-gain 632.8 nm line. By pairing an approximated free-space wavelength with the corresponding properties in Table 4.1, optical WGM resonances with their own nearby wavelengths and physical m's on the order of 100 can be isolated for. Using ARPACK subroutines [88], written to solve for the eigenvectors and eigenvalues of matrices using either the Implicitly Restarted Arnoldi or Lanczos Method (IRAM or IRLM), we may search for a number of eigenvectors with eigenvalues of largest real part for a sparse matrix $\mathbf{V}$. It is also important to recognize that in the transition from a microsphere's effective potential to that of a microtoroid, from a theoretical viewpoint, the radial eigenfunctions remain relatively unperturbed while the polar eigenfunctions suffer observable spatial narrowing.

Finite Difference Grid	
Uniform Grid Spacings	$\Delta\rho = \Delta z = 100$, 50, 25, 12.5, & 6.25 nm
Excitation Source	
Operational Wavelength	$\lambda = 633$ nm
Geometry	
Major Radius	$R = 40$ μm
Minor Radius	$r = 5$ μm
Aspect Ratio	$\frac{R}{r} = 8$
Materials	
Core/Microcavity: SiO_2	$n_{\text{Core}} = 1.457 + i(6.95 \times 10^{-11})$
Cladding/External Dielectric: H_2O	$n_{\text{Cladding}} = 1.332 + i(1.47 \times 10^{-8})$
Resonance	
Azimuthal Mode Order	$m = 636$

Table 4.1: WGM simulation parameters for a bare microtoroid.

Forcing $\widetilde{m} = m$ via $m_i = 0$ consequently encodes loss information onto the resonant wavelength such that it becomes

$$\widetilde{\lambda}_{\text{Res}} = \lambda_{\text{Res}} + i\lambda_{\text{Res},i} \tag{4.1}$$

As in Chapter 2, the Q-factor communicates field attenuation on per cycle basis. A preliminary calculation, given the existence of an absorption index κ and complex $\widetilde{\lambda}_{\text{Res}}$, is [89]

$$\begin{aligned} Q &= \frac{\text{Re}(\widetilde{\lambda}_{\text{Res}})}{2\text{Im}(\widetilde{\lambda}_{\text{Res}})} \\ &= \frac{\lambda_{\text{Res}}}{2\lambda_{\text{Res},i}} \end{aligned} \tag{4.2}$$

rather than the expression for an uninhibited $\widetilde{m}$, which is otherwise

$$\begin{aligned} Q &= \frac{\mathrm{Re}(\widetilde{m})}{2\mathrm{Im}(\widetilde{m})} \\ &= \frac{m}{2m_i} \end{aligned} \tag{4.3}$$

Opting for an $R > 15$ μm allows for absorption that dominates over radiation leakage [90], circumventing the PML that would normally be needed for lower radii of curvature of the cavity. The quasi-transverse electric (TE) and quasi-transverse magnetic (TM) mode profiles of Figures 4.3 and 4.4 for the water-immersed silica microtoroid ($R = 40$ μm and $r = 5$ μm) at $\Delta\rho = \Delta z = 6.25$ nm are a strong indication of the mode solver output's correctness. As for the transverse field components' behaviour across the interface at $z = 0$, we see that the value of $\mathrm{Re}(E_z)$ does not vary while $\mathrm{Re}(E_\rho)$ changes discontinuously according to

$$\begin{aligned} \mathrm{Re}(E_{\rho,\mathrm{Cladding}}) &= \mathrm{Re}\left(\frac{n^2_{\mathrm{Core}}}{n^2_{\mathrm{Cladding}}} E_{\rho,\mathrm{Core}}\right) \\ &= \mathrm{Re}\left(\frac{n^2_{\mathrm{Core}}}{n^2_{\mathrm{Cladding}}}\right) \mathrm{Re}(E_{\rho,\mathrm{Core}}) \\ &= 1.197\mathrm{Re}(E_{\rho,\mathrm{Core}}) \end{aligned} \tag{4.4}$$

as in Figure 4.5. The real part of the longitudinal component, $\mathrm{Re}(E_\phi)$, is expectedly continuous everywhere within the computation window. Even though continuity in this distribution is no longer prevalent once axisymmetry is broken, the cross-sectional mode profiles can be manipulated and aggregated (e.g. via mode matching) to put the asymmetry into account. Aspects of propagation, in this regard, will be briefly addressed in Chapter 5.

Comparing the fundamental quasi-TE mode's $\lambda_{\mathrm{Res}} = 632.756$ nm and $Q = 1.64 \times 10^9$ for dissipative surroundings and $\Delta\rho = \Delta z = 6.25$ nm to like data for a COMSOL Multiphysics FE solver, specifically 632.747 nm and 1.65×10^9 [17], we procure respective relative errors of 1.42×10^{-5} and 6.06×10^{-3}. Note here that this thesis's full-vector finite difference mode solving technique arrives at such a solution in one of two ways:

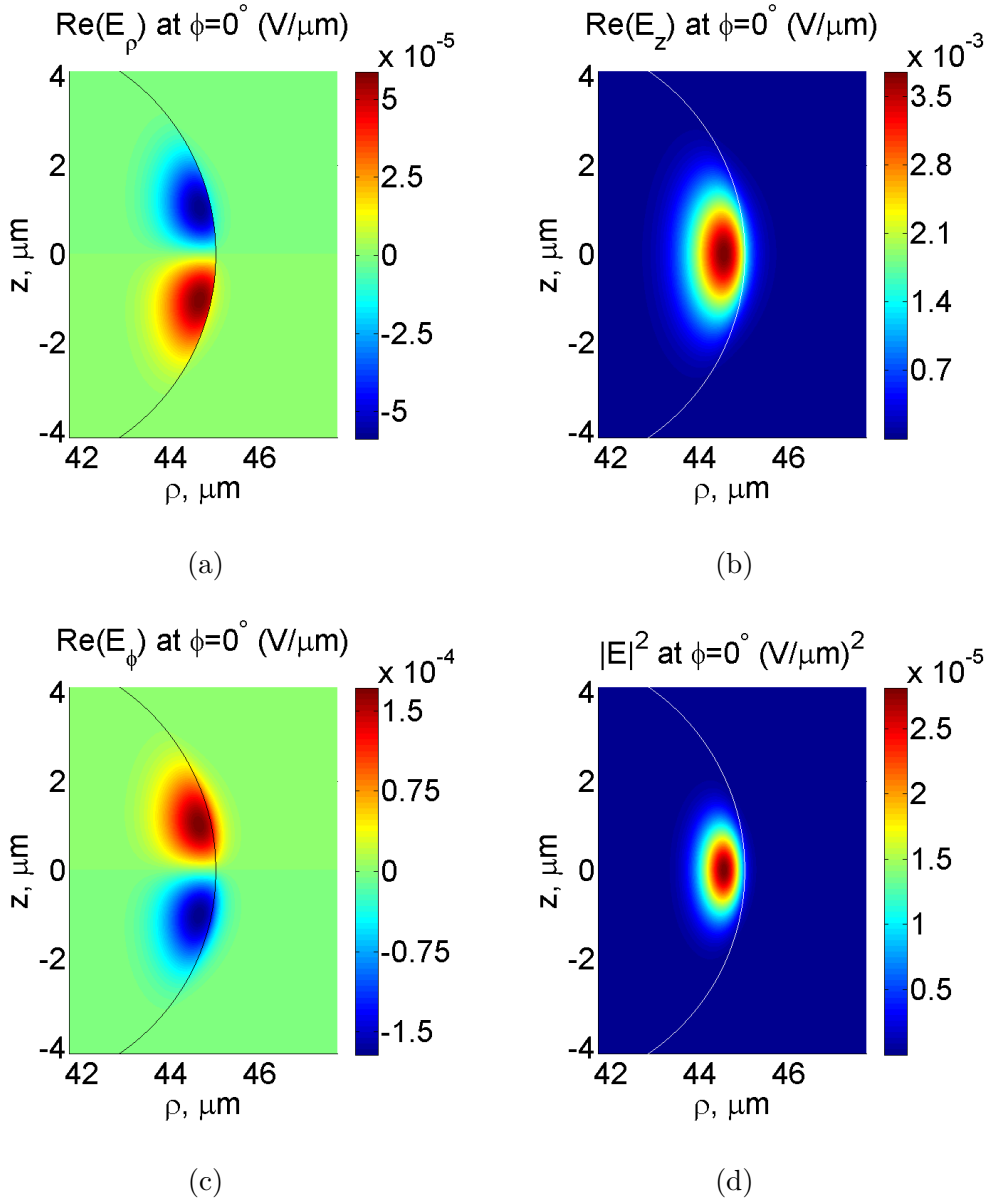

Figure 4.3: Fundamental quasi-TE mode for a silica microtoroid surrounded by water, where $m = 636$, $\lambda_{\text{Res}} = 632.756$ nm, and $Q = 1.64 \times 10^9$. (a), (b), and (c) are respectively the real parts of the ρ, z, and ϕ-directed electric field components E_ρ, E_z, and E_ϕ, whilst (d) is the modulus of the total electric field squared $|\vec{E}|^2$.

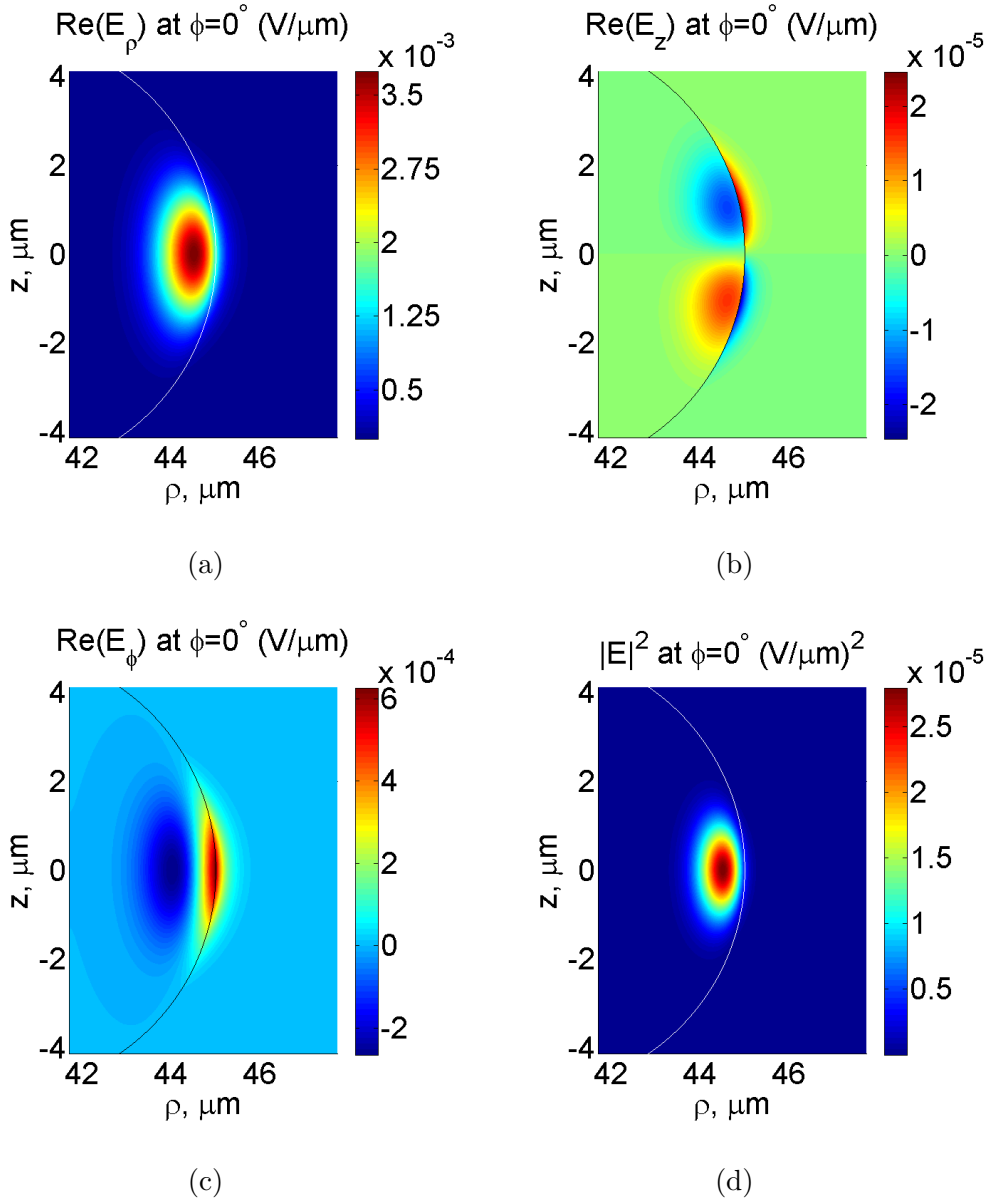

Figure 4.4: Fundamental quasi-TM mode for a silica microtoroid surrounded by water, where $m = 636$, $\lambda_{\text{Res}} = 632.399$ nm, and $Q = 1.45 \times 10^9$. (a), (b), and (c) are respectively the real parts of the ρ, z, and ϕ-directed electric field components E_ρ, E_z, and E_ϕ, whilst (d) is the modulus of the total electric field squared $|\vec{E}|^2$.

1. Solver iterations based on the value of $|\lambda_{\text{Res,Next}} - \lambda_{\text{Res,Previous}}|/\lambda_{\text{Res,Next}}$ due to the $\mathbf{V}(\widetilde{\lambda}_{\text{Res}})$ dependency. If this error is smaller than 1×10^{-6}, convergence is considered to have occurred.

2. 2D matrix determinant minimization of $\det(\mathbf{V} + k_o^2\mathbf{I})$ with respect to $\widetilde{\lambda}_{\text{Res}}$ in the complex plane for the recast $(\mathbf{V} + k_o^2\mathbf{I})\mathbf{E} = \mathbf{0}$, where $\mathbf{I}$ is an identity matrix with the same dimensions as $\mathbf{V}$ and $\mathbf{0}$ is a zero column vector with the same number of rows as $\mathbf{E}$.

In most cases, solver iterations are favoured over 2D matrix determinant optimization. The latter has a longer computation time stemming from multiple, mandatory LUP

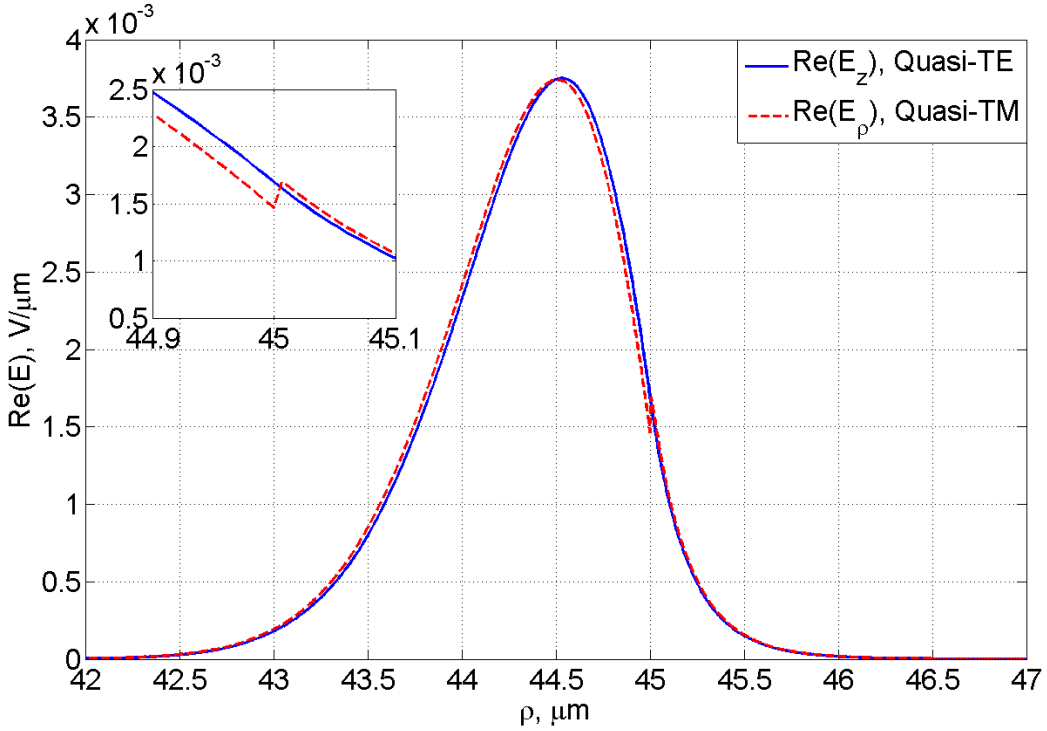

Figure 4.5: Real parts of the major electric fields for the 636$^{\text{th}}$ fundamental quasi-TE and quasi-TM modes of the bare microtoroid. The profiles correspond to the $z = 0$ line intersecting the silica-water interface, wherein the inset exposes the discontinuous $\text{Re}(E_\rho)$ at the $\rho = 45$ μm permittivity transition.

decompositions towards computing matrix determinants (detailed in Appendix B). A single solver iteration with $\sim 3 \times 10^5$ nodes and a uniform grid spacing of 12.5 nm, for example, occupies 57 seconds of time and 3.4 GB of memory on a computer with a 2.30 GHz base processor frequency and 16.0 GB of random-access memory. As little as one iteration is required for this particular arrangement as the relative error for the fundamental quasi-TE mode's resonant wavelength will immediately drop below 1×10^{-8}.

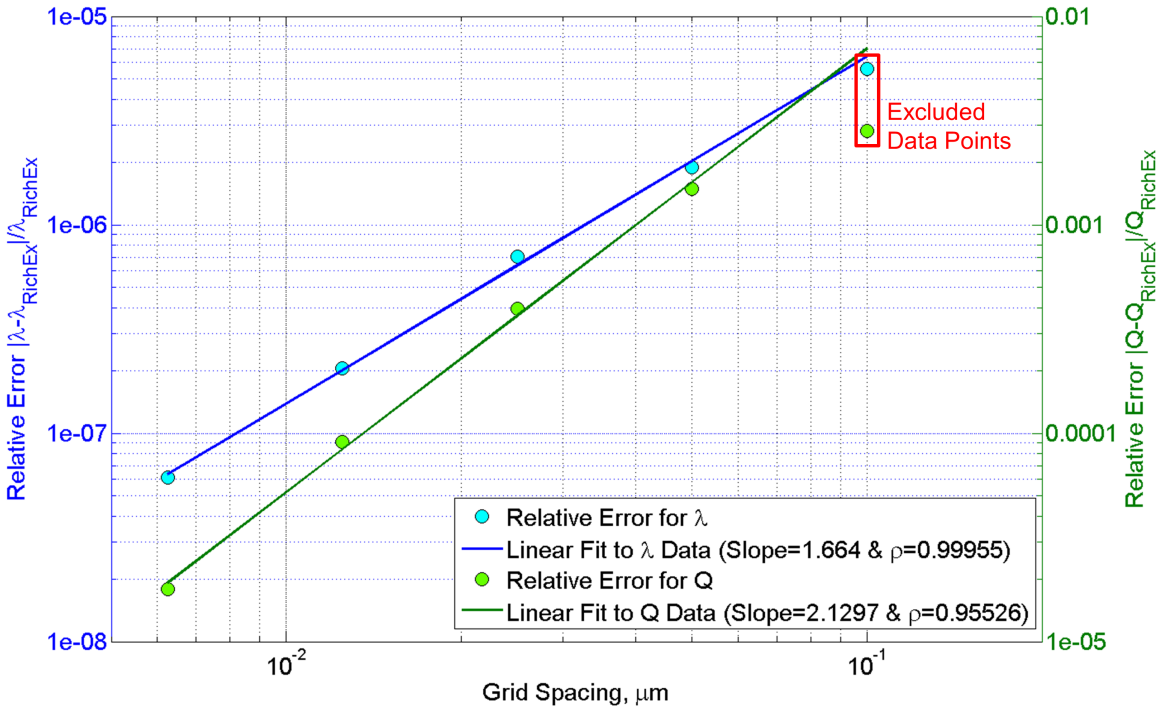

Figure 4.6: Resonant wavelength and quality factor relative error convergence plots of the 636$^{\text{th}}$ fundamental quasi-TE mode for a uniformly gridded silica microtoroid surrounded by water. The symbols ρ correspond to Pearson's linear correlation coefficients.

Actual characterization of the convergence rate is imperative if we are to substantiate the claims made in Section 3.2. A route that establishes the order of accuracy n comes from the relationship between the uniform grid spacing Δ and the eigenvalue.

That is to say, for a difference between an approximation $\widetilde{\lambda}_\Delta$ and a hypothetically exact λ, there is a constant C such that

$$\left|\widetilde{\lambda}_\Delta - \lambda\right| \leq C\Delta^n \tag{4.5}$$

Focusing on equality alone, we may take a logarithm of both sides of (4.5) and obtain

$$\begin{aligned}\log_{10}\left|\widetilde{\lambda}_\Delta - \lambda\right| &= \log_{10}\left(C\Delta^n\right) \\ &= \log_{10}C + n\log_{10}\Delta\end{aligned} \tag{4.6}$$

Through sequentially halving Δ we anticipate a linear log-log plot of $\log_{10}\left|\widetilde{\lambda}_\Delta - \lambda\right|$ versus $\log_{10}\Delta$ for a sizeable interval, wherein the slope n is the convergence rate we seek. Accordingly, Figure 4.6 is such a plot for λ_{Res} and Q at $\Delta = 100,\ 50,\ 25,\ 12.5,$ and 6.25 nm using Richardson extrapolated data points (explained in Appendix C) as references. The lines of best fit show a convergence rate near 2 for the finest grids, which is clearly in agreement with the finite difference mode solver's formulation.

4.2 Plasmonic Microdisk

B. Min *et al.* [78], among many research groups, looked beyond ordinary WGM resonators by introducing feasible surface plasmon polariton excitation. Evanescently bound and dielectric eigenmodes for a dominantly plasmonic architecture, such as a silica microdisk with a thin metal layer, suffer from a Q-factor reduction of several orders of magnitude due to a large intrinsic metal loss. This is the price paid for coupling to surface plasmons and the ensuing compression of the electromagnetic fields, offering meaningful sensitivity gains (in a localized sense) for particle detection [10, 11, 12], spontaneous emission enhancements [91], and miniaturization to deep subwavelength plasmonic WGM devices [92]. In this way, a magnified near-field intensity at hot spots can induce strong light-mater interactions that are vital to cavity QED [93].

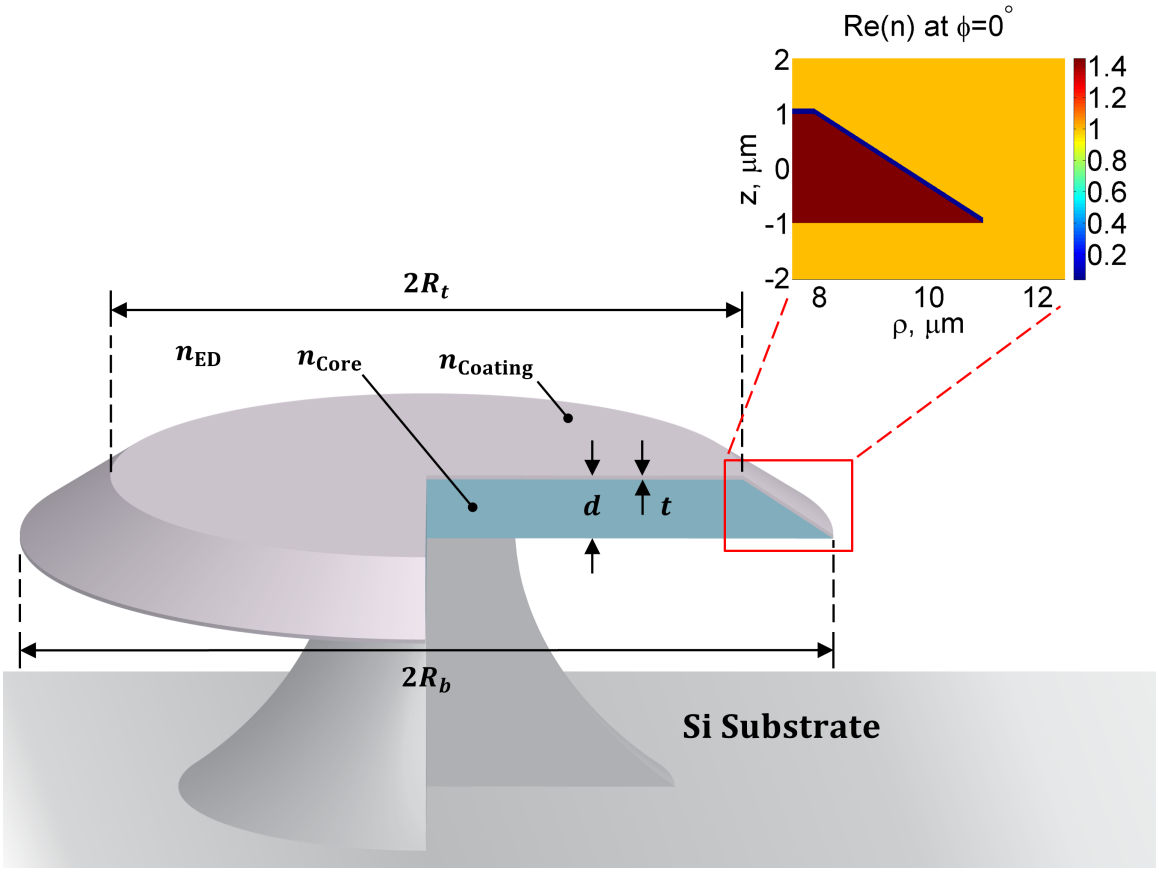

Figure 4.7: Cross-sectional diagram of a silver-coated silica microdisk enclosed by air accompanied by the refractive index profile for $\lambda = 1062.45$ nm.

The optical cavity of Figure 4.7, originating from [78], may receive phase-matched optical input from a tapered waveguide. The silica microdisk template with the depicted wedge generally reaches quality factors $> 5 \times 10^7$ with little scattering loss [94]. After depositing a noble metal (e.g. silver) onto the top surface through sputtering, SPP WGM's at the metal-dielectric interface and dielectric guided WGM's are able to propagate. Table 4.2 lists the simulation settings for modelling eigenmodes with $m = 85$ at the near-infrared wavelength of 1062.45 μm. This happens to be the aforementioned paper's numerical resonant wavelength of the fundamental $\mathrm{SPP}_{1,m}$ mode (of highest Q within the azimuthal mode order range), as will soon be inspected in the following pages. We are also obligated to maintain the grid spacing of both $\Delta\rho$ and Δz below 30 nm to faithfully emulate the sharp corners and inclined Ag layer in the discretized cross section.

Finite Difference Grid	
Uniform Grid Spacings	$\Delta\rho = \Delta z = 25$, 12.5, 6.25, & 3.125 nm
Excitation Source	
Operational Wavelength	$\lambda = 1062.45$ nm
Geometry	
Top Radius	$R_t = 7.9$ μm
Bottom Radius	$R_b = 11$ μm
Disk Thickness	$d = 2$ μm
Metal Coating Thickness	$t = 100$ nm
Materials	
Core/Microcavity: SiO_2	$n_{\text{Core}} = 1.450 + i(6 \times 10^{-8})$
Metal Coating: Ag	$n_{\text{Coating}} = 0.0400 + i7.598$ [95]
External Dielectric: Air	$n_{\text{ED}} = 1.000274$
Resonance	
Azimuthal Mode Order	$m = 85$

Table 4.2: SPP WGM simulation parameters for a plasmonic microdisk.

Figures 4.8 and 4.9 show the transverse field distributions and absolute value squared of the total electric fields for the two lowest-order SPP whispering-gallery modes of the silica microdisk with a silver coating, enveloped by air. The disk core thickness $d = 2$ μm, thickness of the silver coating $t = 100$ nm, top radius $R_t = 7.9$ μm, bottom radius $R_b = 11$ μm, and node separation $\Delta\rho = \Delta z = 3.125$ nm. What is unique to these modes is their self-consistency condition at a single interface, ensured by the negative relative permittivity of the metal. There is rapid decay into the silver coating as well as continuous E_ρ and discontinuous E_z on each side of the SiO_2-air interface at the bottom of the microdisk. The shorter wavelength of the SPP WGM with respect to free-space radiation reminds us as to why we must phase-match (i.e. simultaneously conserve photon momentum and energy) to couple into these modes from a tapered fiber. Moreover, the wedge's sharp tip behaves much like a lightning rod in the way that it draws the peak energy density to said tip. Due

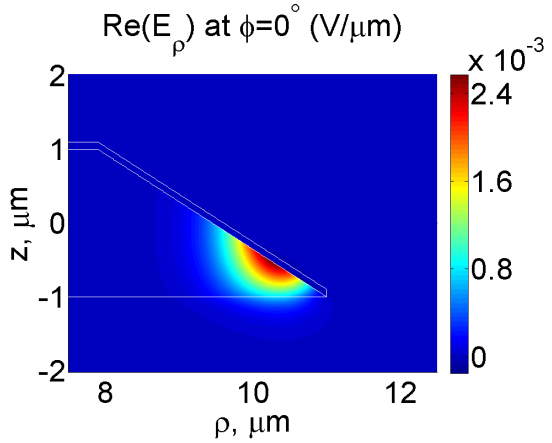

(a)

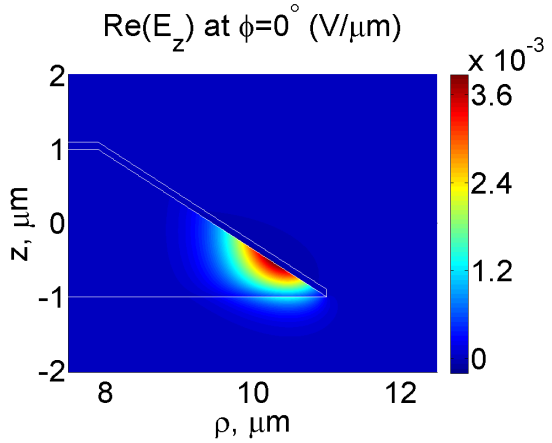

(b)

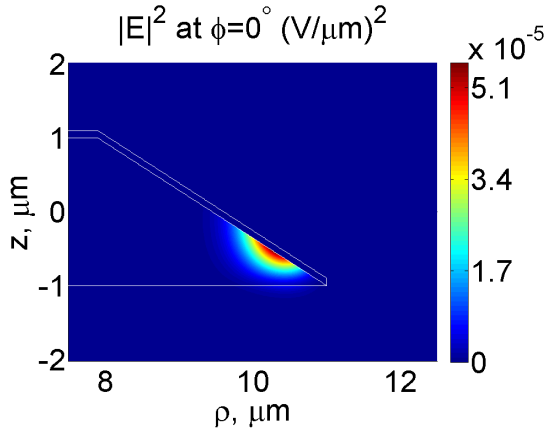

(c)

Figure 4.8: $\mathrm{SPP}_{1,m}$ eigenmode of the Ag-coated SiO_2 microdisk in air for $m = 85$. (a) and (b) are the real parts of the transverse field components while (c) is the absolute value of the total electric field squared. $\lambda_{\mathrm{Res}} = 1061.310$ μm and $Q = 1.77 \times 10^3$.

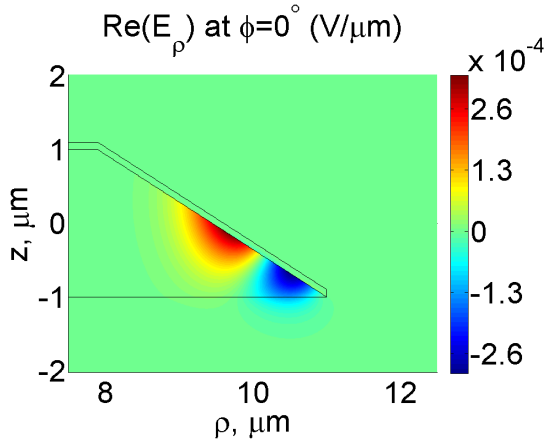

(a)

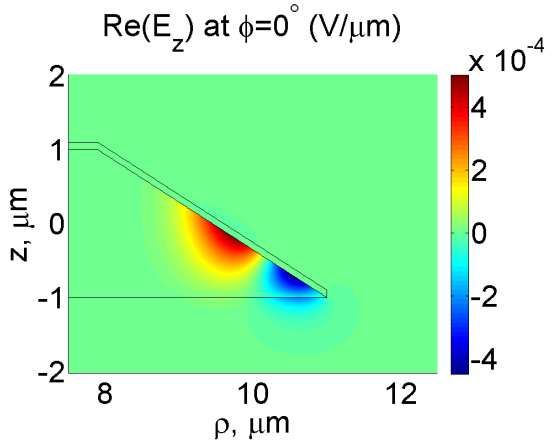

(b)

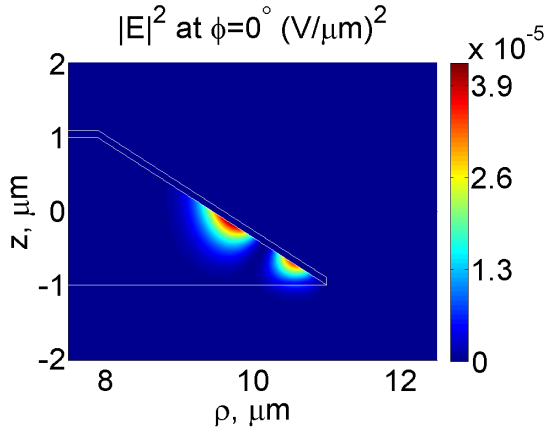

(c)

Figure 4.9: $SPP_{2,m}$ eigenmode of the Ag-coated SiO_2 microdisk in air for $m = 85$. (a) and (b) are the real parts of the transverse field components while (c) is the absolute value of the total electric field squared. $\lambda_{\text{Res}} = 1003.511$ μm and $Q = 1.44 \times 10^3$.

to the scale of this extremity and the computational resource limited mesh density, unavoidable discrepancies in the calculated eigenwavelengths will arise.

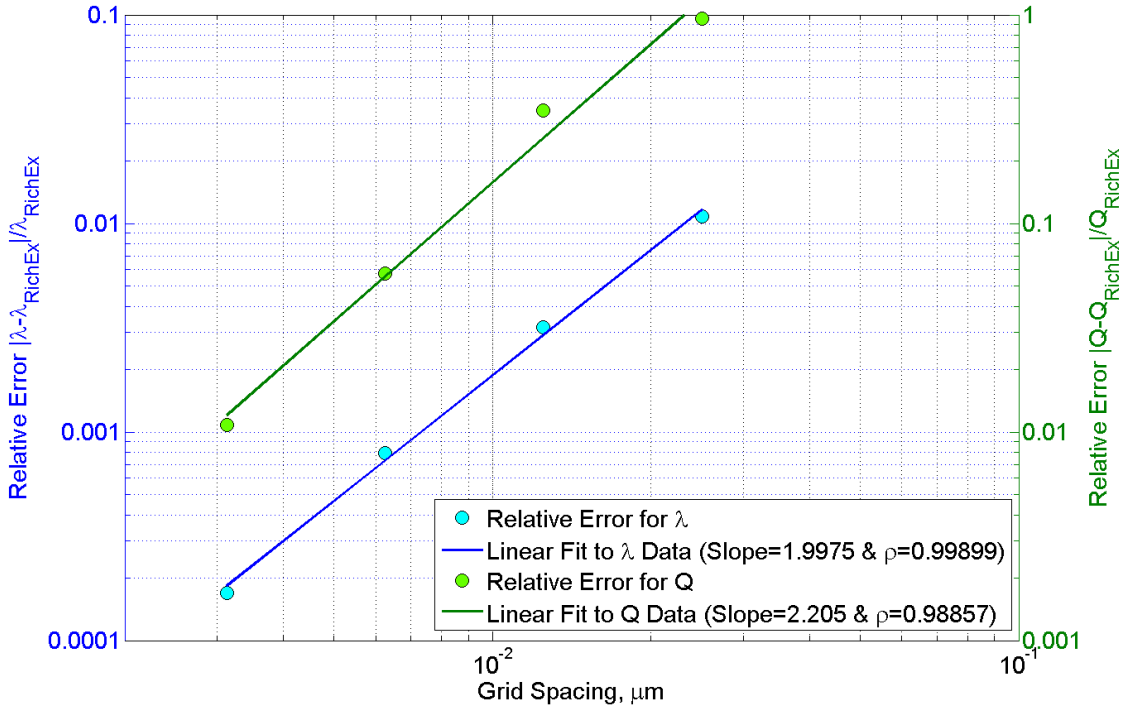

Figure 4.10: Resonant wavelength and quality factor relative error convergence plots of the fundamental $\mathrm{SPP}_{1,85}$ mode for a uniformly gridded silver-coated silica microdisk in air. The correlation coefficient ρ, more precisely, measures the strength and direction of a linear association.

The Q-factor prediction of the finite element method used by B. Min *et al.* for the $\mathrm{SPP}_{1,m}$ eigenmode is 1.80×10^3, in contrast to the currently presented mode solver's $Q = 1.77 \times 10^3$ at $\Delta\rho = \Delta z = 3.125$ nm. Compiling this with their resonant wavelength and our own $\lambda_{\mathrm{Res}} = 1061.310$ μm, the relative errors $|\lambda_{\mathrm{Res,FD}} - \lambda_{\mathrm{Res,FE}}|/\lambda_{\mathrm{Res,FE}} = 1.07 \times 10^{-3}$ and $|Q_{\mathrm{FD}} - Q_{\mathrm{FE}}|/Q_{\mathrm{FE}} = 1.67 \times 10^{-2}$. Again the growth in disparity from Section 4.1 can be traced to the grid resolution at the acute edge of the plasmonic microdisk, as the computation for the given number of nodes already occupies $>$ 25.0 GB of memory. For completeness and further verification, convergence of λ_{Res} and Q at a rate of 2 for this resonator is demonstrated in Figure 4.10 by halving $\Delta\rho = \Delta z = 25$ nm three times.

4.3 Weak Modal Perturbations

The wide range of scales involved in WGM microcavity based sensing inevitably demands flexible grid schemes. Nonequidistant discretization, included within the full-vector formulation of Section 3.3, yields meshes capable of preserving the fine surface curvature of minuscule objects without squandering memory space on regions with less significant permittivity structure and/or scarce optical energy. To realize this for a given dimension $x = \rho$ or z, we introduce a grid growth factor

$$g_n = \frac{1 - \zeta^{-1} e^{-\left(\frac{x_n - \eta}{\xi}\right)^2}}{1 - \zeta^{-1}} \tag{4.7}$$

such that the initial x_i approaches $x_f = x_N$ via $x_n = x_i + (n-1)\Delta x$, $n = 1, 2, 3, ..., N$, Δx is constant, and the new M points with constant ΔX are

$$X_m = \begin{cases} X_i & \text{if } m = 1 \\ X_{m-1} + g_{m-1}\Delta X & \text{if } 1 < m \leq M \end{cases} \tag{4.8}$$

where the purely real constant $\xi > 0$ must satisfy

$$\begin{aligned} \sum_{m=2}^{M} (X_m - X_{m-1}) &= \sum_{m=1}^{M-1} g_m \Delta X \\ &= X_f - X_i \end{aligned} \tag{4.9}$$

ζ is slightly larger than 1, $\eta \geq 0$, and it follows that $X_m - X_{m-1}$ monotonically increases (i.e. the Gaussian $1 - (1 - \zeta^{-1}) g_{m-1}$ monotonically decreases) as one departs from $x_{m-1} = \eta$ towards $\pm\infty$. This way, the minimum $X_m - X_{m-1} = \Delta X$ is reached at $x_{m-1} = \eta$. Through optimization we can find ξ's for the ρ and z domains, η's depending on the position of the highly refined zone, and one shared ζ.

In light of promising experimental advancements in the field [13, 14], we will now adhere to the topic of WGM detection. A spherical, 50-nm polystyrene nanoparticle binding to the equator of the silica microtoroid of Section 4.1 is portrayed in Figure 4.11 for an aqueous environment. The particle is meant to interact with revolving light at a point close to the peak modal intensity, as to maximize the optical resonant

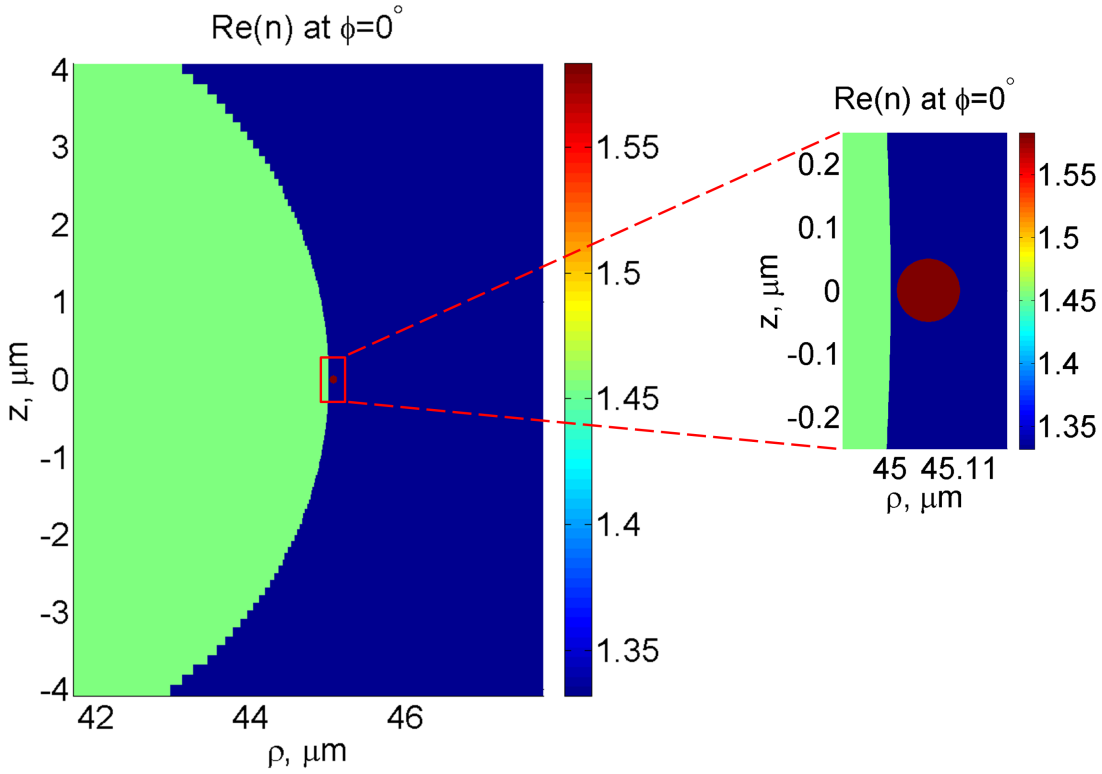

Figure 4.11: Refractive index's real part at $\lambda = 633$ nm for a silica microtoroid and $\phi = 0°$-centered polystyrene nanobead system in water.

wavelength shift. Following data entry according to Table 4.3, there are a few key elements of our numerical approach that we should contemplate. Asymmetry along the ϕ-direction produces mode mismatch losses between cross sections, that is quantified by a new component of the imaginary part of $\widetilde{m}$ [17]:

$$m_{\mathrm{mm}}(\phi_i) = -\lim_{\delta\phi\to 0} \frac{\ln\left[\frac{1}{2Z_o}\iint n(\rho,z,\phi_i+\delta\phi)e^*(\rho,z,\phi_i+\delta\phi)e(\rho,z,\phi_i)d\rho dz\right]}{\delta\phi} \tag{4.10}$$

at the i^{th} cross section, where the impedance of free space $Z_o = 377\ \Omega$ and each normalized field $e(\rho,z,\phi_i)$ satisfies

$$\frac{1}{2Z_o}\iint n(\rho,z,\phi_i)|e(\rho,z,\phi_i)|^2 d\rho dz = 1 \tag{4.11}$$

Finite Difference Grid	
Nonuniform Grid Spacing Minima	$\Delta\rho = \Delta z = 0.1$, 0.25, 0.5, 0.75 & 0.9 nm
Excitation Source	
Operational Wavelength	$\lambda = 633$ nm
Geometry	
Major Radius	$R = 40$ μm
Minor Radius	$r = 5$ μm
Aspect Ratio	$\frac{R}{r} = 8$
Particle Radii	$r_p = 10$ to 100 nm in 10 nm increments
Gap Distance at $\phi = 0°$	$d_{\text{Gap}} = 10$ nm
Materials	
Core/Microcavity: SiO_2	$n_{\text{Core}} = 1.457 + i(6.95 \times 10^{-11})$
Cladding/External Dielectric: H_2O	$n_{\text{Cladding}} = 1.332 + i(1.47 \times 10^{-8})$
Particle: $(C_8H_8)_n$	$n_p = 1.583 + i(5.29 \times 10^{-4})$
Resonance	
Azimuthal Mode Order	$m = 636$

Table 4.3: Perturbed WGM simulation parameters for dielectric particle adsorption onto a microtoroid.

We must also mathematically capture the absorption loss, from a weighted averaging of material attenuation coefficients, that was the sole determining factor of the Q for the ideal cavity:

$$m_{\text{abs}} = \frac{m}{\text{Re}(\widetilde{\lambda}_{\text{Res}})/[2\text{Im}(\widetilde{\lambda}_{\text{Res}})]} \tag{4.12}$$

The revised Q thus becomes

$$\begin{aligned} Q &= \frac{1}{\frac{1}{Q_{\text{abs}}} + \frac{1}{Q_{mm}}} \\ &= \frac{2\pi m}{2\int_0^{2\pi} \left[m_{\text{abs}}(\phi) + m_{\text{mm}}(\phi)\right] d\phi} \end{aligned} \tag{4.13}$$

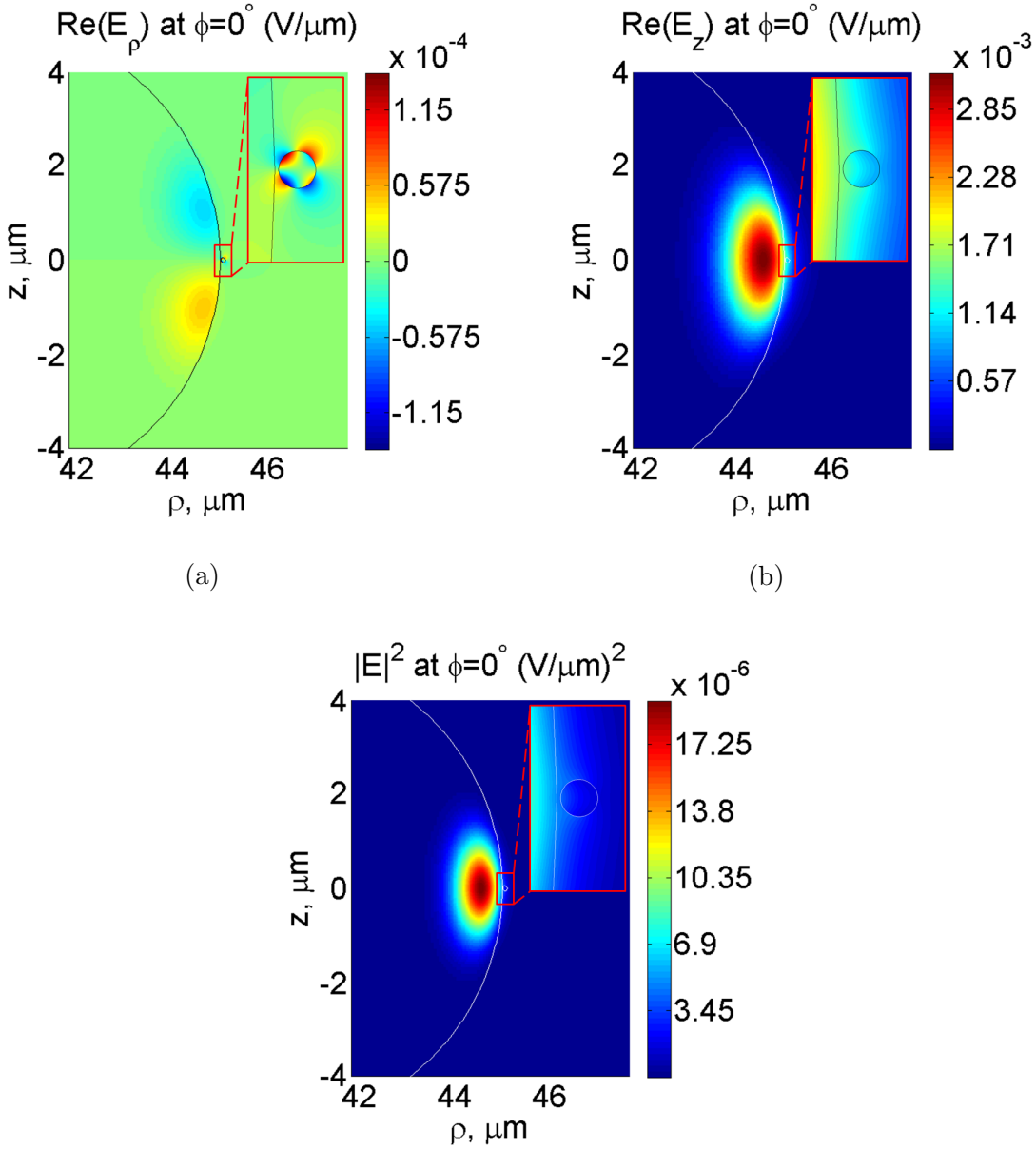

Figure 4.12: Perturbed fundamental quasi-TE mode for a silica microtoroid with an attracted 50-nm polystyrene particle in liquid water, where $m = 636$, $\Delta\lambda_{\text{Res}} = 19.312$ fm, and $Q = 1.15 \times 10^7$. (a) and (b) are respectively the real parts of the transverse E_ρ and E_z while (c) is the modulus of the total electric field squared $|\vec{E}|^2$. The insets are magnified views of the distributions near the nanobead.

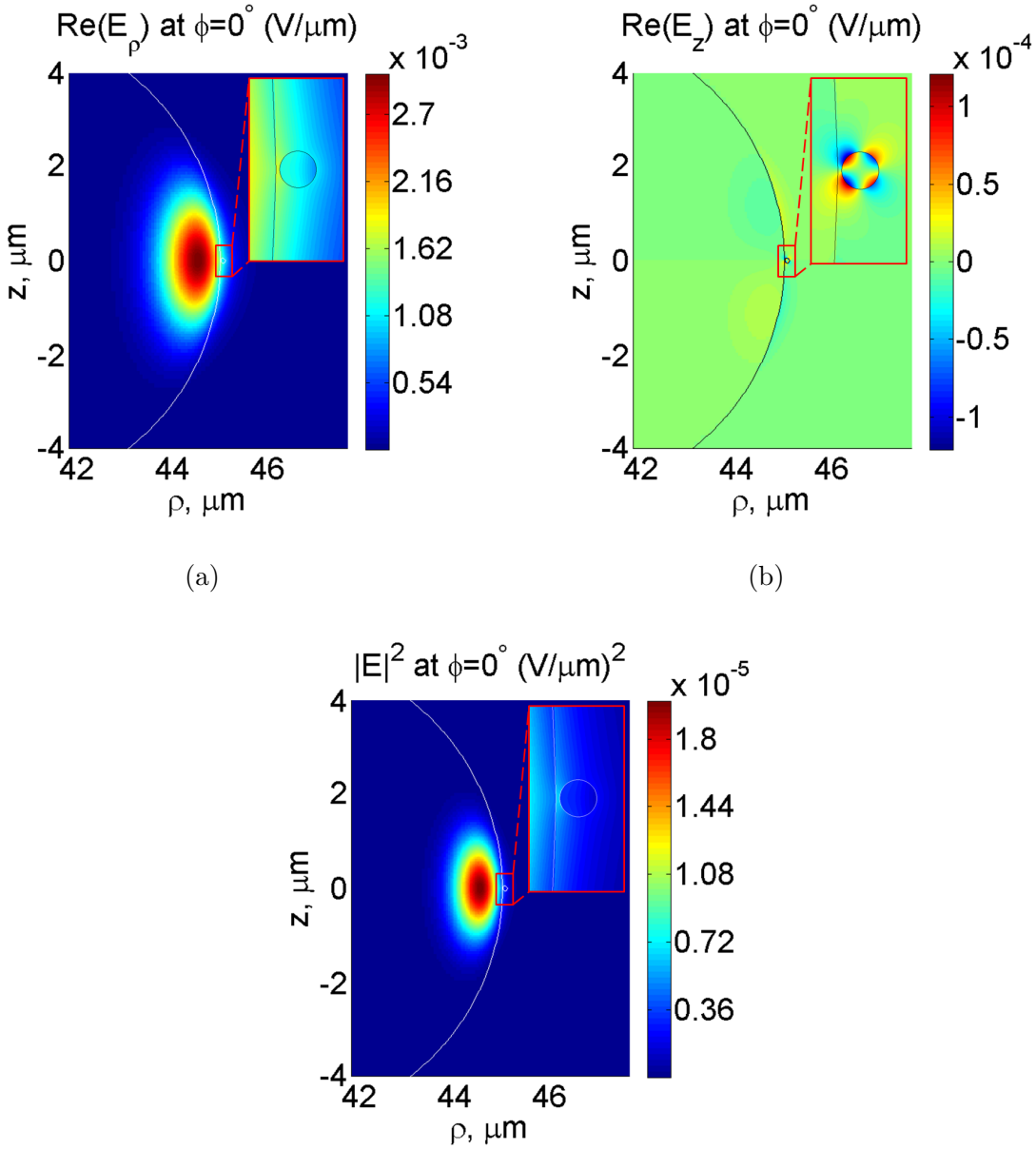

Figure 4.13: Perturbed fundamental quasi-TM mode for a silica microtoroid with an attracted 50-nm polystyrene particle in liquid water, where $m = 636$, $\Delta\lambda_{\text{Res}} = 16.821$ fm, and $Q = 1.15 \times 10^7$. (a) and (b) are respectively the real parts of the transverse E_ρ and E_z while (c) is the modulus of the total electric field squared $|\vec{E}|^2$. The insets are magnified views of the distributions near the nanobead.

Resonant wavelength shifts $\Delta\lambda_{\text{Res}}$ brought on by this weak perturbation are calculable in an analogous fashion, in that we may azimuthallly integrate $\Delta\lambda_{\text{Res}}(\phi) - \Delta\lambda_{\text{Res,Ideal}}$. In short, for a particle situated between ϕ_i and $\phi_i + \Delta\phi$,

$$\Delta\lambda_{\text{Res}} = \frac{\int_{\phi_i}^{\phi_i+\Delta\phi} \left[\lambda_{\text{Res}}(\phi) - \lambda_{\text{Res,Ideal}}\right] d\phi}{2\pi} \tag{4.14}$$

Alterations of the WGM's, as in Figures 4.12 and 4.13, encompass moderate distortion about the 50-nm nanobead with finest $\Delta\rho = \Delta z = 500$ pm, Q deterioration by two orders of magnitude, and an increase of a few femtometers in λ_{Res} (i.e. the first shift $\Delta\lambda_{\text{Res}} = 19.312$ fm is consistent with published work [13]). Continuity relations hold across principal interfaces and Figure 4.14's perturbed fundamental quasi-TM mode's $\text{Re}(E_\rho)$ along the $z = 0$ line has a series of telling steps. Effectively equivalent

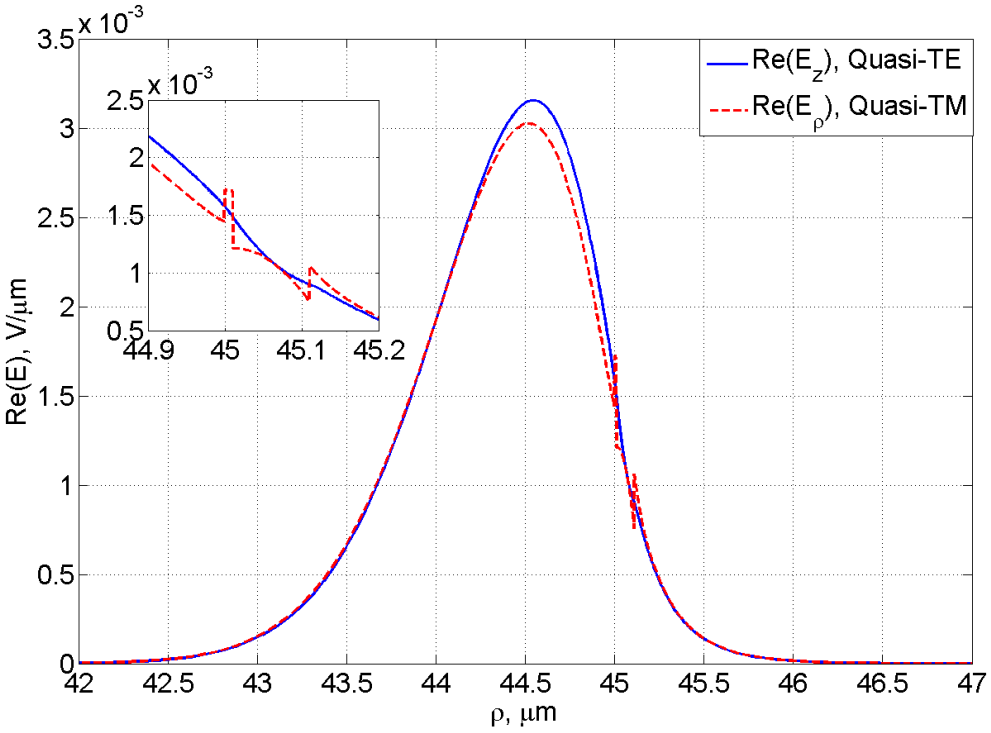

Figure 4.14: The major electric fields' real parts for the perturbed 636$^{\text{th}}$ fundamental quasi-TE and quasi-TM modes of the microtoroid-nanobead system.

Q-factors for the modes come from the pervasive/dominant mode mismatch loss, made clear if the cross sections are dissected in terms of the components of the imaginary part of the azimuthal mode number m_i as in Figure 4.15. The peak of m_{abs} and largest amount of absorption are found at the central ϕ-slice of the particle but m_{mm} rather dips due to rising overlap integrals of adjacent ϕ-dependent eigenmodes.

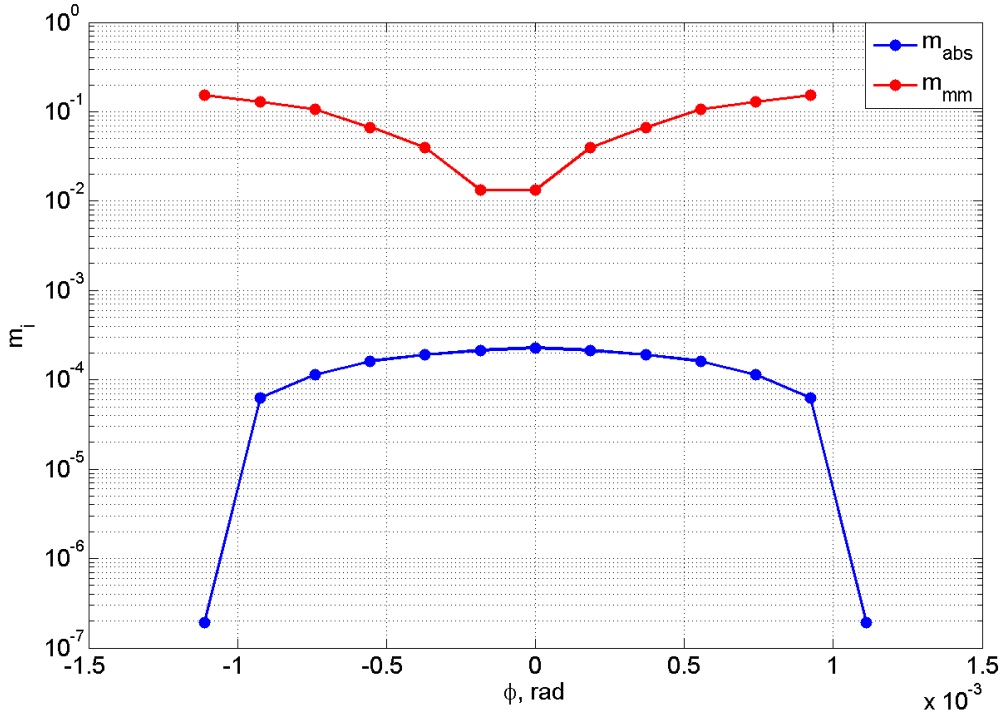

Figure 4.15: Imaginary part of $\tilde{\text{m}}$ as a function of ϕ for a 50-nm bound polystyrene bead. The variable m_{mm} drops to 0 once neighbouring modes are invariant, hence its final datum is omitted.

Lastly, dielectric particles of assorted radii binding to the microtoroid surface are simulated. Selecting a decade from $r_p = 0.01$ to 0.1 μm as well as minima $\Delta\rho = \Delta z = 0.1$, 0.25, 0.5, 0.75, and 0.9 nm, the total Q and $\Delta\lambda_{\text{Res}}$'s dependence on r_p are recorded (namely Figure 4.16). The escalating resonant wavelength shift is in line with earlier results [17] and first-order perturbation theory [39] adapted herein, conforming to formula (2.7). Section 4.3's evaluation assigns a single eigenmode to the optically resonating cavity, yet there is a possibility of inserting coupling between several WGM's (e.g. appending the methods of [18]) as to improve numerical accuracy.

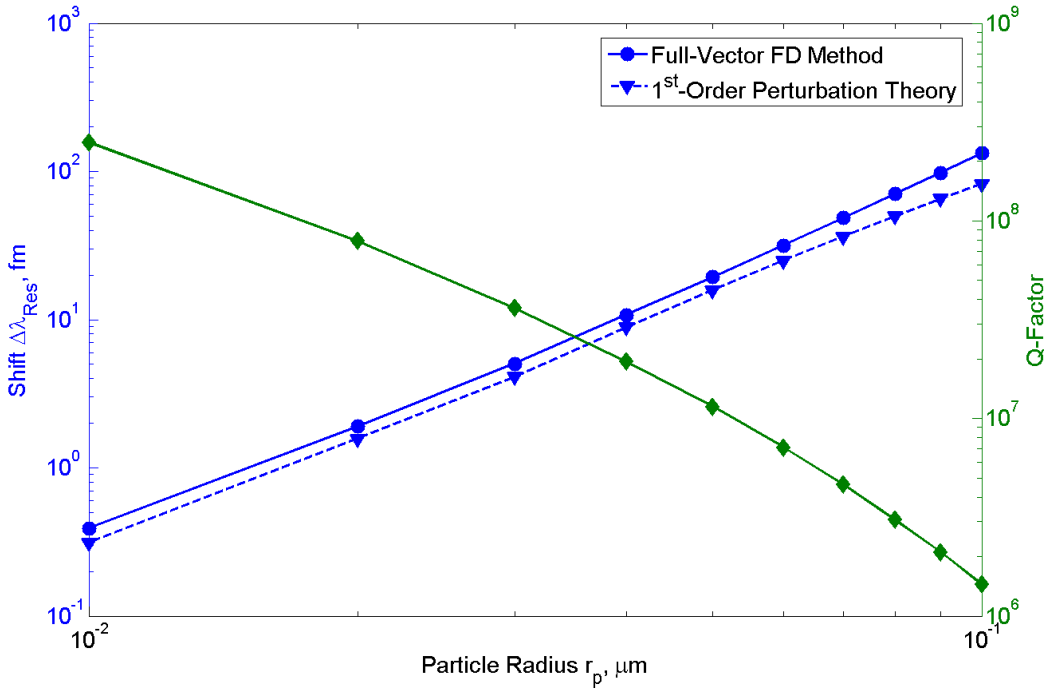

Figure 4.16: Resonant wavelength fluctuation and quality factor upon surface binding of diversely-sized polystyrene nanoparticles.

Chapter 5

Conclusions

5.1 Summary

An efficient finite difference whispering-gallery mode solver with complete coupling between field components for dielectric heterogeneity and grid nonuniformity was presented. Groundwork laid in [27] was expanded upon as the solver was re-evaluated to provide compatibility with the curvilinear coordinate systems befitting WGM technology. At its inception, the combined abstraction of the Taylor series and alignment transform at interfaces enables the simulation of axisymmetric and axisasymmetric optical resonator systems. The latter is achieved by adopting mode matching or any propagation-inclusive numerical study of whispering-gallery modes. Versatility, precision, and accuracy in this thesis's approach is evidenced by its results compared to those of known publications [13, 17, 78] for three arrangements: 1) elementary, plasmonic, and dielectric particle-perturbed microcavities.

Convergence of order 2 for uniform grids was theorized and proven for the first two cases. Further gains are conceivable by enlarging the stencil and conserving higher-order terms of the modified Taylor series. Universally, eigenmodes, eigenwavelengths, and quality factors were readily tabulated within less than 1 minute per solver iteration for node totals in the neighbourhood of 3×10^5, with relative errors (w.r.t. external references) as small as 1.42×10^{-5} for a highly dense mesh. The localized electromagnetic fields also display appropriately physical patterns. In all, this full-vector finite difference solver serves as a critical building block in the development of thorough computational tools for whispering-gallery mode based research.

5.2 Future Work

Firstly, accurate radiative loss is contingent on replacing the current boundary conditions with a perfectly matched layer that has absorption coefficients separately optimized along $\hat{\rho}$ and $\hat{z}$. The mode solver can also profit from coordinate transformations tailored to significantly curved interfaces. Strong modal perturbations, such as those from plasmonic nanoantennas, should be assessed with the discussed methodology. Many orientations of the perturbing specimen can be considered, e.g. to optimize the enhancement in optical sensing signals. Disparities between processed and expected data for this scenario have been discovered and are likely rectifiable via the advised refinements of this subsection. Going forward, a comprehensive numerical analysis of whispering-gallery mode microcavities should take bi-directional propagation from mode splitting into account.

Appendix A

Derivation of 1st and 2nd-Order Interface Continuity Relations

Mirroring [96], Maxwell's equations for a single medium with a local Cartesian coordinate system (n, t, z) are

$$\frac{\partial E_z}{\partial t} - \frac{\partial E_t}{\partial z} = -i\omega\mu_o H_n \tag{A.1}$$

$$\frac{\partial E_n}{\partial z} - \frac{\partial E_z}{\partial n} = -i\omega\mu_o H_t \tag{A.2}$$

$$\frac{\partial E_t}{\partial n} - \frac{\partial E_n}{\partial t} = -i\omega\mu_o H_z \tag{A.3}$$

$$\frac{\partial E_n}{\partial n} + \frac{\partial E_t}{\partial t} + \frac{\partial E_z}{\partial z} = 0 \tag{A.4}$$

$$\frac{\partial H_z}{\partial t} - \frac{\partial H_t}{\partial z} = i\omega\epsilon E_n \tag{A.5}$$

$$\frac{\partial H_n}{\partial z} - \frac{\partial H_z}{\partial n} = i\omega\epsilon E_t \tag{A.6}$$

$$\frac{\partial H_t}{\partial n} - \frac{\partial H_n}{\partial t} = i\omega\epsilon E_z \tag{A.7}$$

$$\frac{\partial H_n}{\partial n} + \frac{\partial H_t}{\partial t} + \frac{\partial H_z}{\partial z} = 0 \tag{A.8}$$

Assuming propagation is along $\hat{z}$ and that the propagation constant is β, (A.3) and (A.4) can be reduced to

$$\frac{\partial E_t}{\partial n} - \frac{\partial E_n}{\partial t} = -i\omega\mu_o H_z \tag{A.9}$$

$$\frac{\partial E_n}{\partial n} + \frac{\partial E_t}{\partial t} = i\beta E_z \tag{A.10}$$

In the transverse direction $\hat{t}$ with respect to an interface, the field quantities are single-valued, bounded, and possess continuous distributions as do their derivatives. Thus given equations (3.104) and (3.105), the first four relations are

$$\left.\frac{\partial E_n}{\partial t}\right|_R = \frac{\epsilon_L}{\epsilon_R}\left.\frac{\partial E_n}{\partial t}\right|_L \tag{A.11}$$

$$\left.\frac{\partial^2 E_n}{\partial t^2}\right|_R = \frac{\epsilon_L}{\epsilon_R}\left.\frac{\partial^2 E_n}{\partial t^2}\right|_L \tag{A.12}$$

$$\left.\frac{\partial E_t}{\partial t}\right|_R = \left.\frac{\partial E_t}{\partial t}\right|_L \tag{A.13}$$

$$\left.\frac{\partial^2 E_t}{\partial t^2}\right|_R = \left.\frac{\partial^2 E_t}{\partial t^2}\right|_L \tag{A.14}$$

Revisiting (A.10) having found (A.13) and further assuming z-symmetry of the permittivity,

$$\begin{aligned}
\left.\frac{\partial E_n}{\partial n}\right|_R + \left.\frac{\partial E_t}{\partial t}\right|_R &= i\beta E_z|_R = i\beta E_z|_L \\
\left.\frac{\partial E_n}{\partial n}\right|_R + \cancel{\left.\frac{\partial E_t}{\partial t}\right|_R} &= \left.\frac{\partial E_n}{\partial n}\right|_L + \left.\frac{\partial E_t}{\partial t}\right|_L = \left.\frac{\partial E_n}{\partial n}\right|_L + \cancel{\left.\frac{\partial E_t}{\partial t}\right|_R} \\
\left.\frac{\partial E_n}{\partial n}\right|_R &= \left.\frac{\partial E_n}{\partial n}\right|_L
\end{aligned} \tag{A.15}$$

and we proceed to state

$$\left.\frac{\partial^2 E_n}{\partial n \partial t}\right|_R = \left.\frac{\partial^2 E_n}{\partial n \partial t}\right|_L \tag{A.16}$$

Now applying (A.9) to both sides of the interface and employing (A.11),

$$\left.\frac{\partial E_t}{\partial n}\right|_R - \left.\frac{\partial E_n}{\partial t}\right|_R = -\,i\omega\mu_o H_z|_R = -\,i\omega\mu_o H_z|_L$$

$$\left.\frac{\partial E_t}{\partial n}\right|_R - \frac{\epsilon_L}{\epsilon_R}\left.\frac{\partial E_n}{\partial t}\right|_L = \left.\frac{\partial E_t}{\partial n}\right|_L - \left.\frac{\partial E_n}{\partial t}\right|_L$$

$$\left.\frac{\partial E_t}{\partial n}\right|_R = \left.\frac{\partial E_t}{\partial n}\right|_L + \left(\frac{\epsilon_L}{\epsilon_R} - 1\right)\left.\frac{\partial E_n}{\partial t}\right|_L \tag{A.17}$$

and

$$\left.\frac{\partial^2 E_t}{\partial n \partial t}\right|_R = \left.\frac{\partial^2 E_t}{\partial n \partial t}\right|_L + \left(\frac{\epsilon_L}{\epsilon_R} - 1\right)\left.\frac{\partial^2 E_n}{\partial t^2}\right|_L \tag{A.18}$$

Finally, from (A.12) and the Helmholtz equation for E_n

$$\left.\frac{\partial^2 E_n}{\partial n^2}\right|_L + \left.\frac{\partial^2 E_n}{\partial t^2}\right|_L + \left.\frac{\partial^2 E_n}{\partial z^2}\right|_L + k_o^2\epsilon_L\, E_n|_L = 0$$

$$\left.\frac{\partial^2 E_n}{\partial n^2}\right|_L + \left.\frac{\partial^2 E_n}{\partial t^2}\right|_L + (k_o^2\epsilon_L - \beta^2)\, E_n|_L = 0$$

$$\frac{\epsilon_L}{\epsilon_R}\left.\frac{\partial^2 E_n}{\partial n^2}\right|_L + \frac{\epsilon_L}{\epsilon_R}\left.\frac{\partial^2 E_n}{\partial t^2}\right|_L + \frac{k_o^2\epsilon_L}{\epsilon_R}\epsilon_L\, E_n|_L = \frac{\beta^2}{\epsilon_R}\epsilon_L\, E_n|_L = \frac{\beta^2}{\cancel{\epsilon_R}}\cancel{\epsilon_R}\, E_n|_R$$

$$\frac{\epsilon_L}{\epsilon_R}\left.\frac{\partial^2 E_n}{\partial n^2}\right|_L + \cancel{\left.\frac{\partial^2 E_n}{\partial t^2}\right|_R} + \frac{k_o^2\epsilon_L}{\epsilon_R}\epsilon_L\, E_n|_L = \left.\frac{\partial^2 E_n}{\partial n^2}\right|_R + \cancel{\left.\frac{\partial^2 E_n}{\partial t^2}\right|_R} + k_o^2\epsilon_R\, E_n|_R$$

$$\frac{\epsilon_L}{\epsilon_R}\left.\frac{\partial^2 E_n}{\partial n^2}\right|_L + \frac{k_o^2\epsilon_L}{\epsilon_R}\epsilon_L\, E_n|_L = \left.\frac{\partial^2 E_n}{\partial n^2}\right|_R + k_o^2\epsilon_L\, E_n|_L$$

$$\downarrow$$

$$\left.\frac{\partial^2 E_n}{\partial n^2}\right|_R = \frac{\epsilon_L}{\epsilon_R}\left.\frac{\partial^2 E_n}{\partial n^2}\right|_L + k_o^2\frac{\epsilon_L(\epsilon_L - \epsilon_R)}{\epsilon_R}\, E_n|_L \tag{A.19}$$

as well as from (A.14) and the Helmholtz equation for E_t

$$\left.\frac{\partial^2 E_t}{\partial n^2}\right|_R + \left.\frac{\partial^2 E_t}{\partial t^2}\right|_R + (k_o^2\epsilon_R - \beta^2)\ E_t|_R = 0$$

$$\left.\frac{\partial^2 E_t}{\partial n^2}\right|_R + \left.\frac{\partial^2 E_t}{\partial t^2}\right|_R + k_o^2\epsilon_R\ E_t|_R = \beta^2\ E_t|_R = \beta^2\ E_t|_L$$

$$\left.\frac{\partial^2 E_t}{\partial n^2}\right|_R + \cancel{\left.\frac{\partial^2 E_t}{\partial t^2}\right|_L} + k_o^2\epsilon_R\ E_t|_L = \left.\frac{\partial^2 E_t}{\partial n^2}\right|_L + \cancel{\left.\frac{\partial^2 E_t}{\partial t^2}\right|_L} + k_o^2\epsilon_L\ E_t|_L$$

$$\left.\frac{\partial^2 E_t}{\partial n^2}\right|_R = \left.\frac{\partial^2 E_t}{\partial n^2}\right|_L + k_o^2(\epsilon_L - \epsilon_R)\ E_t|_L \qquad \text{(A.20)}$$

Appendix B

LUP Decomposition

A. Turing proposed the LU decomposition method in 1948 [97] to lessen round-off errors in the processes of solving sets of linear equations and inverting matrices. His proposal was that a square $n \times n$ matrix $\mathbf{A}$ can be expressed as a matrix product

$$\mathbf{A} = \mathbf{LU} \tag{B.1}$$

where $\mathbf{L}$ and $\mathbf{U}$ are respectively $n \times n$ lower and upper triangular matrices. Factorization will fail, in some instances, if $\mathbf{A}$ is not subject to proper row and/or column orderings or permutations. A more generalized technique, named LU decomposition with partial pivoting or LUP decomposition, is able to accomplish numerically stable factorization of any square matrix. Given a permutation matrix $\mathbf{P}$ that is a row-permuted $n \times n$ identity matrix $\mathbf{I}$ such that $\mathbf{PP}^{\mathrm{T}} = \mathbf{I}$,

$$\begin{aligned} \mathbf{PA} &= \mathbf{LU} \\ &\downarrow \\ \mathbf{A} &= \mathbf{P}^{-1}\mathbf{LU} \end{aligned} \tag{B.2}$$

with

$$\mathbf{L} = \begin{bmatrix} l_{11} & 0 & \dots & 0 \\ l_{21} & l_{22} & \dots & 0 \\ \vdots & \vdots & \ddots & \vdots \\ l_{n1} & l_{n2} & \dots & l_{nn} \end{bmatrix} \tag{B.3}$$

$$\mathbf{U} = \begin{bmatrix} u_{11} & u_{12} & \dots & u_{1n} \\ 0 & u_{22} & \dots & u_{2n} \\ \vdots & \vdots & \ddots & \vdots \\ 0 & 0 & \cdots & u_{nn} \end{bmatrix} \tag{B.4}$$

An advantage of the above decomposition is that computing the determinant of **A** is reduced to multiplying either 1 or -1 by the products of the diagonal entries of **L** and **U**. Hence,

$$\begin{aligned} \det(\mathbf{A}) &= \det(\mathbf{P}^{-1}\mathbf{L}\mathbf{U}) \\ &= \det(\mathbf{P}^{-1})\det(\mathbf{L})\det(\mathbf{U}) \\ &= (-1)^k \left(\prod_{i=1}^{n} l_{ii}\right)\left(\prod_{j=1}^{n} u_{jj}\right) \end{aligned} \tag{B.5}$$

for k = number of row interchanges in the decomposition. Since **L** is usually chosen to be the unit triangular matrix, we can rely on the straightforward, less unreliable numerical operation

$$\begin{aligned}\log_{10}[\det(\mathbf{A})] &= \log_{10}\left[(-1)^k(1)\left(\prod_{j=1}^{n} u_{jj}\right)\right] \\ &= \log_{10}\left[(-1)^k\right] + \log_{10}\left(\prod_{j=1}^{n} u_{jj}\right) \\ &= \begin{cases} \sum_{j=1}^{n} \log_{10} u_{jj} & \text{if } n \text{ is even} \\ \frac{i\pi}{\ln 10} + \sum_{j=1}^{n} \log_{10} u_{jj} & \text{if } n \text{ is odd} \end{cases}\end{aligned} \tag{B.6}$$

improving the dynamic range.

Appendix C

Richardson Extrapolation

For a function $A(h)$ with continuous or discrete step size h, there is often an infinite sequence $A_n = A(h_n), n \in \mathbb{N}$ that converges for a monotonically decreasing h_n such that

$$\lim_{n->\infty} A_n = \lim_{h\to 0^+} A(h) = A \tag{C.1}$$

The series $A(h)$ for approximating A then takes the form

$$A(h) = A + \sum_{n=1}^{N} \alpha_n h^{k_n} + \mathrm{O}(h^{k_{N+1}}) \quad \text{as} \quad h \to 0^+ \tag{C.2}$$

where $k_1 < k_2 < ... < k_{N+1}$, $k_n \neq 0 \ \forall n$, and the limit A must exist if $k_1 > 0$. Supposing that h is sufficiently small and $k_1 > 0$,

$$A(h) - A = \mathrm{O}(h^{k_1}) \tag{C.3}$$

We must endeavour to reduce the error term $\mathrm{O}(h^{k_1})$, which seemingly calls for shrinking the step size h and reiterating (C.2). Considering that

$$A = A(h) + \alpha_1 h^{k_1} + \mathrm{O}(h^{k_2}) \tag{C.4}$$

and

$$A = A(h/s) + \alpha_1 (h/s)^{k_1} + \mathrm{O}(h^{k_2}) \tag{C.5}$$

for an unknown (immaterial) constant α_1 and some step size scaling factor s, we can multiply (C.5) by s^{k_1} and subtract it by (C.4). This leads to

$$(s^{k_1}-1)A = s^{k_1}A(h/s) - A(h) + \mathrm{O}(h^{k_2})$$
$$\downarrow$$
$$A = \frac{s^{k_1}A(h/s) - A(h)}{s^{k_1}-1} + \mathrm{O}(h^{k_2}) \tag{C.6}$$

A superior approximation of A can then always be found and error terms can be repeatedly lowered via the weighted average or Richardson extrapolation

$$A_{n+1}(h) = \frac{s^{k_n}A_n(h/s) - A_n(h)}{s^{k_n}-1} \tag{C.7}$$

with $A = A_{n+1}(h) + \mathrm{O}(h^{k_{n+1}})$ and the least rigorous estimate $A_1(h) = A(h)$. (C.7) can even be applied to identify the rate of convergence through a cross-comparison between approximations for different scaling factors. Implementations of Richardson extrapolation are elucidated in [98].

Bibliography

[1] K. J. Vahala. Optical microcavities. *Nature*, 424(6950):839–846, 2003.

[2] P. Zijlstra, P. M. R. Paulo, and M. Orrit. Optical detection of single non-absorbing molecules using the surface plasmon resonance of a gold nanorod. *Nat. Nanotechnol.*, 7(6):379–382, 2012.

[3] A. K. Naik, M. S. Hanay, W. K. Hiebert, X. L. Feng, and M. L. Roukes. Towards single-molecule nanomechanical mass spectrometry. *Nat. Nanotechnol.*, 4(7):445–450, 2009.

[4] T. Carmon, H. Rokhsari, L. Yang, T. J. Kippenberg, and K. J. Vahala. Temporal behavior of radiation-pressure-induced vibrations of an optical microcavity phonon mode. *Phys. Rev. Lett.*, 94(22):223902, 2005.

[5] T. J. Kippenberg, H. Rokhsari, T. Carmon, A. Scherer, and K. J. Vahala. Analysis of radiation-pressure induced mechanical oscillation of an optical microcavity. *Phys. Rev. Lett.*, 95(3):033901, 2005.

[6] H. Rokhsari, T. J. Kippenberg, T. Carmon, and K. J. Vahala. Radiation-pressure-driven micro-mechanical oscillator. *Opt. Express*, 13(14):5293–5301, 2005.

[7] S. M. Spillane, T. J. Kippenberg, O. Painter, and K. J. Vahala. Ideality in a fiber-taper-coupled microresonator system for application to cavity quantum electrodynamics. *Phys. Rev. Lett.*, 91(4):043902, 2003.

[8] T. J. Kippenberg, S. M. Spillane, and K. J. Vahala. Kerr-nonlinearity optical parametric oscillation in an ultrahigh-Q toroid microcavity. *Phys. Rev. Lett.*, 93(8):083904, 2004.

[9] S. M. Spillane, T. J. Kippenberg, and K. J. Vahala. Ultralow-threshold Raman laser using a spherical dielectric microcavity. *Nature*, 415(6872):621–623, 2002.

[10] S. I. Shopova, R. Rajmangal, S. Holler, and S. Arnold. Plasmonic enhancement of whispering-gallery-mode biosensor for single nanoparticle detection. *Appl. Phys. Lett.*, 98(24):243104, 2011.

[11] M. A. Santiago-Cordoba, S. V. Boriskina, F. Vollmer, and M. C. Demirel. Nanoparticle-based protein detection by optical shift of a resonant microcavity. *Appl. Phys. Lett.*, 99(7):073701, 2011.

[12] J. D. Swaim, J. Knittel, and W. P Bowen. Detection limits in whispering gallery biosensor with plasmonic enhancement. *Appl. Phys. Lett.*, 99(24):243109, 2011.

[13] T. Lu, H. Lee, T. Chen, S. Herchak, J.-H. Kim, S. E. Fraser, R. C. Flagan, and K. J. Vahala. High sensitivity nanoparticle detection using optical microcavities. *PNAS*, 108(15):5976–5979, 2011.

[14] M. D. Baaske, M. R. Foreman, and F. Vollmer. Single-molecule nucleic acid interactions monitored on a label-free microcavity biosensor platform. *Nat. Nanotechnol.*, 9(11):933–939, 2014.

[15] N. M. Alford, J. Breeze, S. J. Penn, and M. Poole. Layered Al_2O_3-TiO_2 composite dielectric resonators with tuneable temperature coefficient for microwave applications. *IEE Proc.: Sci. Meas. Technol.*, 147(6):269–273, 2000.

[16] N. Okada and J. B. Cole. Simulation of whispering gallery modes in the Mie regime using the nonstandard finite-difference time domain algorithm. *J. Opt. Soc. Am. B*, 27(4):631–639, 2010.

[17] X. Du, S. Vincent, and T. Lu. Full-vectorial whispering-gallery-mode cavity analysis. *Opt. Express*, 21(19):22012–22022, Sep 2013.

[18] X. Du, S. Vincent, M. Faucher, M.-J. Picard, and T. Lu. Generalized full-vector multi-mode matching analysis of whispering gallery microcavities. *Opt. Express*, 22(11):13507–13514, 2014.

[19] J. Wiersig. Boundary element method for resonances in dielectric microcavities. *J. Opt. A: Pure Appl. Opt.*, 5(1):53–60, 2003.

[20] C.-L. Zou, H. G. L. Schwefel, F.-W. Sun, Z.-F. Han, and G.-C. Guo. Quick root searching method for resonances of dielectric optical microcavities with the boundary element method. *Opt. Express*, 19(17):15669–15678, 2011.

[21] L. Pan and T. Lu. Highly efficient boundary element analysis of whispering gallery microcavities. *IEEE Photonics Technol. Lett.*, 26(24):2465–2468, 2014.

[22] M. A. Cheraghi Shirazi, W. Yu, S. Vincent, and T. Lu. Cylindrical beam propagation modelling of perturbed whispering-gallery mode microcavities. *Opt. Express*, 21(25):30243–30254, 2013.

[23] M. Oxborrow. Traceable 2-D finite-element simulation of the whispering-gallery modes of axisymmetric electromagnetic resonators. *IEEE Trans. Microwave Theory Tech.*, 55(6):1209–1218, 2007.

[24] C. Grossmann, H.-G. Roos, and M. Stynes. *Numerical Treatment of Partial Differential Equations*, chapter 2, pages 23–124. Berlin/Heidelberg: Springer, 1st edition, 2007.

[25] G. R. Hadley. High-accuracy finite-difference equations for dielectric waveguide analysis I: uniform regions and dielectric interfaces. *J. Lightwave Technol.*, 20(7):1210–1218, 2002.

[26] G. R. Hadley. High-accuracy finite-difference equations for dielectric waveguide analysis II: dielectric corners. *J. Lightwave Technol.*, 20(7):1219–1231, 2002.

[27] Y.-C. Chiang, Y.-P. Chiou, and H.-C. Chang. Improved full-vectorial finite-difference mode solver for optical waveguides with step-index profiles. *J. Lightwave Technol.*, 20(8):1609–1618, 2002.

[28] J. W. Strutt. The problem of the whispering gallery. *Philos. Mag.*, 20(120):1001–1004, 1910.

[29] R. D. Richtmyer. Dielectric resonators. *J. Appl. Phys.*, 10(6):391–398, 1939.

[30] A. Ashkin and J. M. Dziedzic. Observation of resonances in the radiation pressure on dielectric spheres. *Phys. Rev. Lett.*, 38(23):1351–1354, 1977.

[31] R. E. Benner, P. W. Barber, J. F. Owen, and R. K. Chang. Observation of structure resonances in the fluorescence spectra from microspheres. *Phys. Rev. Lett.*, 44(7):475–478, 1980.

[32] V. B. Braginsky, M. L. Gorodetsky, and V. S. Ilchenko. Quality-factor and nonlinear properties of optical whispering-gallery modes. *Phys. Lett. A*, 137(7-8):393 – 397, 1989.

[33] B. Jowers. Whispering Gallery, 2011. Accesed 28 October 2014, ⟨http://templeofheavenbeijing.com/whispering-gallery/⟩.

[34] M. L. Gorodetsky, A. A. Savchenkov, and V. S. Ilchenko. Ultimate Q of optical microsphere resonators. *Opt. Lett.*, 21(7):453–455, 1996.

[35] M. Cai, O. Painter, and K. J. Vahala. Observation of critical coupling in a fiber taper to a silica-microsphere whispering-gallery mode system. *Phys. Rev. Lett.*, 85(1):74–77, 2000.

[36] L. Collot, V. Lefvre-Seguin, M. Brune, J. M. Raimond, and S. Haroche. Very high-Q whispering-gallery mode resonances observed on fused silica microspheres. *Europhys. Lett.*, 23(5):327334, 1993.

[37] A. Serpengüzel, G. Griffel, and S. Arnold. Excitation of resonances of microspheres on an optical fiber. *Opt. Lett.*, 20(7):654–656, 1995.

[38] F. Vollmer and S. Arnold. Whispering-gallery-mode biosensing: label-free detection down to single molecules. *Nat. Methods*, 5(7):591–596, 2008.

[39] S. Arnold, M. Khoshsima, I. Teraoka, S. Holler, and F. Vollmer. Shift of whispering-gallery modes in microspheres by protein adsorption. *Opt. Lett.*, 28(4):272–274, 2003.

[40] F. Vollmer, S. Arnold, and D. Keng. Single virus detection from the reactive shift of a whispering-gallery mode. *PNAS*, 105(52):20701–20704, 2008.

[41] M. L. Gorodetsky, A. D. Pryamikov, and V. S. Ilchenko. Rayleigh scattering in high-Q microspheres. *J. Opt. Soc. Am. B*, 17(6):1051–1057, 2000.

[42] A. L. Schawlow and C. H. Townes. Infrared and optical masers. *Phys. Rev.*, 112(6):1940–1949, 1958.

[43] T. Lu, T.-T. J. Su, K. J. Vahala, and S. E. Fraser. Split frequency sensing methods and systems. *US Patent* 8,593,638 B2, 2013.

[44] J. Zhu, S. K. Ozdemir, Y.-F. Xiao, L. Li, L. He, D.-R. Chen, and L. Yang. On-chip single nanoparticle detection and sizing by mode splitting in an ultrahigh-Q microresonator. *Nature Photon.*, 4(1):46–49, 2010.

[45] S.-X. Qian, J. B. Snow, H.-M. Tzeng, and R. K. Chang. Lasing droplets: highlighting the liquid-air interface by laser emission. *Science*, 231(4737):486–488, 1986.

[46] J.-Z. Zhang and R. K. Chang. Generation and suppression of stimulated Brillouin scattering in single liquid droplets. *J. Opt. Soc. Am. B. : Opt. Phys.*, 6(2):151–153, 1989.

[47] A. J. Campillo, J. D. Eversole, and H.-B. Lin. Cavity quantum electrodynamic enhancement of stimulated emission in microdroplets. *Phys. Rev. Lett.*, 67(4):437–440, 1991.

[48] H.-B. Lin and A. J. Campillo. cw Nonlinear optics in droplet microcavities displaying enhanced gain. *Phys. Rev. Lett.*, 73(18):2440–2443, 1994.

[49] H.-B. Lin and A. J. Campillo. Microcavity enhanced Raman gain. *Opt. Commun.*, 133(1-6):287–292, 1997.

[50] I. S. Grudinin, H. Lee, T. Chen, and K. J. Vahala. Compensation of thermal nonlinearity effect in optical resonators. *Opt. Express*, 19(8):7365–7372, 2011.

[51] S. Xiao, M. H. Khan, H. Shen, and M. Qi. Compact silicon microring resonators with ultra-low propagation loss in the C band. *Opt. Express*, 15(22):14467–14475, 2007.

[52] A. Gondarenko, J. S. Levy, and M. Lipson. High confinement micron-scale silicon nitride high Q ring resonator. *Opt. Express*, 17(14):11366–11370, 2009.

[53] V. S. Ilchenko, A. A. Savchenkov, A. B. Matsko, and L. Maleki. Nonlinear optics and crystalline whispering gallery mode cavities. *Phys. Rev. Lett.*, 92(4):043903, 2004.

[54] A. Andronico, J. Claudon, J. M. Gerard, V. Berger, and G. Leo. Integrated terahertz source based on three-wave mixing of whispering-gallery modes. *Opt. Lett.*, 33(21):2416–2418, 2008.

[55] I. S. Grudinin, V. S. Ilchenko, and L. Maleki. Ultrahigh optical Q factors of crystalline resonators in the linear regime. *Phys. Rev. A*, 74(6):063806, 2006.

[56] A. N. Oraevsky. Whispering-gallery waves. *Quant. Electron.*, 32(5):377–400, 2002.

[57] M. Iqbal, M. A. Gleeson, B. Spaugh, F. Tybor, W. G. Gunn, M. Hochberg, T. Baehr-Jones, R. C. Bailey, and L. C. Gunn. Label-free biosensor arrays based on silicon ring resonators and high-speed optical scanning instrumentation. *IEEE J. Sel. Top. Quantum Electron.*, 16(3):654–661, 2010.

[58] G. T. Reed, G. Mashanovich, F. Y. Gardes, and D. J. Thomson. Silicon optical modulators. *Nature Photon.*, 4(8):518–526, 2010.

[59] P Dong, N.-N. Feng, D. Feng, W. Qian, H. Liang, D. C. Lee, B. J. Luff, T. Banwell, A. Agarwal, P. Toliver, R Menendez, T. K. Woodward, and M. Asghari. GHz-bandwidth optical filters based on high-order silicon ring resonators. *Opt. Express*, 18(23):23784–23789, 2010.

[60] T. J. Kippenberg and K. J. Vahala. Demonstration of high-Q microdisk resonators: fabrication and nonlinear properties. In *Lasers and Electro-Optics, 2007. CLEO 2007. Conference on*, pages 1–2, 6-11 May 2007.

[61] H. Lee, T. Chen, J. Li, K. Y. Yang, S. Jeon, O. Painter, and K. J. Vahala. Chemically etched ultrahigh-Q wedge-resonator on a silicon chip. *Nature Photon.*, 6(6):369373, 2012.

[62] Q. Lin, T. J. Johnson, C. P. Michael, and O. Painter. Adiabatic self-tuning in a silicon microdisk optical resonator. *Opt. Express*, 16(19):14801–14811, 2008.

[63] D. K. Armani, T. J. Kippenberg, S. M. Spillane, and K. J. Vahala. Ultra-high-Q toroid microcavity on a chip. *Nature*, 421(6926):925–928, 2003.

[64] P. Del'Haye, A. Schliesser, O. Arcizet, T. Wilken, R. Holzwarth, and T. J. Kippenberg. Optical frequency comb generation from a monolithic microresonator. *Nature*, 450(7173):1214–1217, 2007.

[65] T. J. Kippenberg and K. J. Vahala. Cavity opto-mechanics. *Opt. Express*, 15(25):17172–17205, 2007.

[66] Q. Lin, J. Rosenberg, X. Jiang, K. J. Vahala, and O. Painter. Mechanical oscillation and cooling actuated by the optical gradient force. *Phys. Rev. Lett.*, 103(10):103601, 2009.

[67] M. Sumetsky, Y. Dulashko, and R. S. Windeler. Optical microbubble resonator. *Opt. Lett.*, 35(7):898–900, 2010.

[68] S. Berneschi, D. Farnesi, F. Cosi, G. Nunzi Conti, S. Pelli, G. C. Righini, and S. Soria. High Q silica microbubble resonators fabricated by arc discharge. *Opt. Lett.*, 36(17):3521–3523, 2011.

[69] M. Pöllinger, D. O'Shea, F. Warken, and A. Rauschenbeutel. Ultrahigh-Q tunable whispering-gallery-mode microresonator. *Phys. Rev. Lett.*, 103(5):053901, 2009.

[70] J. Volz, M. Scheucher, C. Junge, and A. Rauschenbeutel. Nonlinear π phase shift for single fibre-guided photons interacting with a single resonator-enhanced atom. *Nature Photon.*, 8(12):965–970, 2014.

[71] K. Zhu, K. Han, T. Carmon, X. Fan, and G. Bahl. Opto-acoustic sensing of fluids and bioparticles with optomechanofluidic resonators. *Eur. Phys. J.*, 223(10):1937–1947, 2014.

[72] I. M. White, H. Oveys, and X. Fan. Liquid-core optical ring-resonator sensors. *Opt. Lett.*, 31(9):1319–1321, 2006.

[73] R. H. Ritchie. Plasma losses by fast electrons in thin films. *Phys. Rev.*, 106(5):874–881, 1957.

[74] R. W. Wood. On a remarkable case of uneven distribution of light in a diffraction grating spectrum. *Philos. Mag.*, 4(19-24):396–402, 1902.

[75] U. Fano. The theory of anomalous diffraction gratings and of quasi-stationary waves on metallic surfaces (Sommerfeld's waves). *J. Opt. Soc. Am.*, 31(3):213–222, 1941.

[76] R. H. Ritchie, E. T. Arakawa, J. J. Cowan, and R. N. Hamm. Surface-plasmon resonance effect in grating diffraction. *Phys. Rev. Lett.*, 21(22):1530–1533, 1968.

[77] L. Novotny and B. Hecht. *Principles of Nano-Optics*. New York: Cambridge University Press, 1st edition, 2006.

[78] B. Min, E. Ostby, V. Sorger, E. Ulin-Avila, L. Yang, X. Zhang, and Kerry Vahala. High-Q surface-plasmon-polariton whispering-gallery microcavity. *Nature*, 457(7228):455–458, 2009.

[79] V. R. Dantham, S. Holler, C. Barbre, D. Keng, V. Kolchenko, and S. Arnold. Label-free detection of single protein using a nanoplasmonic-photonic hybrid microcavity. *Nano Lett.*, 13(7):3347–3351, 2013.

[80] M. R. Foreman, W.-L. Jin, and F. Vollmer. Optimizing detection limits in whispering gallery mode biosensing. *Opt. Express*, 22(5):5491–5511, 2014.

[81] Y. Hu, L. Shao, S. Arnold, Y.-C. Liu, C.-Y. Ma, and Y.-F. Xiao. Mode broadening induced by nanoparticles in an optical whispering-gallery microcavity. *Phys. Rev. A*, 90(4):043847, 2014.

[82] J. D. Jackson. *Classical Electrodynamics*. New York: Wiley, 2nd edition, 1975.

[83] S. A. Holmes and W. E. Featherstone. A unified approach to the Clenshaw summation and the recursive computation of very high degree and order normalised associated Legendre functions. *J. Geod.*, 76(5):279–299, 2002.

[84] M. Abramowitz and I. A. Stegun. *Handbook of Mathematical Functions with Formulas, Graphs, and Mathematical Tables*, chapter 8, pages 331–341. New York: Dover, 9th edition, 1972.

[85] O. L. Colombo. Numerical methods for harmonic analysis on the sphere. Technical Report 310, Department of Geodetic Science and Surveying, The Ohio State University, Columbus, 1981.

[86] P. M. Morse and H. Feshbach. *Methods of Theoretical Physics, Part I*, chapter 4.3, pages 374–398. New York: McGraw-Hill, 1953.

[87] T. J. Kippenberg, S. M. Spillane, D. K. Armani, and K. J. Vahala. Ultralow-threshold microcavity Raman laser on a microelectronic chip. *Opt. Lett.*, 29(11):1224–1226, 2004.

[88] R. B. Lehoucq, D. C. Sorensen, and C. Yang. *ARPACK Users Guide: Solution of Large-Scale Eigenvalue Problems with Implicity Restarted Arnoldi Methods*. Philadelphia: SIAM, 1998.

[89] K. Srinivasan, M. Borselli, O. Painter, A. Stintz, and S. Krishna. Cavity Q, mode volume, and lasing threshold in small diameter AlGaAs microdisks with embedded quantum dots. *Opt. Express*, 14(3):1094–1105, 2006.

[90] T. J. Kippenberg. *Nonlinear Optics in Ultra-high-Q Whispering-Gallery Optical Microcavities*. PhD thesis, California Institute of Technology, 2004.

[91] K. J. Russell, T.-L. Liu, S. Cui, and E. L. Hu. Large spontaneous emission enhancement in plasmonic nanocavities. *Nature Photon.*, 6(7):459–462, 2012.

[92] S.-H. Kwon. Deep subwavelength plasmonic whispering-gallery-mode cavity. *Opt. Express*, 20(22):24918–24924, 2012.

[93] Y.-F. Xiao, Y.-C. Liu, B.-B. Li, Y.-L. Chen, Y. Li, and Q. Gong. Stongly enhanced light-matter interaction in a hybrid photonic-plasmonic resonator. *Phys. Rev. A*, 85(3):031805(R), 2012.

[94] T. J. Kippenberg, J. Kalkman, A. Polman, and K. J. Vahala. Demonstration of an erbium-doped microdisk laser on a silicon chip. *Phys. Rev. A*, 74(5):051802(R), 2006.

[95] P. B. Johnson and R. W. Christy. Optical constants of the noble metals. *Phys. Rev. B*, 6(12):4370–4379, 1972.

[96] T. E. van Deventer and L. P. B. Katehi. Generalized boundary conditions with application to submillimeter and optical waveguides. *Radio Sci.*, 31(6):1407–1416, 1996.

[97] A. M. Turing. Rounding-off errors in matrix processes. *Q. J. Mechanics Appl. Math.*, 1(1):287–308, 1948.

[98] W. H. Press, S. A. Teukolsky, W. T. Vetterling, and B. P. Flannery. *Numerical Recipes: The Art of Scientific Computing*, chapter 17.3 - Richardson Extrapolation and the Bulirsch-Stoer Method, pages 921–928. New York: Cambridge University Press, 3rd edition, 2007.